Acta Pharmaceutica Sinica B 2026;16(4):2444−2473

Chinese Pharmaceutical Association
Institute of Materia Medica, Chinese Academy of Medical Sciences

Acta Pharmaceutica Sinica B

www.elsevier.com/locate/apsb
www.sciencedirect.com

ORIGINAL ARTICLE

Generative active learning guided discovery of a tobramycin and ciprofloxacin adjuvant against multidrug-resistant *Pseudomonas aeruginosa* infections

Siyu Zhao[a,†], Jie Tang[a,†], Ziyang Du[a,†], Yujie Li[a], Yingbo Zhou[a], Wenqian Liu[a], Xiao Wu[a], Xibing Hu[a], Xin Long[a], Dengchao Lian[b], Jinglin Xie[b], Tiantian Xie[b], Shuo Dai[b], Daxi He[a], Jiahui Su[a], Youfeng Zhu[d], Yiqun Chang[a,*], Junxia Zheng[c,*], Jun Liu[a,*], Pinghua Sun[a,b,d,*]

[a]*State Key Laboratory of Bioactive Molecules and Druggability Assessment, College of Pharmacy, Institute for Advanced and Applied Chemical Synthesis, Jinan University, Guangzhou 510632, China*
[b]*Key Laboratory of Xinjiang Phytomedicine Resource and Utilization, Ministry of Education, School of Pharmacy, Shihezi University, Shihezi 832003, China*
[c]*School of Biomedical and Pharmaceutical Sciences, Guangdong University of Technology, Guangzhou 510006, China*
[d]*Department of Critical Care Medicine, Guangzhou Red Cross Hospital, Jinan University, Guangzhou 510220, China*

Received 26 June 2025; received in revised form 24 December 2025; accepted 24 December 2025

KEY WORDS

Pseudomonas aeruginosa;
Multidrug-resistant;
Antibacterial adjuvant;
Generative active learning;
Succinate dehydrogenase;

Abstract Biofilm-mediated resistance in multidrug-resistant (MDR) *Pseudomonas aeruginosa* infections severely compromise antibiotic efficacy in clinical applications. Antibacterial adjuvants represent a promising strategy to restore antibiotic sensitivity and reduce therapeutic dosages. To identify new antibacterial adjuvants with unique structure and mechanism, we established a generative active learning workflow integrating an in-house compound repository of 725 biofilm inhibitors and a library of potential antibiofilm targets. The most potent compound STY17 was identified with sub-micromolar antibiofilm

*Corresponding authors.
E-mail addresses: Changyiqun_4907@126.com (Yiqun Chang), junxiazheng@gdut.edu.cn (Junxia Zheng), liujun__jnu@163.com (Jun Liu), pinghuasunny@163.com (Pinghua Sun).
[†]These authors made equal contributions to this work.
Peer review under the responsibility of Chinese Pharmaceutical Association and Institute of Materia Medica, Chinese Academy of Medical Sciences.

https://doi.org/10.1016/j.apsb.2026.02.002

Tobramycin;
Ciprofloxacin;
Biofilm

activity (IC_{50} = 0.29 ± 0.01 μmol/L). In clinically isolated MDR *Pseudomonas aeruginosa*, STY17 significantly inhibited biofilm formation, potently synergized with tobramycin and ciprofloxacin, and suppressed the resistance development of these antibiotics. Furthermore, mechanistic studies indicated that STY17 inhibited succinate dehydrogenase to disrupt biofilm formation. *In vivo*, STY17 significantly enhanced the antibacterial activity of tobramycin and ciprofloxacin in *Galleria mellonella* and the mouse wound infection model with favorable safety profiles. These findings validated the utility of machine learning to discover novel antibacterial adjuvants, revealing STY17 as a promising candidate for antibacterial adjuvants against MDR *Pseudomonas aeruginosa* infections.

1. Introduction

The increasing prevalence of multidrug-resistant (MDR) pathogens is a major global health threat in the 21st century, making bacterial infections extremely challenging and costly to treat[1]. Antimicrobial resistance caused about 4.95 million deaths in 2019, and the number of deaths is estimated to surge to 10 million per year by 2050[2-4]. Even though a great deal of effort has been invested in developing novel antibiotics, few of them have been approved for the treatment of bacterial infections in recent decades[5-7], further exacerbating the need for novel therapies against MDR infections.

Pseudomonas aeruginosa is a threatening opportunistic pathogen, particularly known for causing recalcitrant infections in wounds and lungs that contribute to high morbidity and mortality[8,9]. Ciprofloxacin and tobramycin are commonly used in clinical settings for their cost-effectiveness and potent antimicrobial activity to address wound and lung infections of *P. aeruginosa*[10,11], however, their resistance increased from 19% to 56% in ten years[12]. The ability of the *P. aeruginosa* to colonize and form biofilms at these sites is thought to be an important factor that leads to a significant reduction in the efficacy and persistent resistance of these two antibiotics[13,14]. As complex bacterial communities embedded in extracellular matrix, biofilms constitute a strong physical and biochemical barrier that significantly limits the penetration and diffusion of clinically used antibiotics, including ciprofloxacin and tobramycin[15-17], reducing their susceptibility by up to 1000-fold[18]. Therefore, the development of antibacterial adjuvants targeting biofilms is an effective way to restore the killing efficacy of ciprofloxacin and tobramycin against biofilm-associated MDR *P. aeruginosa* infections.

Three antibacterial adjuvants that enhance the efficacy of ciprofloxacin and tobramycin are currently in clinical trials, which facilitate the uptake of these antibiotics by impairing biofilm formation in *P. aeruginosa*[19-24]. Despite this progress, no antibiofilm agents are available on the market, representing a significant unmet medical lack for biofilm inhibitors as antibacterial adjuvants. Taking into consideration that the structural diversity of these antibacterial adjuvants in clinical trials is limited (antimicrobial peptides or polymers), and the inherent challenges of conventional drug screening methods in identifying new chemotypes with unique mechanisms, necessitating a need for innovative approaches. Machine learning (ML)-driven *de novo* molecular design has emerged as a transformative strategy for developing small-molecule antimicrobial adjuvants with novel structures and mechanisms[25]. By leveraging deep generative models (DGMs) with reward-driven optimization, this approach iteratively designs compounds exhibiting tailored properties, including high target affinity, optimal ADMET profiles, and low synthetic complexity[26]. Furthermore, the integration of generative AI with active learning (AL) leads to generative active learning (GAL). By learning complex structure-activity relationships and latent chemical features from known datasets, GAL can propose novel, synthetically accessible molecular structures with optimized properties *in silico*[27-29]. This capability to efficiently capture potential structural motifs and generate focused libraries significantly accelerates the identification of promising adjuvant candidates against MDR pathogens.

Previous studies in our laboratory have validated the potential of biofilm inhibitors to enhance the antimicrobial activity of antibiotics[30-36]. Based on this, this study created an in-house compound repository of 725 biofilm inhibitors and a library of potential antibiofilm targets, leading to the establishment of a GAL workflow to discover antibacterial adjuvants with new structures and mechanisms. Through this approach and further optimization, compound STY17 was identified as a potent biofilm inhibitor, exhibiting sub-micromolar activity (IC_{50} = 0.29 ± 0.01 μmol/L). In clinical MDR *P. aeruginosa* isolates, STY17 significantly inhibited biofilm formation, exhibited potent synergy with tobramycin and ciprofloxacin, and suppressed resistance development to both antibiotics. Critically, in *Galleria mellonella* and murine wound infection models of *P. aeruginosa*, STY17 demonstrated a significant synergistic effect with tobramycin and ciprofloxacin, increasing the survival rate to 100% and resulting in 0.92−1.46-$\log_{10}$ CFU/mL reduction of bacterial burden. Moreover, mechanistic studies revealed that STY17 potently inhibited succinate dehydrogenase (SDH) to suppress the tricarboxylic acid (TCA) cycle, electron transport chain, and biofilm formation. Collectively, this study highlighted the utility of machine learning in discovering novel antibacterial adjuvants and revealed the promising potential of derivative STY17 as an antibacterial adjuvant against multidrug-resistant *P. aeruginosa* infections.

2. Results and discussion

2.1. Establishment of generative active learning models of structure innovation

We employed a generative model (Fig. 1) to create novel molecules in real-time, effectively representing a vast dynamic subset of chemical space, thereby replacing the reliance on static large databases or vendor catalogs. Reinforcement learning (RL) *via* the REINVENT[37] framework was utilized to generate new molecules

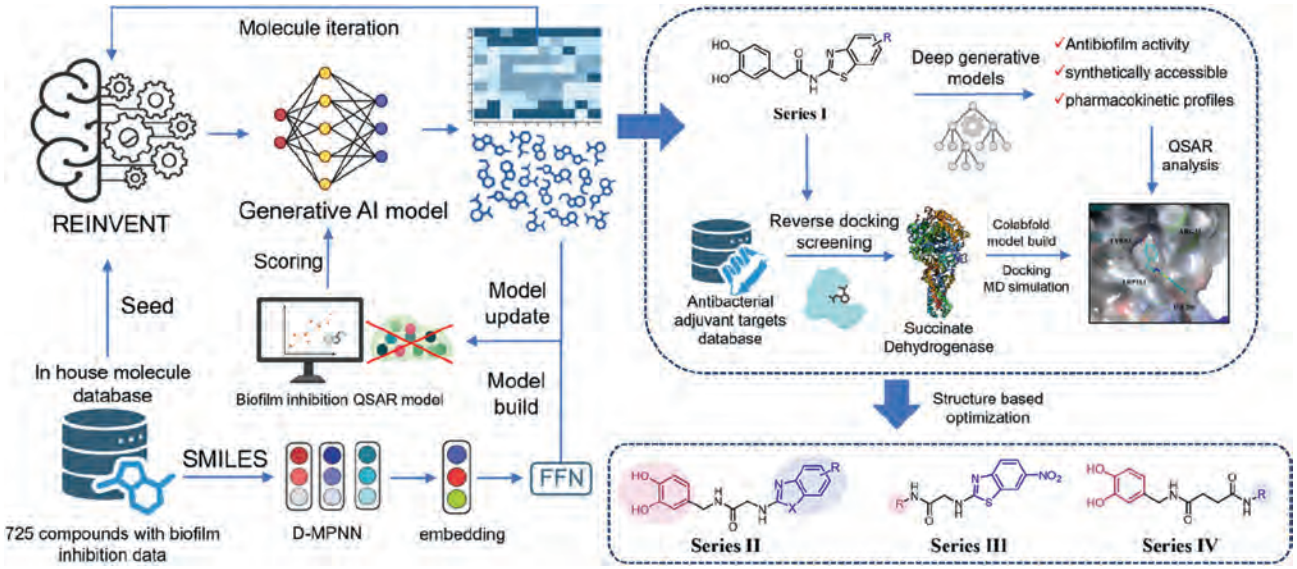

Figure 1 Overall workflow of generative active learning guided molecule design, target identification, and molecular optimization.

constrained by a user-defined scoring function. The RL algorithm drives a chemically knowledgeable prior model towards a specialized target chemical space. The scoring function is a weighted arithmetic or geometric mean of several scoring components, with the primary scoring component (weight = 0.6) being a QSAR-like surrogate model based on our previous work. This surrogate model, implemented with ChemProp[38], utilizes directed message-passing neural networks (D-MPNNs) to predict molecular properties directly from molecular graph structures (atoms as nodes, bonds as edges). It was trained on our published dataset of 725 unique compounds exhibiting biofilm inhibitory activity[30-32,34-36,39,40]. As these compounds potentially target various points, yet all manifest the common phenotypic outcome of biofilm inhibition, biofilm inhibitory activity was selected as the target property for modeling, facilitating data normalization. Molecular graphs were reconstructed from SMILES strings using RDKit[41]. The ChemProp model was trained for a maximum of 30 epochs[28], with the initial dataset split into training (80%), testing (10%), and validation (10%) sets. The surrogate model exhibited robust performance, achieving an R^2 of 0.91, MAE of 0.21, RMSE of 0.27; the cross-validated Q^2 was 0.82. Additional scoring components included QED (quantitative estimate of drug-likeness), Tanimoto similarity to known actives, and structural alerts, serving as filters. A Tanimoto coefficient threshold of 0.5 was set for the screening of generated compounds to maintain structural novelty. The batch size per generative active learning (GAL) iteration step was set to 50.

2.2. *Identification of the key scaffold and target for potential biofilm inhibitors*

Next, we applied the GAL models to identify the key scaffold of potential biofilm inhibitors. After five GAL iteration cycles, cluster analysis and synthetic accessibility assessment identified a novel scaffold comprised of the catechol and benzothiazole *via* an amide linker. It demonstrated 57% predicted biofilm inhibition with high synthetic accessibility, highlighting its potential as a promising chemical series. Compared to random screening in chemical space, the surrogate model-guided generative design significantly enhanced efficiency. Moreover, when allocated equivalent computational resources, the GAL method demonstrated an approximately five-fold increase in efficiency over traditional virtual screening in generating novel structures. Furthermore, the GAL model is characterized by integrating biofilm-inhibitory scaffold discovery with direct target prediction. For catechol-conjugated benzothiazole compounds, target hypotheses were generated *via* reverse docking against our in-house database of known or potential biofilm targets. Docking results (Supporting Information Fig. S1A−S1C) indicated affinity towards several targets (including RhlR and lasR, etc.), with the strongest predicted affinity for succinate dehydrogenase (SDH, PDB code: 1NEK). This finding aligns with reports of significant *sdhCAB* upregulation in biofilms and the severe biofilm deficiency observed in *sdhCAB* mutants[42]. Further supporting evidence comes from promysalin and its derivatives, which are discovery-stage compounds that inhibit *P. aeruginosa* biofilms and enhance antibiotic activity by targeting SDH[43]. Collectively, these results suggested that catechol-conjugated benzothiazole compounds potentially inhibit biofilm by impairing SDH.

2.3. *Structural analysis and optimization*

As the *P. aeruginosa* SDH has not yet been crystallized, we leveraged the homologous enzyme from *Escherichia coli* (PDB: 1NEK) for initial docking[44]. Next, we generated a high-confidence *P. aeruginosa* SDH complex model (subunits A−D, sequences from UniProt[45]) using ColabFold multimer for further investigation[46]. This model exhibited high pLDDT scores with protein cofactors modeled from the *E. coli* structure (Supporting Information Fig. S2A−S2C). The results indicated that key interactions involved the catechol moiety forming hydrogen bonds and the benzoheterocycle engaging in $\pi-\pi$ stacking with critical residues TYR83 and TRP161, respectively, highlighting their potential as novel antibiofilm pharmacophores. MD simulations confirmed binding stability but revealed a critical limitation in GAL-generated compounds: the key interactions of the two terminal fragments exhibited some degree of mutual exclusivity. The catechol and heterocycle interacted with key residues for 32% and

37% of the simulation time, yet simultaneous binding occurred only 7.2%. This is likely attributable to the molecular size, primarily the linker length, forcing bent conformations that are only marginally sufficient for optimal simultaneous engagement.

Based on this hypothesis, we designed structural modifications focusing on: (1) introducing different substitutions to benzothiazole, yielding Series I. (2) Replacing the amide linker with an aminoacetamide linker to enhance spatial compatibility between pharmacophores and substituting benzothiazole with benzoxazole to modulate $\pi-\pi$ stacking strength, generating Series II. (3) Systematic structure-activity relationship studies were conducted through the removal of catechol (Series III) and benzothiazole (Series IV) pharmacophores (Fig. 1).

2.4. Chemistry

The synthetic route to compounds STY1−STY11 (except STY2 and STY8) is shown in Scheme 1. 3,4-Dimethoxyphenylacetic acid (**1**) and 2-aminobenzothiazole containing different substituents were used as reactants to obtain intermediates **3a−3k** by 2-(7-azabenzotriazole)-*N*,*N*,*N*′,*N*′-tetramethyluronium hexafluorophosphate (HATU)-catalyzed amide condensation reaction. Subsequently, the compounds **3a−3k** were dissolved in dichloromethane (DCM), and BBr_3 was slowly added dropwise in an ice bath. Upon reaction completion, ice water was added to quench the reaction, and the resulting solids were filtered to obtain the target compounds STY1, STY3−STY7, and STY9−STY11.

The synthetic route to compounds STY2 and STY8 is shown in Scheme 2. 3,4-Dimethoxyphenylacetic acid (**1**) was dissolved in DCM, and BBr_3 was slowly added dropwise under argon protection as well as ice bath conditions. Upon reaction completion, ice water was added to quench the reaction, and the intermediate **4** was obtained by extraction with DCM. Subsequently, 4-methoxy-2-aminobenzothiazole (**2b**) or 6-methoxy-2-aminobenzothiazole (**2h**) and **4** were used as reactants to obtain the solid compounds STY2, STY8 by HATU-catalyzed amide condensation reaction.

The synthetic route to compounds STY12−STY27 is shown in Scheme 3. (3,4-Dimethoxyphenyl) methanamine (**6**), *N*-Boc-glycine (**5**), and *N*,*N*-diisopropylethylamine (DIPEA) were used as reactants in DCM to obtain intermediate **7** by HATU-catalyzed amide condensation reaction. Subsequently, the removal of the Boc protecting group from **7** with trifluoroacetic acid (TFA) in DCM yielded compound **8**. Intermediate **8** was then subjected to a nucleophilic substitution reaction with diversely substituted compounds **9a−9p** under potassium iodide (KI) catalysis, affording intermediates **10a−10p**. Finally, BBr_3-mediated deprotection of **10a−10p** obtained target compounds STY12−STY27.

The synthetic route to compounds STY28−STY33 is shown in Scheme 4. Intermediates **12a−12f** were synthesized by condensing *N*-Boc-glycine (**5**) with diversely substituted amines. Subsequently, Boc deprotection of **12a−12f** using trifluoroacetic acid (TFA) afforded compounds **13a−13f**. Intermediates **13a−13f** then underwent KI-catalyzed nucleophilic substitution with 2-chloro-6-nitrobenzothiazole (**14**) in the presence of DIPEA, yielding target compounds STY28−STY33.

The synthetic route to compounds STY34−STY41 is shown in Scheme 5. Intermediate **16** was synthesized by treating 3,4-dimethoxybenzylamine (**6**) with succinic anhydride in DCM, using triethylamine as a base. The reaction was stirred at room temperature for 1 h, affording **16** as a white solid. Intermediate **16** was then dissolved in DCM containing diversely substituted amines, HATU, and triethylamine, stirring at room temperature for 6 h to obtain the intermediates **18a−18h**. Finally, BBr_3-mediated deprotection of **18a−18h** obtained target compounds STY34−STY41.

2.5. Structure−activity relationship studies of the compounds

The MICs of all compounds were initially tested, and the results suggested that all of them have no effect on killing bacteria with MIC >256 μmol/L. Subsequently, biofilm inhibitory activities of all the compounds were evaluated using crystal violet staining. The results were shown in Tables 1−3.

Building upon the GAL-generated scaffold, our initial design strategy involved hybridizing the benzothiazole and catechol pharmacophores *via* an amide linker, incorporating substituents at the 4- and 5-positions of the benzothiazole. The obtained compounds STY1−STY4 exhibited measurable biofilm inhibitory activity (IC_{50} = 6.46−10.04 μmol/L), prompting further structure−activity relationships (SAR) exploration at the 6-position. Introduction of diverse electron-withdrawing and electron-donating substituents (STY5−STY9) yielded IC_{50} values ranging from 2.83 to 12.07 μmol/L. It was only compound STY5 substituted with fluorine atoms that showed efficient antibiofilm activity (IC_{50} = 2.83 ± 1.48 μmol/L), suggesting that the strong electron-withdrawing ability of compounds may be favorable for inhibiting biofilm. To probe this hypothesis, we next introduced stronger electron-withdrawing nitro (STY10) and trifluoromethyl groups (STY11) to the 6-position of the benzothiazole, which provided the compound STY10 with enhanced potency (IC_{50} = 1.18 ± 0.68 μmol/L).

Further structural optimizations were performed by replacing amide with aminoacetamide as a linker to enhance the biofilm inhibitory activity. Given that the strong electron-withdrawing

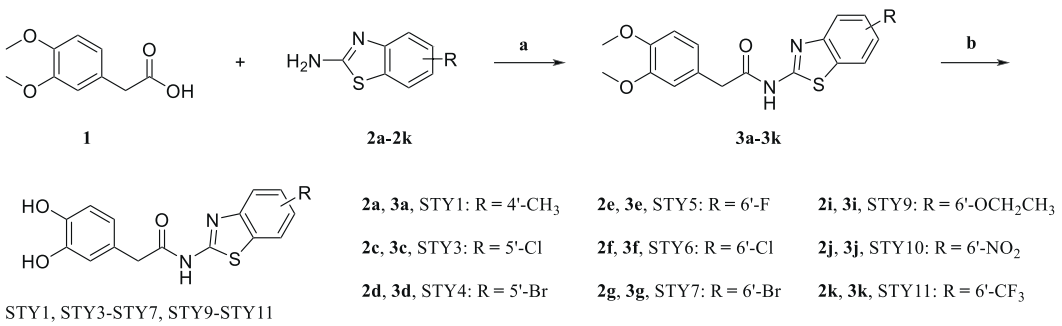

Scheme 1 Reaction conditions and reaction reagents: (a) HATU, DIPEA, DCM, rt, 12 h; (b) BBr_3, DCM, 0 °C, 30 min.

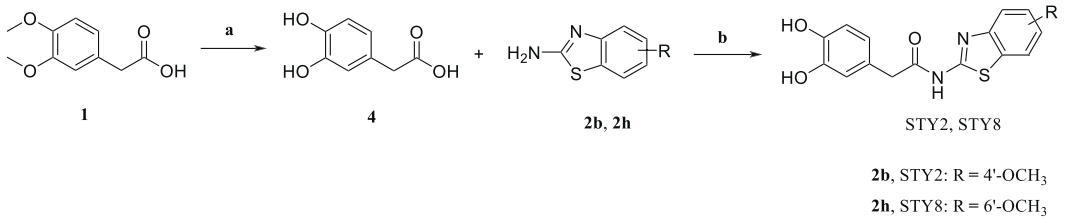

Scheme 2 Reaction conditions and reaction reagents: (a) BBr_3, DCM, 0 °C, 30 min; (b) HATU, DIPEA, DMF, rt, 12 h.

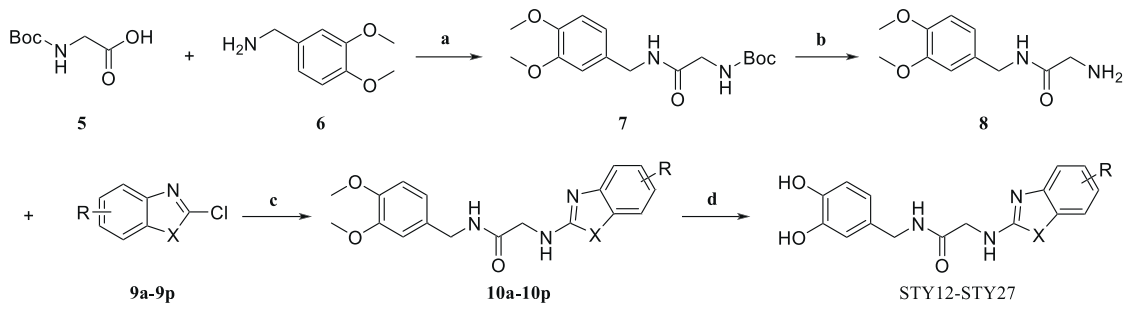

9a,**10a**, STY12: R = 6'-H, X =S
9b, **10b**, STY13: R = 6'-F, X =S
9c, **10c**, STY14: R = 6'-OCF_3, X =S
9d, **10d**, STY15: R = 6'-Br, X =S
9e, **10e**, STY16: R = 6'-CF_3, X =S
9f, **10f**, STY17: R = 6'-NO_2, X =S
9g, **10g**, STY18: R = 5'-F, X =S
9h, **10h**, STY19: R = 5'-Cl, X =S
9i, **10i**, STY20: R = 5'-Br, X =S
9j, **10j**, STY21: R = 5'-NO_2, X =S
9k, **10k**, STY22: R = 5'-NO_2, X =O
9l, **10l**, STY23: R = 5'-Cl, X =O
9m, **10m**, STY24: R = 6'-H, X =O
9n, **10n**, STY25: R = 5'-Br, X =O
9o, **10o**, STY26: R = 6'-F, X =O
9p, **10p**, STY27: R = 6'-Cl, X =O

Scheme 3 Reaction conditions and reaction reagents: (a) HATU, DIPEA, DCM, rt, 12 h; (b) CF_3COOH: DCM = 1:9, 3 h; (c) DIPEA, KI, EtOH, reflux, 12 h; (d) BBr_3, DCM, 0 °C, 30 min.

substituent at the 6-position of benzothiazole had a major effect on biofilm inhibition, we first introduced different electron-withdrawing substituent groups to the 6-position of benzothiazole. Compared to compound STY12 (IC_{50} = 4.93 ± 0.21 μmol/L) without any substituent, the introduction of the fluorine atom (STY13, IC_{50} = 16.23 ± 1.64 μmol/L) and trifluoromethoxy (STY14, IC_{50} = 17.56 ± 4.34 μmol/L) to benzothiazole resulted in an approximately four-fold decrease in antibiofilm activity. In contrast, the introduction of bromine atom (STY15, IC_{50} = 2.59 ± 0.91 μmol/L), trifluoromethyl (STY16, IC_{50} = 1.58 ± 0.52 μmol/L), nitro (STY17, IC_{50} = 0.29 ± 0.01 μmol/L) and other electron-withdrawing substituents increased the biofilm inhibitory activity of the compounds by 2-17-fold. Notably, compound STY17 featuring the strongest electron-withdrawing ability, nitro, showed the optimal biofilm inhibitory activity, which could significantly inhibit the biofilm of *P. aeruginosa* at submicromolar concentration (IC_{50} = 0.29 ± 0.01 μmol/L). This further validated the importance of strong electron-withdrawing substituents for enhancing the biofilm inhibitory activity of compounds. Subsequently, we transferred the substituent position of benzothiazole from the 6-position to the 5-position, and the obtained derivatives STY18−STY21 all exhibited reduced biofilm inhibitory activity (IC_{50} = 1.73−3.00 μmol/L) compared to compound STY17, suggesting that the 6-position of benzothiazole is the optimal substitution site and nitro is the optimal electron-withdrawing substituent. Moreover, we replaced benzothiazole with benzoxazole to improve the biofilm inhibitory activity. However, the obtained compounds STY22−STY27 (IC_{50} = 5.07−23.46 μmol/L) inhibited the biofilm formation with 17−81-fold reduced activity compared to the compound STY17, suggesting that benzothiazole is more favorable for the enhancement of the activity.

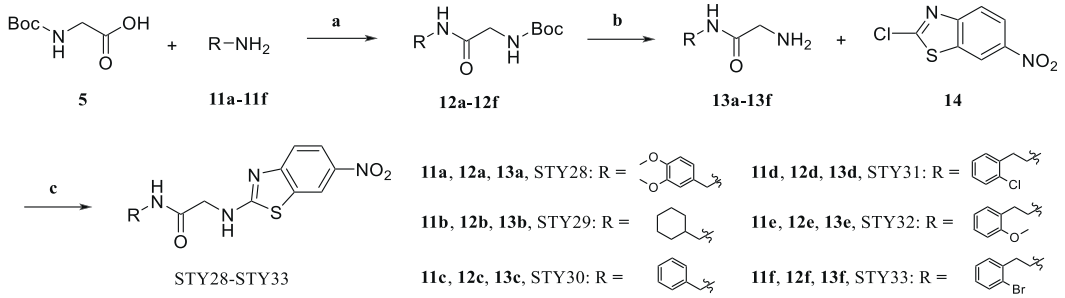

Scheme 4 Reaction conditions and reaction reagents: (a) HATU, DIPEA, DCM, rt, 12 h; (b) CF_3COOH: DCM = 1:9, 3 h; (c) DIPEA, KI, EtOH, reflux, 12 h.

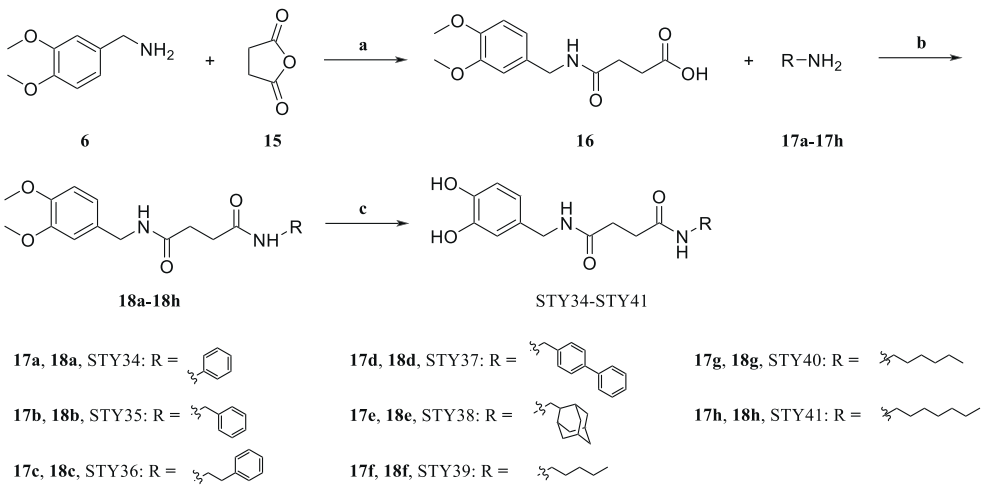

Scheme 5 Reaction conditions and reaction reagents: (a) Et_3N, DCM, rt, 1 h; (b) HATU, Et_3N, DCM, rt, 6 h; (c) BBr_3, DCM, 0 °C, 0.5 h.

In addition, the importance of catechol and benzothiazole was also assessed by replacing them with other heterocycles or alkanes, respectively. The results showed that the absence of catechols resulted in a complete loss of antibiofilm activity of compounds (STY28−STY33, $IC_{50} > 100$ μmol/L), whereas the absence of benzothiazole reduced 5-110-fold the ability of compounds STY34−STY41 ($IC_{50} = 1.57-31.83$ μmol/L) to inhibit biofilm formation in comparison with compound STY17. This indicated that catechol and benzothiazole are important pharmacophores for compounds to inhibit biofilms. Based on these findings, compound STY17 was selected as a hit compound for further investigation to explore its biological activity and mechanism.

2.6. Compound STY17 inhibits biofilm and the formation of organized structures in P. aeruginosa

The ability to form biofilms is a critical determinant in the infection and colonization processes of *P. aeruginosa*. Consequently, we initially conducted a thorough evaluation of the antibiofilm efficacy of STY17 (Fig. 2A) at various concentrations by utilizing a crystal violet assay. STY17 was found to inhibit biofilm formation in a dose-dependent manner (Fig. 2B), with the addition of 2 μmol/L STY17 resulting in a maximum reduction of 73% in biofilm when compared to untreated *P. aeruginosa*. Similarly, analysis *via* confocal laser scanning microscope (CLSM) revealed that the biofilms in the control group exhibited a

Table 1 Structures, biofilm inhibitory activities, and MICs of compounds STY1−STY11 in Series I. Azithromycin was used as a positive control.

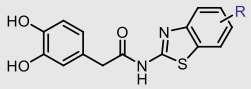

Series I

Compd.	Structure	IC_{50} (μmol/L)	MIC (μmol/L)	Compd.	Structure	IC_{50} (μmol/L)	MIC (μmol/L)
STY1	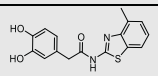	8.03±0.32	> 256	STY7	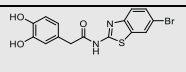	10.67±1.94	> 256
STY2	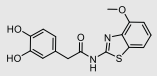	6.46±1.21	> 256	STY8	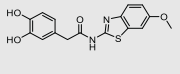	6.77±0.16	> 256
STY3	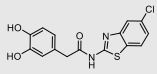	7.12±2.58	> 256	STY9	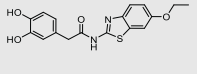	8.67±1.83	> 256
STY4	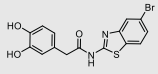	10.04±0.78	> 256	STY10	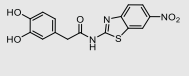	1.18±0.68	> 256
STY5	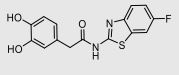	2.83±1.48	> 256	STY11	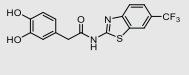	3.87±1.98	> 256
STY6	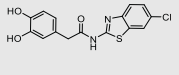	12.07±3.21	> 256		Azithromycin	6.41±0.90	

Table 2 Structures, biofilm inhibitory activities, and MICs of compounds STY12−STY27 in Series II.

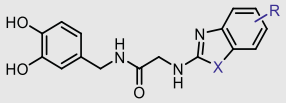

X = S, O
Series II

Compd.	Structure	IC_{50} (μmol/L)	MIC (μmol/L)	Compd.	Structure	IC_{50} (μmol/L)	MIC (μmol/L)
STY12	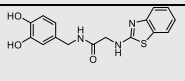	4.93±0.21	> 256	STY20	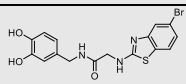	2.65±0.91	> 256
STY13	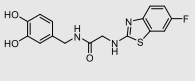	16.23±1.64	> 256	STY21	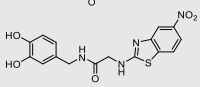	1.98±0.21	> 256
STY14	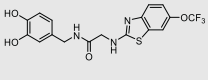	17.56±4.34	> 256	STY22	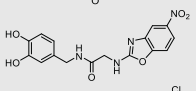	7.75±1.50	> 256
STY15	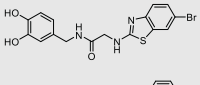	2.59±0.91	> 256	STY23	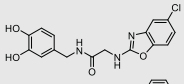	5.58±2.45	> 256
STY16	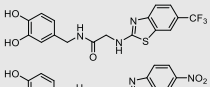	1.58±0.52	> 256	STY24	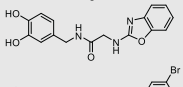	5.07±0.51	> 256
STY17	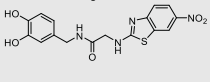	0.29±0.01	> 256	STY25	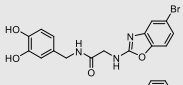	14.35±2.76	> 256
STY18	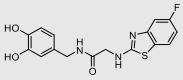	3.00±0.39	> 256	STY26	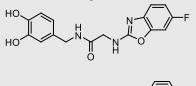	23.46±3.93	> 256
STY19	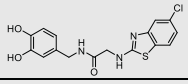	1.73±0.10	> 256	STY27	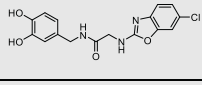	18.62±6.60	> 256

compact and thicker morphology, characterized by well-organized three-dimensional structures. In contrast, biofilms exposed to STY17 displayed a thinner and disorganized architecture, with a notable absence of intercellular adhesion (Fig. 2D). These findings strongly indicated that STY17 inhibited biofilm growth and the formation of organized structures. Additionally, the growth curves of *P. aeruginosa* strain PAO1 were not affected by STY17 compared to the control group (Fig. 2C), suggesting that STY17 may not inhibit biofilm by causing bacterial death. These findings established STY17 as a promising biofilm inhibitor.

2.7. Compound STY17 synergizes with tobramycin and ciprofloxacin against multidrug-resistant P. aeruginosa

To further validate whether the biofilm inhibitor STY17 can also exert efficient antibiofilm activity in multidrug-resistant *P. aeruginosa* infections, we next evaluated its antibiofilm activity in clinically isolated multidrug-resistant *P. aeruginosa*. As shown in Fig. 3A−F, STY17 concentration-dependently inhibited biofilm formation in these clinically multidrug-resistant strains, resulting in >50% inhibition at 2 μmol/L. Growth curve analysis confirmed that the antibiofilm effect of STY17 is not attributable to direct bacterial killing (Supporting Information Fig. S3A−S3F). The calculated IC_{50} values on inhibiting biofilm were in the low micromolar range (0.22−3.48 μmol/L), demonstrating that STY17 also potently inhibits biofilm formation in clinically multidrug-resistant *P. aeruginosa*. The high antibiofilm activities of drugs usually determine their potent low resistance and are of great translational potential as an antibacterial adjuvant in combination therapy. Therefore, the standard checkerboard microdilution method was used to examine the combination of STY17 with commonly used antibiotics tobramycin (Tob) and ciprofloxacin (CIP) for *P. aeruginosa* infections. As expected, the combination of STY17 with Tob and CIP showed excellent synergistic antibacterial activity against *P. aeruginosa* PAO1, PA182, PA1129, PA185, PA187, PA1065, and PA1167, with a fractional inhibitory concentration index (FICI) ranging from 0.259 to 0.5 (Fig. 3G−U). This suggested that STY17 represented a candidate compound with potential antimicrobial synergistic effects to combat clinically multidrug-resistant *P. aeruginosa* infections.

2.8. Compound STY17 minimizes the resistance of tobramycin and ciprofloxacin to multidrug-resistant P. aeruginosa

Prolonged exposure of bacteria to sublethal doses of antimicrobial agents usually promotes the development of resistance. Therefore, further sequential passaging experiments were performed in clinically isolated multidrug-resistant *P. aeruginosa* (PA182, PA1129, PA185, PA187) and reference strain PAO1 to evaluate resistance induction risk induced by STY17-tobramycin/ciprofloxacin combinations. The addition of Tob alone had a high tendency to induce resistance in *P. aeruginosa* (Fig. 4A−E), which exhibited a rapid increase in MIC after 12 passages, with maximum increases in MIC of 256-fold (PAO1), 128-fold (PA182), 512-fold (PA1129), 128-fold (PA185), and 256-fold (PA187), respectively. However, compound STY17 (Fig. 4K)

Table 3 Structures, biofilm inhibitory activities, and MICs of compounds STY28−STY41 in Series III and IV.

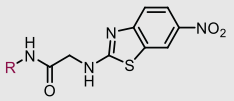

Series III

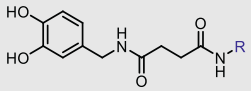

Series IV

Compd.	Structure	IC_{50} (μmol/L)	MIC (μmol/L)	Compd.	Structure	IC_{50} (μmol/L)	MIC (μmol/L)
STY28	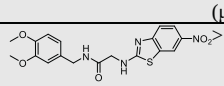	>100	> 256	STY35	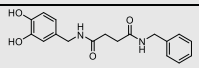	23.03±8.42	> 256
STY29	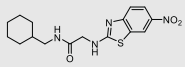	>100	> 256	STY36	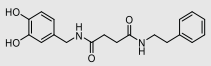	1.57±0.45	> 256
STY30	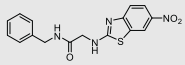	>100	> 256	STY37	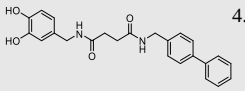	4.50±2.88	> 256
STY31	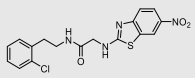	>100	> 256	STY38	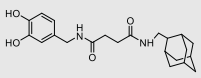	19.70±2.93	> 256
STY32	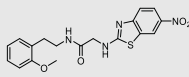	>100	> 256	STY39	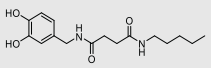	2.89±1.27	> 256
STY33	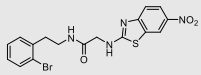	>100	> 256	STY40	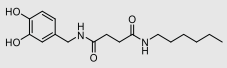	2.88±1.91	> 256
STY34	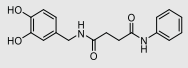	31.83±3.37	> 256	STY41	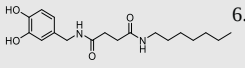	6.04±2.07	> 256

effectively prevented the emergence of tobramycin resistance in multidrug-resistant *P. aeruginosa* (MIC = 8−32 μg/mL). The same suppression of resistance development by STY17 was confirmed in combination with CIP. The treatment of CIP alone had a high tendency to induce resistance in *P. aeruginosa* (Fig. 4F−J), which exhibited a rapid increase in MIC after 12 passages, with maximum increases in MIC of 256-fold (PAO1), 2048-fold (PA182), 1024-fold (PA1129), 512-fold (PA185), and 512-fold (PA187), respectively. However, in the presence of compound STY17 (Fig. 4L), CIP remained active throughout the study (MIC = 2−16 μg/mL). These results suggested that STY17 may have advantages in preventing the development of drug resistance and has the potential to be used as an antibacterial adjuvant against multidrug-resistant *P. aeruginosa* infections.

2.9. Compound STY17 inhibits succinate dehydrogenase to disrupt biofilm formation

The previous study based on GAL models indicated that succinate dehydrogenase (SDH) may be influenced by catechol-conjugated benzothiazole compounds to inhibit biofilm. To clarify the underlying mechanism of STY17, a comprehensive *in silico* study was conducted on its SDH binding mode. The computational analysis of STY17 confirmed its interaction with SDH: the catechol hydroxyl groups form hydrogen bonds bridging SdhB and SdhD subunits, locking the compound at their interface. The NO_2-substituted benzothiazole moiety engages in a T-shaped $\pi-\pi$ interaction with TYR83 (SdhC), stabilizing the distal end within the cavity. The amide bond within the linker participates in hydrogen bonding, constraining the linker into a bent, pseudocyclic conformation (Fig. 5A). These key interactions rationalize the success of our chemical optimization strategy. Further MD simulations demonstrated stable binding of STY17 at the interface of three Sdh subunits, adopting an inwardly folded conformation. Hydrophobic interactions between its phenyl ring and residue ILE206 (Site I) were consistent with literature findings. STY17 also formed persistent hydrogen bonds with SdhB TRP161 and SdhC TYR83, and engaged in $\pi-\pi$ stacking with TYR83 for over 50% of the stable simulation trajectory (Fig. 5B). Residue-based binding free energy decomposition confirmed significant contributions from these key residues (Fig. 5C). The binding free energy calculation based on the last 50 ns equilibrium trajectory gave satisfactory results of -42.99 ± 4.1 kcal/mol. Residue-based decomposition of the binding free energy and the ligand dynamic profile (Fig. 5D) confirmed that these key residues contributed significantly to binding stabilization, which supported the interfering effect of STY17 on SDH.

The *in vitro* inhibitory activity and the results from molecular docking studies supported that STY17 effectively inhibited SDH to suppress biofilm formation. Consequently, we proceeded to assess the activity of SDH intracellularly in *P. aeruginosa* PAO1. As shown in Fig. 6A, the activity of SDH in *P. aeruginosa* was significantly reduced in a concentration-dependent manner in response to the addition of different concentrations of compound STY17. Notably, the application of 2 μmol/L STY17 resulted in a 56% inhibition of SDH activity. To further validate that STY17 regulates biofilm formation by inhibiting SDH, we constructed a *ΔsdhB* mutant in *P. aeruginosa* PAO1, which is known to have a deficiency in succinate dehydrogenase activity[42,47]. The quantification of biofilms in the *ΔsdhB* strain showed no obvious change

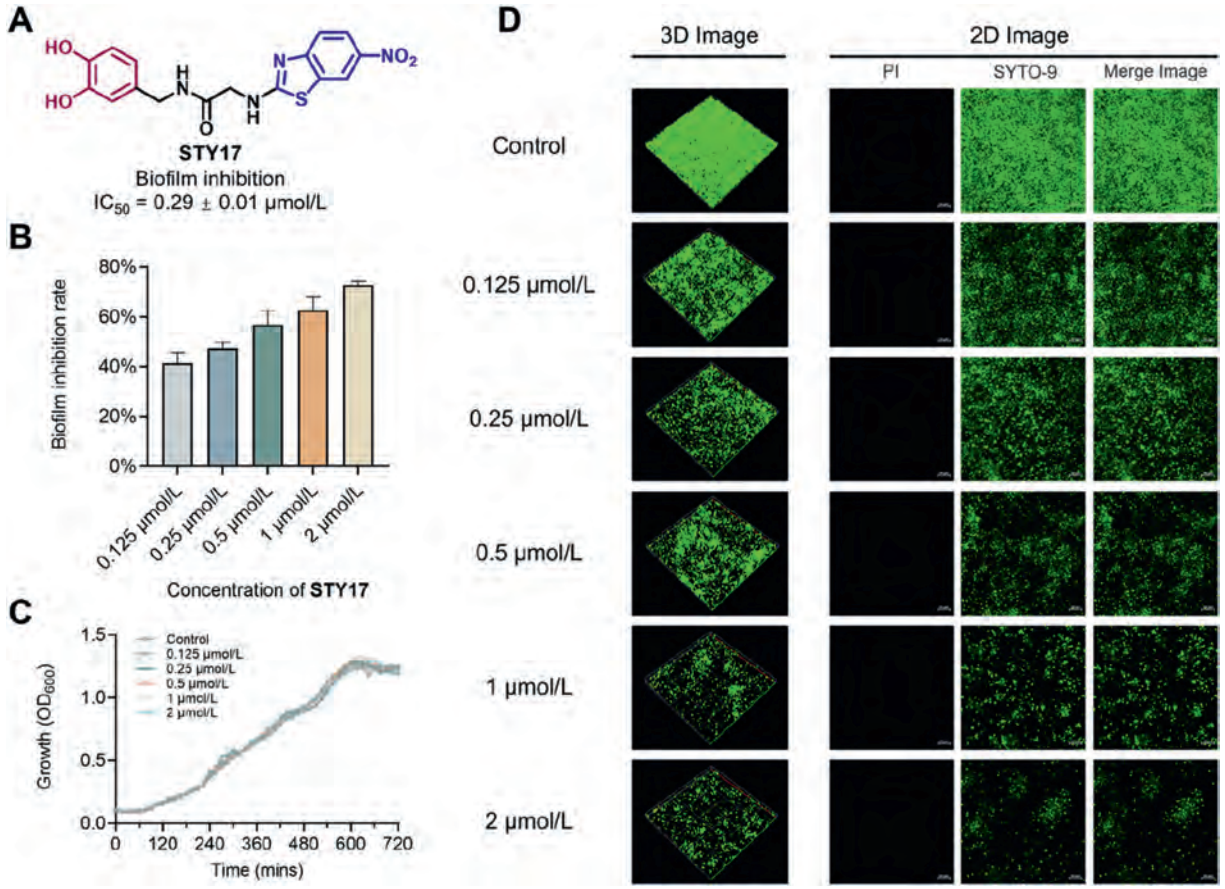

Figure 2 The effect of compound STY17 on biofilm formation of organized structures in *P. aeruginosa*. (A) The structure of the hit compound STY17. (B) The biofilm inhibition rate of compound STY17 at different concentrations. (C) The growth curve of *P. aeruginosa* PAO1 under the treatment of compound STY17. (D) CLSM images of biofilm in *P. aeruginosa* PAO1 treated with compound STY17. Data are presented as means ± SD of three biologically independent experiments. $^{*}P < 0.05$, $^{**}P < 0.01$, $^{***}P < 0.001$, and $^{****}P < 0.0001$.

in biofilm formation even in the presence of a high concentration of the compound STY17 (2 μmol/L) compared to untreated bacteria (Fig. 6B), suggesting that STY17 may have diminished efficacy in inhibiting biofilm formation in the *ΔsdhB* strain. Moreover, reverse transcription-polymerase chain reaction (RT-PCR) analysis of *sdhB* expression further supported the reduced SDH activity (Fig. 6C). To provide conclusive evidence for direct binding between SDH and the compound STY17, we next purified the SdhB membrane protein and performed microscale thermophoresis (MST) experiments following previously published methods[48]. As presented in Fig. 6J, the dissociation constant (K_d) for the binding of STY17 to SdhB was determined to be 5.44 ± 0.85 μmol/L, indicating a strong binding interaction between STY17 and SdhB. The disconnect between binding avidity and biofilm inhibitory potency may be attributed to the fact that SdhB is a functionally critical subunit in membrane protein SDH, the removal of SdhB from its native membrane-bound assembly and the loss of stabilizing inter-subunit interactions likely induce subtle conformational shifts or relaxation in the binding pocket. This approach may not fully replicate the lipid environment and the tightly assembled complex state present in the inner membrane of *P. aeruginosa*, leading to a higher K_d value for STY17 binding to SdhB than its IC_{50} of antibiofilm activity. In summary, these results indicated that STY17 potentially exerts its antibiofilm effects by inhibiting SDH in *P. aeruginosa*.

2.10. Compound STY17 disrupts SDH-mediated tricarboxylic acid cycle and electron transport chain

Succinate dehydrogenase is an enzyme involved in the tricarboxylic acid (TCA) cycle that uses iron as a cofactor[49]. Considering that the structure of the compound STY17 contains catechol chelating groups, we speculated that the inhibition of SDH may be attributed to the influence of STY17 on the iron-containing enzyme in *P. aeruginosa*. The restored fluorescence of Fe(III)-quenched CP654 probe (Fig. 6D)[50] and the reduced intracellular iron concentration (Fig. 6E) indicated that the compound STY17 is a high-affinity iron chelator, which may lead to iron deficiency in *P. aeruginosa* and impaired activity of iron-containing enzymes such as SDH.

SDH participates in the tricarboxylic acid (TCA) cycle and electron transport chain (ETC) to regulate biofilm formation[51]. To investigate the effects of STY17 on the respiratory chain and ETC, we tested bacterial respiration using the tetrazolium salt iodonitrotetrazolium chloride (INT), which can be reduced by respiratory chain dehydrogenases to a red insoluble formazan[52]. STY17 dose-dependently reduced INT reduction (Fig. 6F), indicating impaired respiratory chain and electron transport chain in *P. aeruginosa*. In addition, SDH-mediated TCA cycle and ETC promote the production of ATP and proton motive force (PMF), which provide energy and metabolic precursors for various

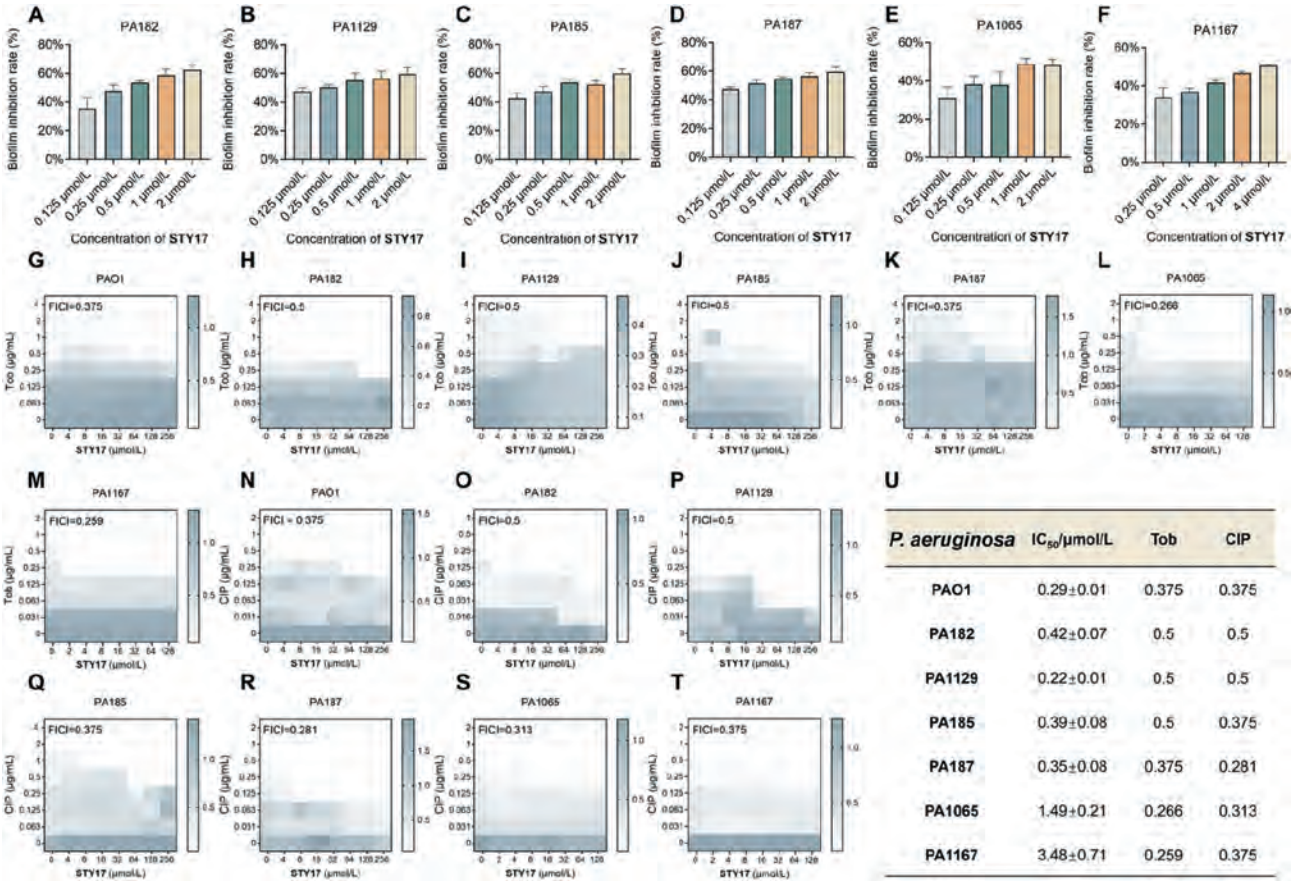

U

P. aeruginosa	IC_{50}/μmol/L	Tob	CIP
PAO1	0.29±0.01	0.375	0.375
PA182	0.42±0.07	0.5	0.5
PA1129	0.22±0.01	0.5	0.5
PA185	0.39±0.08	0.5	0.375
PA187	0.35±0.08	0.375	0.281
PA1065	1.49±0.21	0.266	0.313
PA1167	3.48±0.71	0.259	0.375

Figure 3 Compound STY17 synergizes with tobramycin and ciprofloxacin against clinically multidrug-resistant *P. aeruginosa.* Biofilm inhibition rate of compound STY17 at different concentrations against clinically isolated multidrug-resistant *P. aeruginosa* (A) PA182, (B) PA1129, (C) PA185, (D) PA187, (E) PA1065, and (F) PA1167. Compound STY17 exhibited synergy with tobramycin against *P. aeruginosa* (G) PAO1 and clinically isolated multidrug-resistant *P. aeruginosa* (H) PA182, (I) PA1129, (J) PA185, (K) PA187, (L) PA1065, and (M) PA1167. Compound STY17 exhibited synergy with ciprofloxacin against *P. aeruginosa* (N) PAO1 and clinically isolated multidrug-resistant *P. aeruginosa* strains (O) PA182, (P) PA1129, (Q) PA185, (R) PA187, (S) PA1065, and (T) PA1167. (U) Summary of the antibiofilm activity and synergistic effects of compound STY17 on tobramycin and ciprofloxacin. Data are presented as means ± SD of three biologically independent experiments. $*P < 0.05$, $**P < 0.01$, $***P < 0.001$, and $****P < 0.0001$.

cellular functions, including biofilm formation[53]. We determined PMF consisting of the transmembrane proton gradient (ΔpH) and potential ($\Delta\Psi$) using 2′,7′-bis-(2-carboxyethyl)-5-(and −6)-carboxyfluorescein acetoxymethyl ester (BCECF-AM) probe[54] and the dye thioflavin T (ThT)[55], respectively. In the presence of the compound STY17, the concentration-dependent decrease in the fluorescence intensity of BCECF-AM represented a significant decrease in cytoplasmic pH (Fig. 6H), whereas ThT exhibited strong fluorescence, representing a lower membrane potential of the cell (Fig. 6I). These results suggested that STY17 significantly impaired PMF in *P. aeruginosa*. Moreover, with the disruption of PMF by STY17, the ATP synthesis driven by it was also significantly reduced (Fig. 6G). Collectively, the above results revealed that compound STY17 may inhibit PMF homeostasis and ATP utilization by suppressing SDH-mediated TCA and ETC activity, thus disrupting biofilm formation.

2.11. Compound STY17 reduces the virulence and bacterial motility in P. aeruginosa

The energy and metabolic requirements of bacteria present in biofilms vary with complex environmental conditions, which in turn regulate the expression of various virulence determinants. Consequently, we determined the major virulence factors in *P. aeruginosa* PAO1 exposed to STY17. Extracellular polysaccharides (EPS), the main substances of biofilm formation and essential for biofilm adhesion and resilience, were significantly reduced by STY17 treatment (Fig. 7A), indicating potential inhibition of EPS synthesis within the biofilm matrix. In addition, with increasing concentrations of STY17, the secretion of elastase was significantly reduced in a concentration-dependent manner, and pyocyanin was slightly inhibited (Fig. 7B and C). This indicated that compound STY17 may reduce bacterial pathogenicity by inhibiting the production of virulence factors of *P. aeruginosa*. Moreover, bacteria must drive motility for initial colonization and adhesion to form biofilms. *P. aeruginosa* has three main types of motility, including swarming, swimming, and twitching, which were evaluated in our study. The presence of STY17 significantly reduced all three motilities, especially swarming motility, which was reduced by 80% by STY17 at a concentration of 2 μmol/L (Fig. 7D−G). Notably, swarming and twitching motility is dependent on type IV pili (T4P)[56,57], and then we observed the production of T4P using scanning electron microscopy (SEM). Fig. 7H showed that STY17 dramatically inhibited the

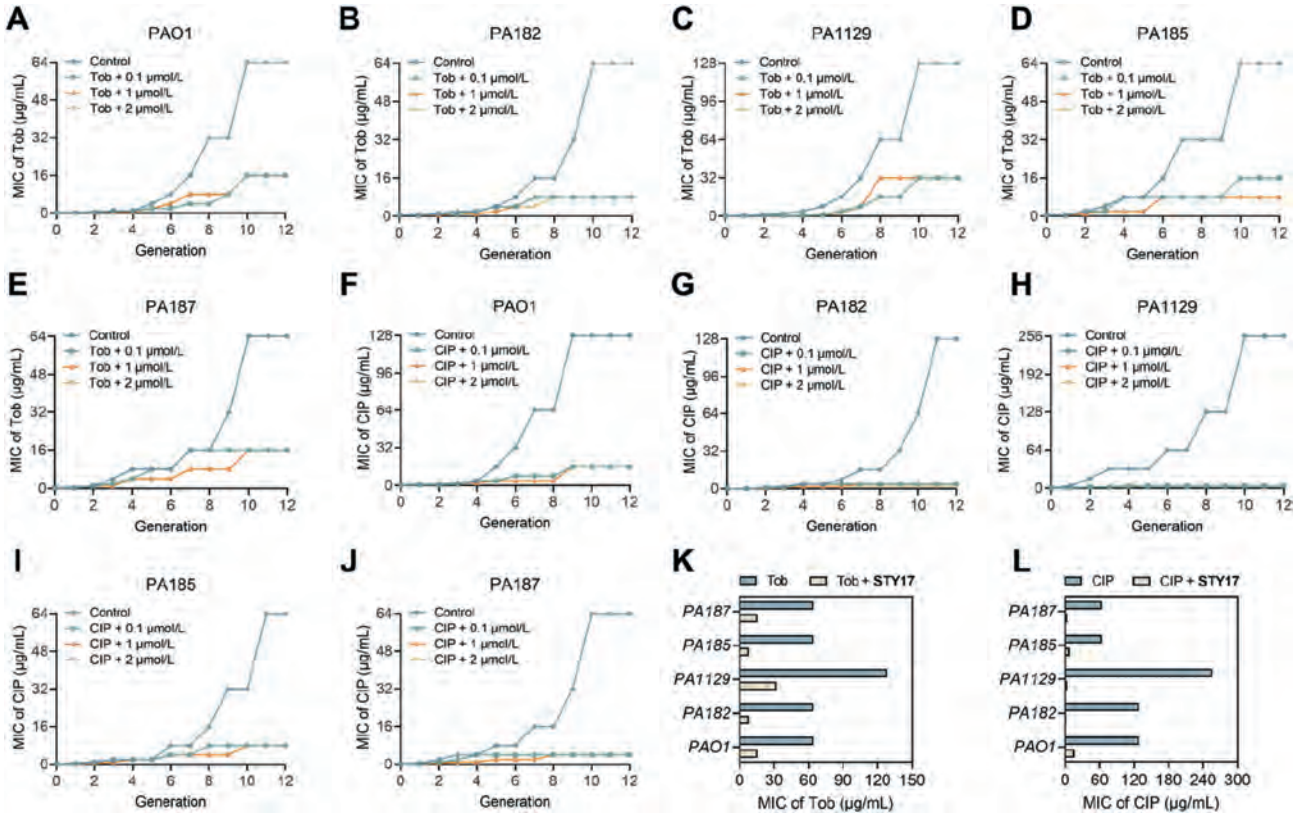

Figure 4 The effect of compound STY17 on the tobramycin and ciprofloxacin resistance in multidrug-resistant *P. aeruginosa.* MIC of Tob treated with or without compound STY17 in (A) PAO1, (B) PA182, (C) PA1129, (D) PA185, and (E) PA187. MIC of CIP treated with or without compound STY17 in (F) PAO1, (G) PA182, (H) PA1129, (I) PA185, and (J) PA187. MICs of (K) Tob and (L) CIP after 12 passages. Control was the group treated with Tob or CIP alone.

formation of pili in *P. aeruginosa* PAO1. These results indicated that STY17 may reduce bacterial motility by inhibiting the formation of pili, thereby disrupting the development of complex three-dimensional structures in biofilms. RT-PCR analysis (Fig. 6C) further demonstrated the inhibition of virulence and bacterial motility.

2.12. Compound STY17 has favorable safety profiles in vitro and in vivo

Next, we evaluated the safety profiles of STY17. *In vitro*, the toxicity of STY17 was determined by MTT assay on mouse macrophage cells (RAW264.7) and African green monkey kidney cells (Vero). There was no significant influence on the cell viability after treating these cells with different concentrations of STY17 for 24 h (Fig. 8A and B), demonstrating the favorable safety of STY17. As for the human breast cell line BT549, concentrations of STY17 as high as 100 μmol/L did not impair the viability of human BT549 cells (Supporting Information Fig. S4) or influence cellular iron levels (Supporting Information Fig. S5), which provided direct evidence that STY17 may not interfere with host iron homeostasis, aligning with a favorable safety profile. What's more, the hemolysis of rabbit (Fig. 8C) and mouse erythrocytes (Fig. 8D) induced by co-incubation with STY17 was less than 0.05%, indicating the excellent plasma stability of STY17. *In vivo*, no mortality was observed in zebrafish (Fig. 8E) or *Galleria mellonella* (Fig. 8F) treated with STY17 at concentrations exceeding 600-fold the IC_{50} (*i.e.*, 200 μmol/L). Taken together, these data highlighted the promising potential of STY17 as a potent and safe antibacterial adjuvant candidate.

2.13. Compound STY17 in combination with tobramycin and ciprofloxacin effectively resists P. aeruginosa infection in Galleria mellonella

Due to the safety profiles and antimicrobial synergistic potential of hit compound STY17, we next evaluated its efficacy as an antibacterial adjuvant *in vivo*. The easily infected *Galleria mellonella* has proved to be an ideal model for studying microbial pathogenesis, as it exhibits similar immune responses to vertebrates and mammals and is inexpensive[58]. Consequently, we sought to evaluate the synergistic potential of compound STY17 on Tob and CIP in *G. mellonella* infected by *P. aeruginosa* PAO1 (Fig. 9A). According to the Clinical and Laboratory Standards Institute (CLSI), the clinical resistance breakpoint for tobramycin is $\geq$ 4 μg/mL, and for ciprofloxacin is $\geq$ 2 μg/mL[59]. Thus, subtherapeutic concentrations of tobramycin (0.0025 mg/mL) and ciprofloxacin (0.001 mg/mL) were used in this study. Moreover, a maximum biofilm inhibition rate of STY17 was achieved at 2 μmol/L and thus was selected for the subsequent *in vivo* experiments to study the antibacterial synergistic effects of STY17 on tobramycin and ciprofloxacin. As displayed in Fig. 9B and C, untreated *G. mellonella* all died after 2 days of infection, whereas the compound STY17 prolonged their survivability to 3 days,

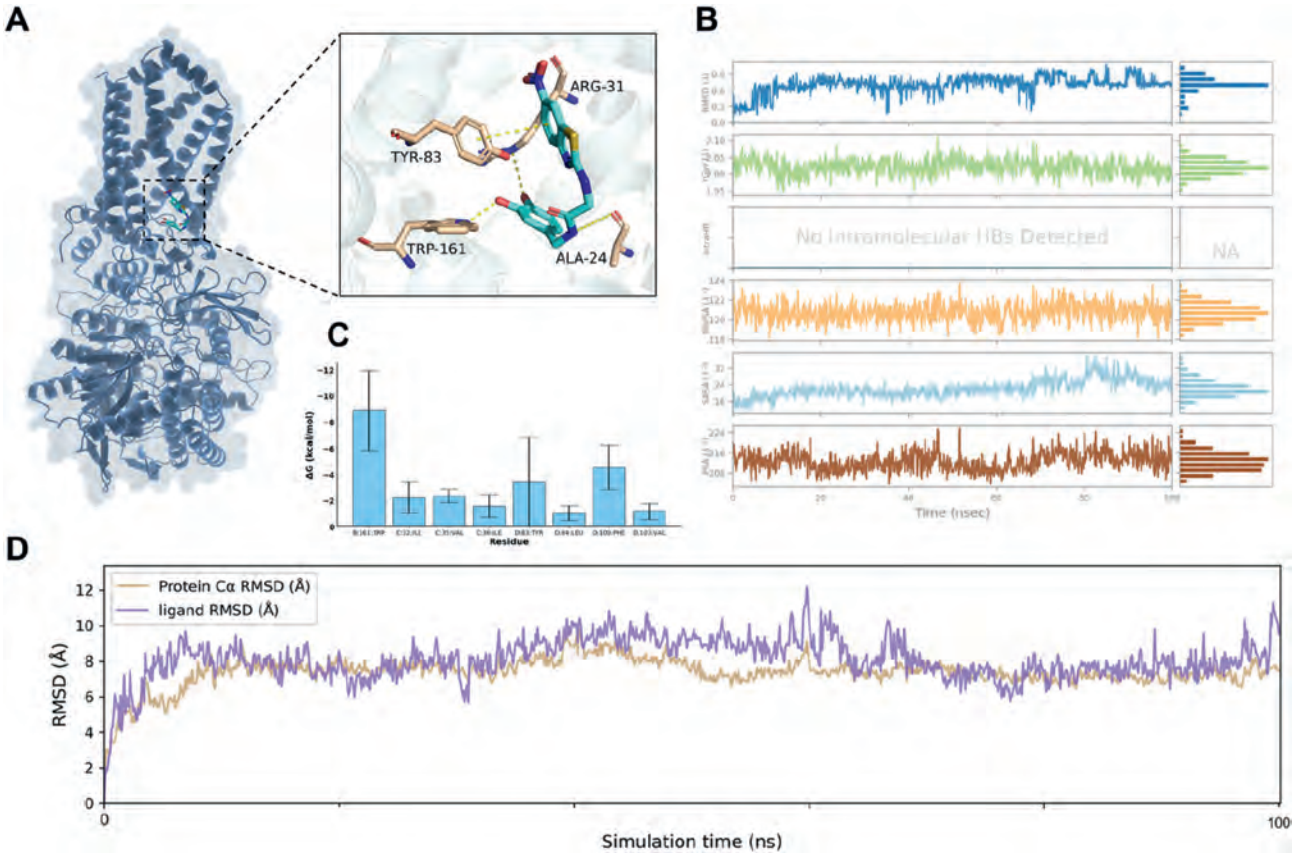

Figure 5 The binding study of STY17 with *P. aeruginosa* SDH *in silico*. (A) The binding site and key interactions between STY17 and SDH. (B) Dynamic properties of STY17 during the simulation. (C) Residue-based decomposition of binding free energy. (D) RMSD plot of Cα atoms of SDH and STY17 in MD simulation.

which may be attributed to the reduced virulence of the bacteria by STY17. Following injection with 0.0025 mg/mL tobramycin alone, *G. mellonella* larvae exhibited a survival rate of 40% after 5 days, whereas the addition of STY17 in combination with it consistently maintained 100% survival, suggesting that STY17 significantly enhances the antimicrobial activity of Tob. Similarly, the survival rate of *G. mellonella* was 30% after being treated with 0.001 mg/mL CIP monotherapy 5 days later, whereas the addition of STY17 in combination with it consistently maintained 100% survival, indicating a strong enhancement of antimicrobial activity on CIP by STY17 as well. Additionally, two other antibiotics, colistin (CST) and ceftazidime (CAZ), were employed for co-administration with STY17 and also revealed significant synergistic effects (Supporting Information Fig. S6A−S6D). With CST, STY17 increased the survival rate from 10% with CST alone to 80% in combination after five days. In the case of CAZ, it resulted in complete mortality within 2 days while its combination with STY17 led to 20% survival over five days. The above results demonstrated a broad synergistic applicability of STY17.

2.14. Compound STY17 in combination with tobramycin and ciprofloxacin effectively resists P. aeruginosa infection in mice

Given that *P. aeruginosa* is one of the common causes of wound infection, we also constructed a mouse wound infection model of *P. aeruginosa* to evaluate the synergistic efficacy of STY17 on Tob and CIP *in vivo*. Surface wounds were first created and the wound area was infected with *P. aeruginosa* PAO1, which was administered by direct droplet application of saline, antibiotics alone, or antibiotics combined with STY17 (Fig. 10A). After 3 consecutive days of treatment, we observed that the bacterial burden in the wounds of mice treated with STY17 alone (7.42-$\log_{10}$ CFU/mL) was comparable to that treated with saline (7.45-$\log_{10}$ CFU/mL), further verifying *in vivo* that the compound STY17 had no bactericidal effect (Fig. 10B and E). What's more, the bacterial level in wounds treated with 0.0025 mg/mL Tob alone was 6.66-$\log_{10}$ CFU/mL, while STY17 in combination with a subtherapeutic concentration of 0.0025 mg/mL Tob achieved a 1.46-$\log_{10}$ CFU/mL reduction of bacteria in wounds (5.20-$\log_{10}$ CFU/mL). Further, the wound healing rate of Tob-treated mice in the presence of STY17 was distinctly faster than that of Tob-treated mice alone (Fig. 10C and D). The above tests on bacterial burden and area in the wound revealed that STY17 enhanced the antimicrobial efficacy of Tob in the treatment of *P. aeruginosa* infections in mice.

The mice treated with STY17 and CIP produced similar results to those treated with Tob. Even at a lower subtherapeutic concentration of 0.001 mg/mL CIP, its combination with 2 μmol/L STY17 reduced bacterial load by an additional 1.11-$\log_{10}$ CFU/mL (Fig. 11A and D) compared to 0.001 mg/mL CIP treatment alone (6.47-$\log_{10}$ CFU/mL). Further, the wound healing rate of CIP-treated mice in the presence of STY17 was distinctly faster than that of CIP-treated alone (Fig. 11B and C), suggesting that compound STY17 enhanced the antimicrobial efficacy of CIP

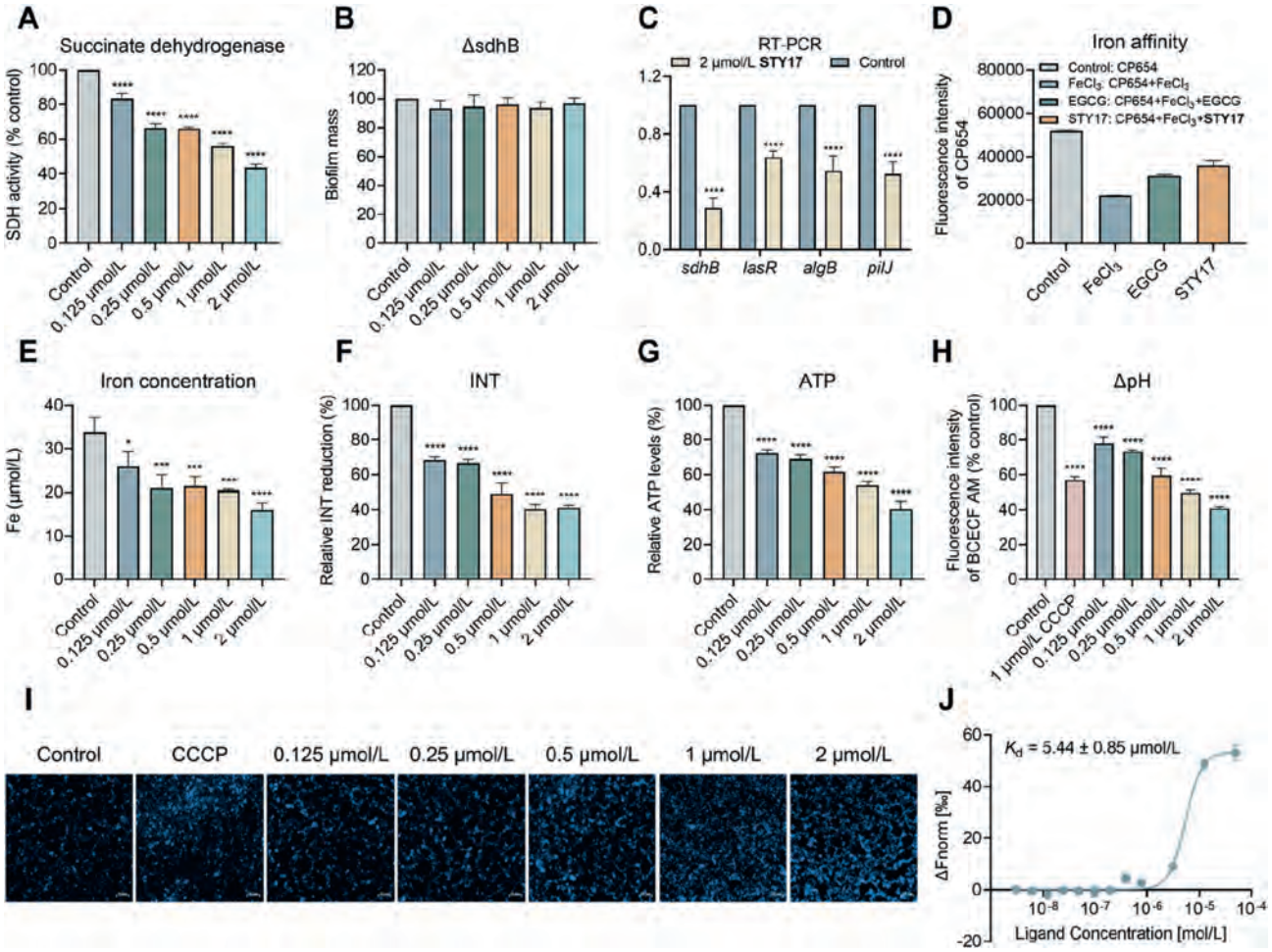

Figure 6 The effect of compound STY17 on SDH-mediated TCA and ETC. (A) The activity of SDH in *P. aeruginosa* strain PAO1 treated with different concentrations of STY17. (B) Evaluation of biofilm formation in *ΔsdhB* in the presence of compound STY17. (C) The results of RT-PCR on some related genes. (D) Assessment of the iron chelating ability of compound STY17, EGCG used as a positive control. (E) The iron concentration, (F) the relative INT reduction, (G) the relative ATP levels, and (H) pH in *P. aeruginosa* strain PAO1 under the treatment of STY17. (I) The potential of *P. aeruginosa* treated with STY17. (J) The binding of STY17 to SdhB was tested by MST experiments ($n = 3$). Control was the untreated group. Data are presented as means ± SD of three biologically independent experiments. $^{*}P < 0.05$, $^{**}P < 0.01$, $^{***}P < 0.001$, and $^{****}P < 0.0001$.

in the treatment of *P. aeruginosa* infections in mice. In addition, the analysis of weight (Supporting Information Fig. S7A and S7B) and hematoxylin−eosin (H&E) staining of major organs in mice (Supporting Information Fig. S8A and S8B) showed that STY17 had no toxicity to mice at therapeutic concentrations. In conclusion, the above results demonstrated the potential of STY17 to enhance the potency of Tob and CIP *in vivo*.

2.15. Compound STY17 in combination with tobramycin and ciprofloxacin effectively resists multidrug-resistant P. aeruginosa infection in mice

The results of *in vitro* standard checkerboard assays for antibacterial synergistic activities indicated (Fig. 3J, K, Q, and R) that STY17 demonstrated synergistic effects with Tob and CIP against multidrug-resistant isolates PA185 and PA187. Consequently, we further investigated the efficacy of STY17 in combination with Tob and CIP against PA185 and PA187 *in vivo* to evaluate the clinical application potential of STY17 in *P. aeruginosa* drug-resistant infections. As summarized in Fig. 12A and D, although STY17 monotherapy showed no antimicrobial effect, its combination with 0.0025 mg/mL Tob (5.84-$\log_{10}$ CFU/mL) produced an additional 1.14-$\log_{10}$ CFU/mL reduction in bacterial burden than Tob treatment alone (6.98-$\log_{10}$ CFU/mL). Similarly, its combination with 0.001 mg/mL CIP (5.91-$\log_{10}$ CFU/mL) resulted in an additional 0.92-$\log_{10}$ CFU/mL reduction compared to CIP monotherapy (6.83-$\log_{10}$ CFU/mL). Both combination therapies also significantly accelerated wound healing (Fig. 12B and C). These results suggested that STY17 enhanced the antimicrobial efficacy of Tob and CIP in the treatment of resistant *P. aeruginosa* infections *in vivo*.

Additionally, the evaluation against the multidrug-resistant *P. aeruginosa* strain PA187 also confirmed that STY17 synergized with subtherapeutic doses of Tob (0.0025 mg/mL) or CIP (0.001 mg/mL). The combinations produced additional bacterial load reductions of 0.95-$\log_{10}$ and 1.17-$\log_{10}$ CFU/mL, respectively, beyond antibiotic monotherapies (Fig. 13A and D), and significantly accelerated wound healing (Fig. 13B and C), demonstrating

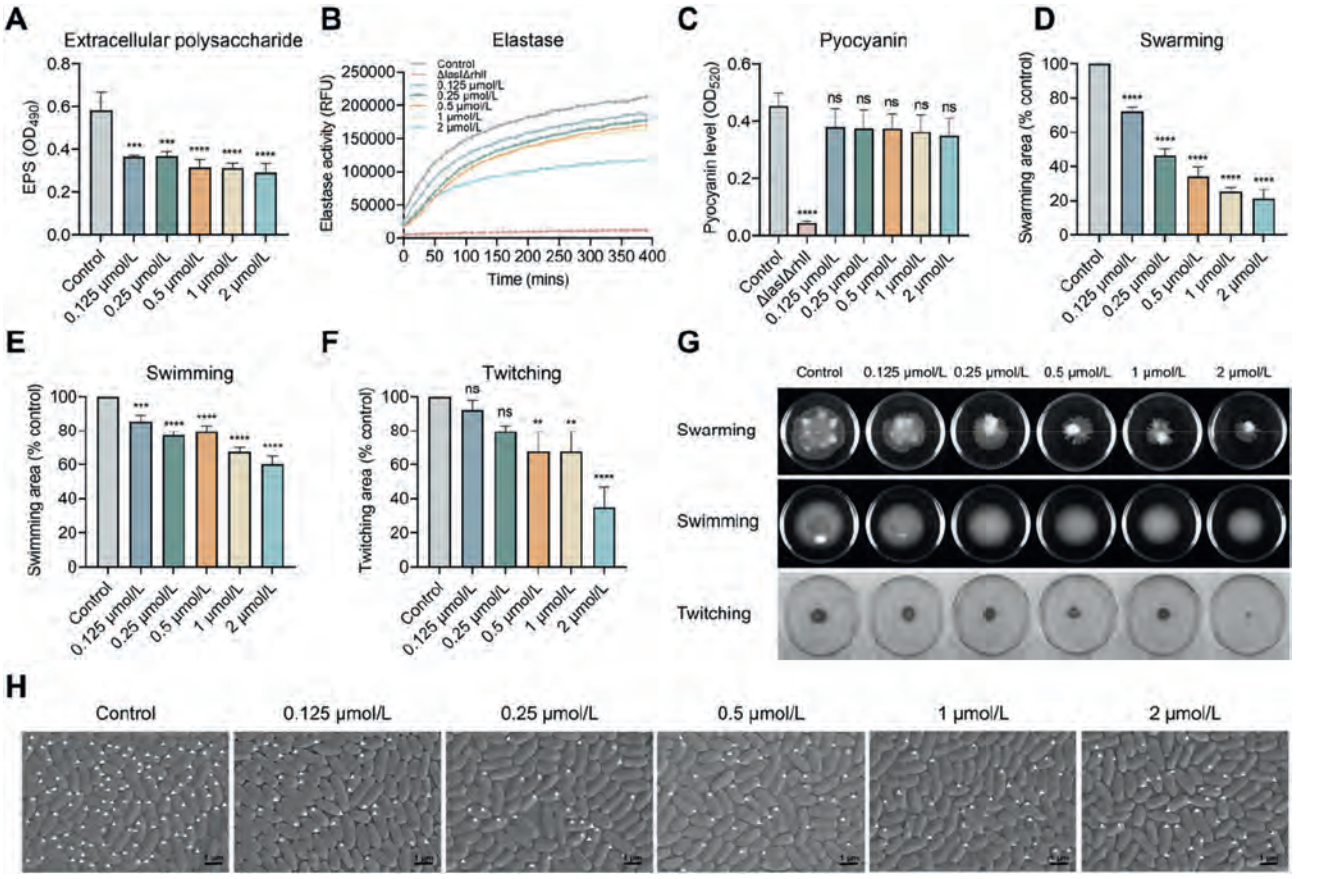

Figure 7 The effect of compound STY17 on virulence and bacterial motility in *P. aeruginosa*. The production of (A) EPS, (B) elastase, and (C) pyocyanin in *P. aeruginosa* PAO1 under the treatment of STY17 at 0.125, 0.25, 0.5, 1, and 2 μmol/L. The (D) swarming, (E) swimming, and (F) twitching areas of PAO1 that treated with STY17. (G) The swarming, swimming, and twitching motility of *P. aeruginosa* strain PAO1 under the treatment of STY17. (H) The formation of pili in PAO1 treated with STY17. Control was the untreated group. Data are presented as means ± SD of three biologically independent experiments. $*P < 0.05$, $**P < 0.01$, $***P < 0.001$, and $****P < 0.0001$.

its potential as an adjunctive therapy for resistant *P. aeruginosa* infections.

Collectively, the *in vivo* studies in a murine wound infection model revealed a promising therapeutic role for STY17, which functioned as a potent synergistic adjuvant to enhance the efficacy of Tob and CIP against multidrug-resistant *P. aeruginosa* infections. These results position STY17 as a compelling candidate for treating both conventional and resistant *P. aeruginosa* infections.

2.16. *The acute toxicity of STY17 in mice*

To clarify the safety range of therapeutic doses and potential toxicological effects of STY17, an acute toxicity studies were conducted in mice. Animals received single oral doses of STY17 at 50, 100, and 200 mg/kg, and were monitored for changes in body weight and behavioural status over 14 days. As summarized in Supporting Information Fig. S9A and S9C, all dose groups exhibited gradual body weight gain, with no mortality or behavioural abnormalities observed, indicating a good tolerance profile up to 200 mg/kg STY17. After 14 days of dosing, mice were euthanised. Representative organs (heart, liver, spleen, lungs, and kidneys) were collected, and histopathological analysis was performed on tissue sections stained with hematoxylin and eosin (H&E). As shown in Supporting Information Fig. S9B and S9D, H&E staining of tissue sections revealed no toxic effects or tissue damage attributable to STY17. Collectively, these results supported the safety profile of STY17 as a potential drug candidate.

2.17. *The pharmacokinetic properties of STY17*

To evaluate the pharmacokinetic properties (PK) of STY17, mice were treated with STY17 *via* intravenous (i.v. 10 mg/kg) and intraperitoneal administration (i.p. 10 mg/kg). As summarized in Table 4, STY17 displayed favorable pharmacokinetics following IP administration. The compound was rapidly absorbed with a maximum concentration (C_{max}) of 338 ng/mL reached at 0.19 h (T_{max} = 0.19 h). It exhibited a favorable systemic exposure (AUC_{last} = 525 h ng/mL), an acceptable terminal half-life ($t_{1/2}$ = 1.05 h), and a high bioavailability (F = 60.1%). For comparison, after i.v. administration, STY17 showed a C_0 of 10,833 ng/mL, an AUC_{last} of 880 h ng/mL, a $t_{1/2}$ of 1.29 h, and a clearance (CL) of 195 mL/min/kg. These collective PK findings provided a critical foundation for the subsequent studies of STY17.

3. Conclusions

Multidrug-resistant *P. aeruginosa* infections accompanied by biofilm-associated resistance have become a serious threat to public health[60]. The application of antibacterial adjuvants to

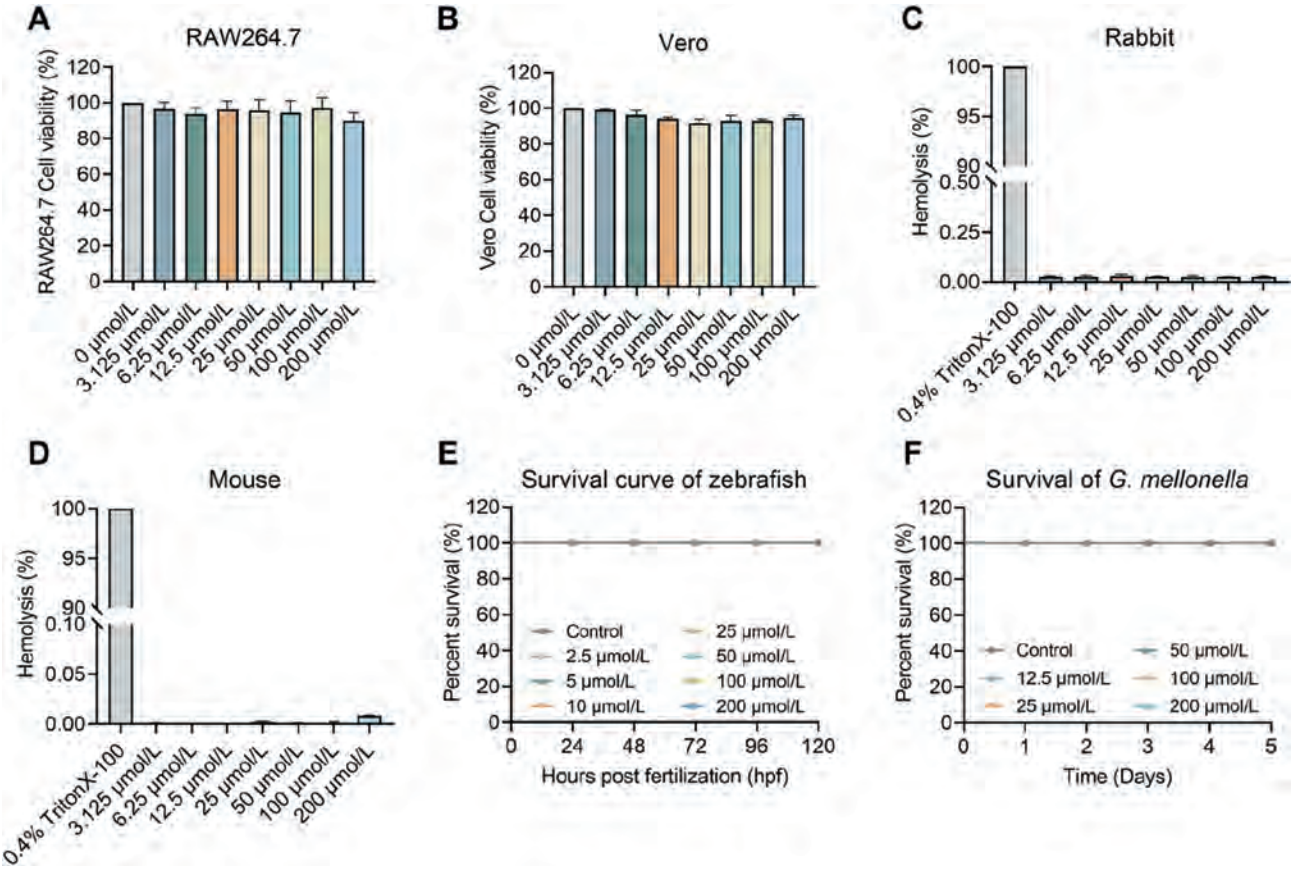

Figure 8 The safety profiles of compound STY17 *in vitro* and *in vivo*. Effects of STY17 on cell viability of (A) the RAW264.7 and (B) Vero cells. Assessment of hemolysis in (C) rabbit and (D) mouse under the treatment of STY17, 0.4% TritonX-100 was a positive control. Survival curves of (E) zebrafish and (F) *G. mellonella* after co-incubation with STY17. Control was the untreated group. Data are presented as means ± SD of three biologically independent experiments.

enhance the antibacterial activity of commonly used antibiotics has already demonstrated strong therapeutic potential in clinical studies. However, there is a shortage of commercially available antibacterial adjuvants against biofilm-associated *P. aeruginosa* infections, and the structural diversity of clinical candidate drugs is limited. Therefore, the identification of antibacterial adjuvants with new scaffolds and mechanisms to enhance antibiotic efficacy is urgently needed.

This study developed a generative active learning workflow to design new antibacterial adjuvants through an in-house compound repository of 725 biofilm inhibitors and a library of potential antibiofilm targets constructed from our previous work. The novel scaffold, comprised of the catechol and benzothiazole, was identified as a candidate. Further structural optimization and SAR analysis resulted in the hit compound STY17, which significantly inhibited *P. aeruginosa* biofilm formation at sub-micromolar concentrations. Notably, STY17 significantly inhibited biofilm formation, synergized with Tob and CIP, and suppressed the resistance development of both antibiotics against clinically multidrug-resistant *P. aeruginosa*, demonstrating its potential as an antibacterial adjuvant with Tob and CIP. Next, computerized molecular docking data and MST studies displayed a high affinity between STY17 and SDH, which resulted in a significant reduction of SDH activity in *P. aeruginosa*. The absence of antibiofilm activity of STY17 in SDH-deficient strains further verified the hypothesis that the inhibition of biofilm by STY17 derives from the impairment of SDH. SDH is an iron-containing enzyme that is involved in the TCA cycle and ETC, affecting the metabolic status of bacteria, triggering their adaptive responses, and inducing biofilm formation or dispersal. Subsequent exploration indicated that the influence of STY17 on SDH might be attributed to an intracellular iron deficiency in *P. aeruginosa*. Thus, the impaired activity of SDH further led to the impairment of TCA, ETC, and biofilm formation.

In addition, STY17 reduces bacterial pathogenicity by decreasing the production of virulence factors such as elastase and EPS in *P. aeruginosa*, it also inhibits bacterial motility by inhibiting the formation of pili, so that biofilm colonization is limited. STY17 exhibited a favorable safety profile *in vitro* and *in vivo*, as it did not cause cell death or erythrocyte hemolysis, nor did it cause mortality in zebrafish and *G. mellonella* at up to 200 μmol/L. In a *G. mellonella* infection model, the combination of STY17 with Tob and CIP treatment raised the survival rate of *G. mellonella* to 100% compared with the application of antibiotics alone. In a mouse wound infection model, STY17 significantly improved the effect of Tob and CIP to reduce bacterial burden in the wound

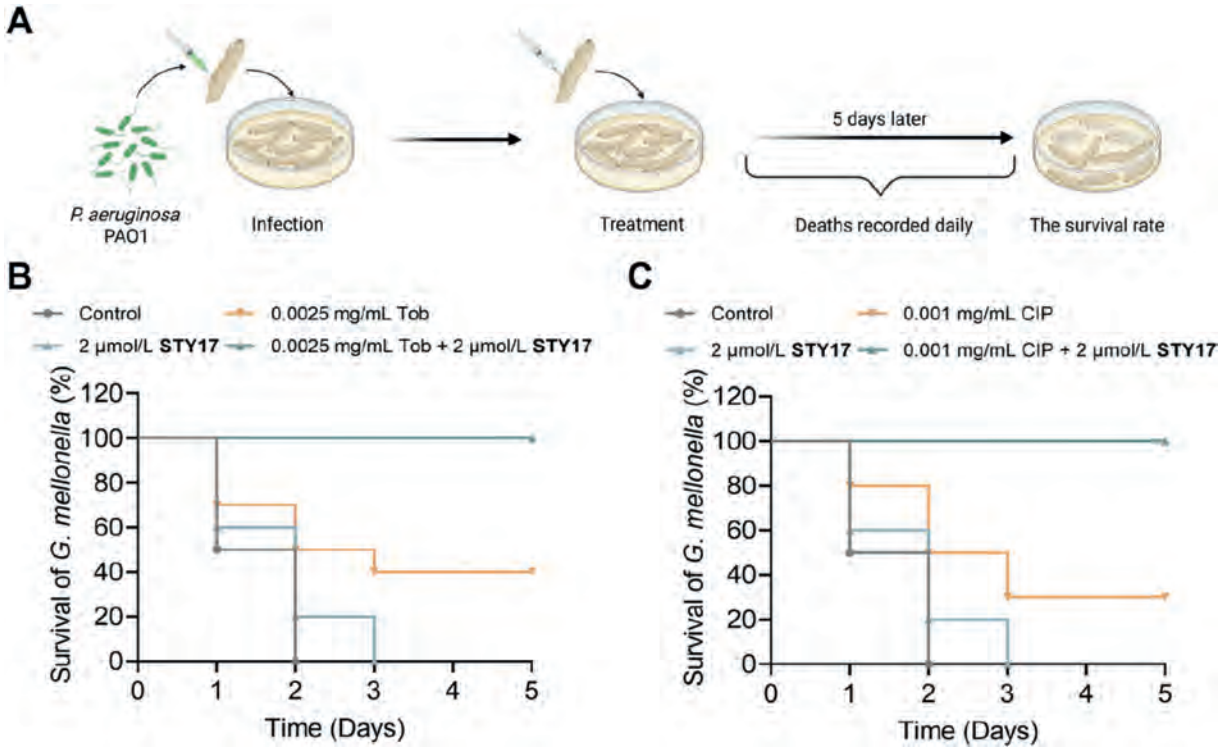

Figure 9 The synergistic effect of compound STY17 in combination with Tob and CIP against *P. aeruginosa* infection in *Galleria mellonella*. (A) The experimental process of the *G. mellonella* infected model. (B) The survival of *G. mellonella* infected by PAO1 after being treated with PBS containing 0.1% DMSO (control), STY17, Tob, and Tob in combination with STY17. (C) The survival of *G. mellonella* infected by PAO1 after being treated with PBS containing 0.1% DMSO (control), STY17, CIP, and CIP in combination with STY17.

with a 0.92−1.46-$\log_{10}$ CFU/mL reduction compared with the application of antibiotics alone, demonstrating a favorable antimicrobial synergistic effect.

In summary, these findings emphasized the utility of machine learning in discovering desirable new chemotypes, especially against challenging pathogens such as multidrug-resistant *P. aeruginosa*, and identified STY17 as a promising antibacterial adjuvant. This approach further unveils SDH as a potential target for next-generation adjuvants, providing a rational design strategy to overcome the limitations of current antibiotic therapies. Looking forward, future research will focus on elucidating the precise molecular mechanism of STY17 by determining its co-structure with SDH, optimizing its pharmacokinetic and safety profiles through structural refinement, and expanding its application to enhance the efficacy of existing antibiotics against a broader spectrum of resistant bacterial pathogens.

4. Experimental

4.1. Computational methods

Molecular Standardization of the in-house database: The items of the in-house database are listed in Supporting Information Table S1. This database integrates compounds (725 structures) from our prior publications, which act on targets within critical biofilm modulation pathways such as the *las*, *rhl*, *pqs* systems, and iron uptake systems. To ensure consistency and chemical accuracy, all molecular entries in the database (encoded as SMILES strings) were subjected to a standardized preprocessing workflow using RDKit. The standardization pipeline included: (i) normalization of functional groups; (ii) removal of counterions and selection of the main organic component; (iii) neutralization of formal charges; and (iv) generation of canonical tautomeric forms. This protocol ensured uniform representation of chemical structures for downstream analyses.

ChemProp, which employs a directed message-passing neural network (D-MPNN), was used to construct chemical property prediction models. The model serves as a fixed surrogate (retaining its original algorithm and hyperparameters) throughout the workflow. The initial QSAR model for biofilm inhibition was developed using 725 in-house chemical library structures. Implemented as a scoring plug-in within REINVENT's molecular generation module, this model provides directional guidance for generated molecules. The analysis in Supporting Information Table S2 compares the properties of the generated batches against the training set to address overfitting and demonstrate the generative model's ability to explore novel chemical space.

The complete amino acid sequences of all four subunits of *P. aeruginosa* succinate dehydrogenase (SDH) were retrieved from the UniProt database (Q9I3D5, Q9I3D4, Q9I3D7 and Q9I3D6). Structural prediction was performed using ColabFold Multimer, and the top-ranked model was selected for further processing. The protein structure was prepared using the Protein Preparation Wizard in Maestro, with cofactors manually added based on the homologous *E. coli* Sdh crystal structure. The resulting complex was subjected to initial energy minimization using the OPLS4 force field, followed by structural relaxation *via* molecular dynamics (MD) simulation. An orthorhombic solvent box containing

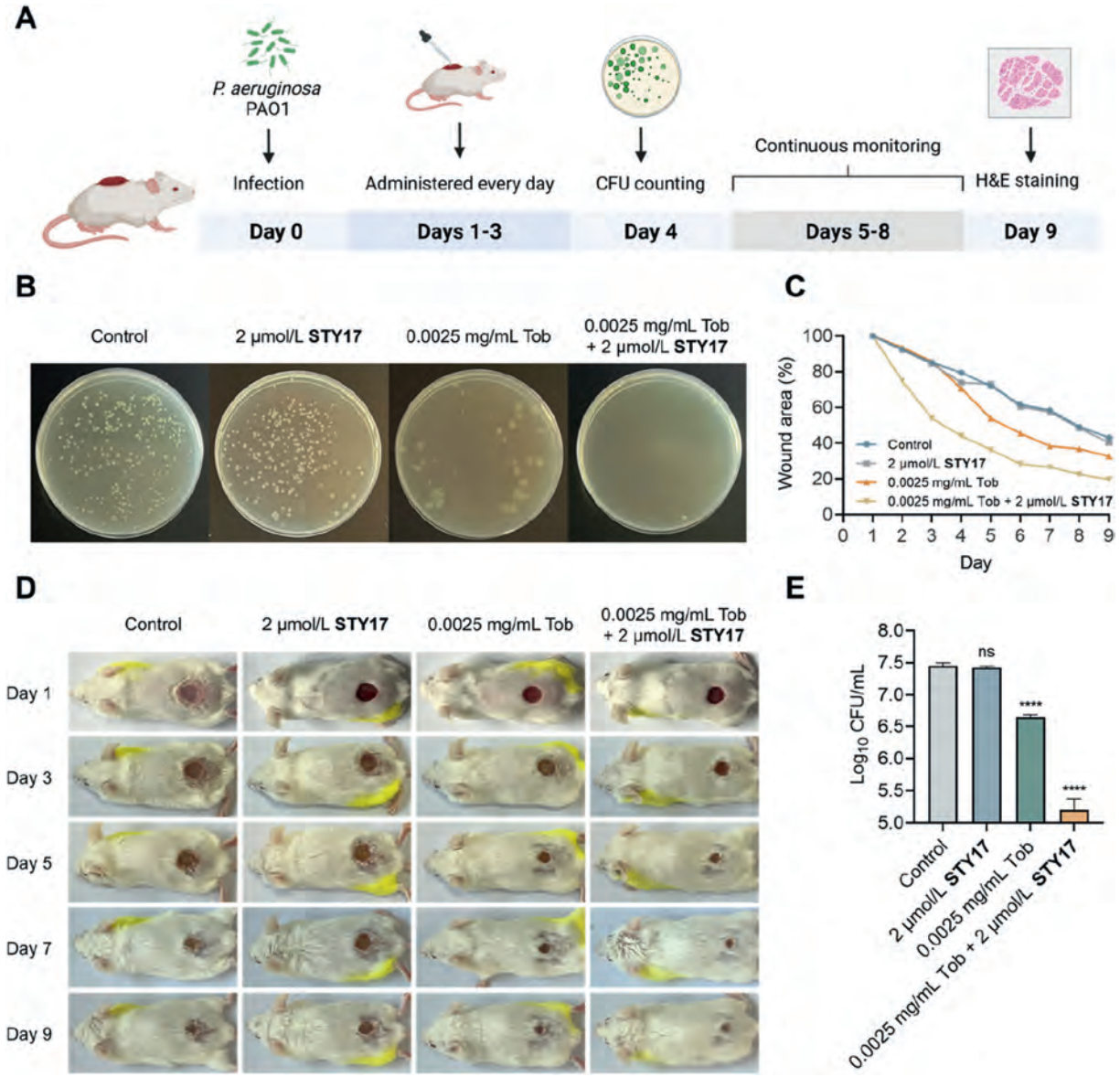

Figure 10 Compound STY17 in combination with Tob effectively resists *P. aeruginosa* PAO1 infection in mice. (A) The experimental process of the mouse wound-infected model. (B) The bacterial growth in the wound of mice after 3 consecutive days of treatment, including saline containing 0.1% DMSO, 2 μmol/L STY17, 0.0025 mg/mL Tob, and 0.0025 mg/mL Tob + 2 μmol/L STY17. (C) The wound area of mice during Days 1−9. (D) The representative images of wounds in mice during Days 1−9. (E) Quantitative analysis of bacterial growth in the wound of mice after 3 consecutive days of treatment. Data are presented as means ± SD of three biologically independent experiments. $^{*}P < 0.05$, $^{**}P < 0.01$, $^{***}P < 0.001$, and $^{****}P < 0.0001$.

SPC water molecules, counterions, and 0.15 mol/L NaCl was generated using the Desmond System Builder[61]. After standard minimization and equilibration, a 100 ns MD simulation was performed, and the equilibrium structure was extracted for virtual screening.

Docking and reverse docking were performed using the Glide module[62], and XGLIDE protocol. Molecules were then docked into the ubiquinone-binding site using Glide XP mode for binding affinity assessment. Selected compounds showing favorable docking scores were further validated by molecular dynamics simulations to evaluate the stability of binding, and their binding free energies were computed using the MM-GBSA method[63] based on the equilibrated MD trajectories.

4.2. *Chemical reagents and general method*

Unless otherwise stated, all experimental substances were obtained from Bide Pharmatech Ltd., Shanghai Macklin Biochemical Co., Ltd. or other commercial reagent vendors and were ready for use without further purification. The ^{1}H NMR and ^{13}C NMR spectra of the compounds were recorded on Bruker AVANCE III HD 400 MHz with DMSO-d_6 as a solvent. The purity of the final compounds (>95%) was determined by HPLC (Thermo Scientific Dionex Ultimate 3000 series) using a reversed-phase C18 column with the mobile phase consisting of 70% methanol and 30% pure water. The high-resolution mass spectra (HRMS) were recorded using SHIMADZU LCMS-9030, Thermo Q Exactive Plus, and

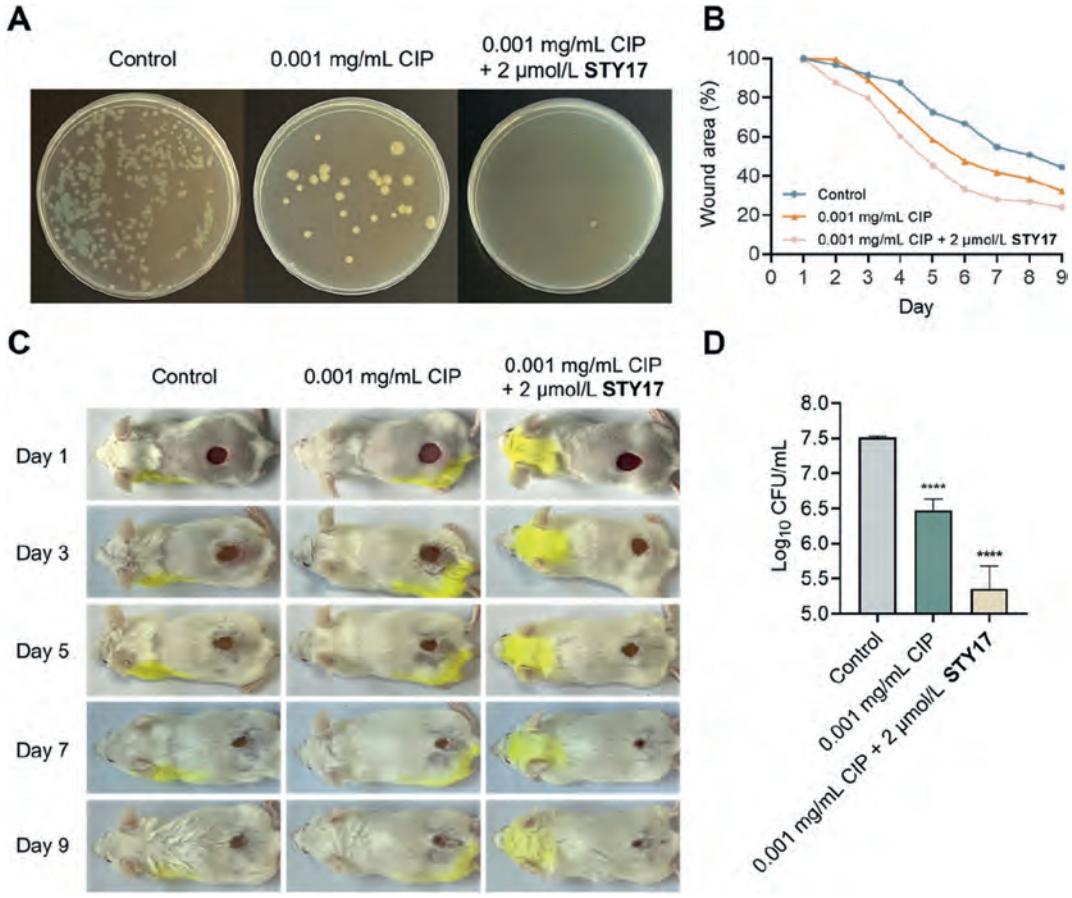

Figure 11 Compound STY17 in combination with CIP effectively resists *P. aeruginosa* PAO1 infection in mice. (A) The bacterial growth in the wound of mice after 3 consecutive days of treatment, including saline containing 0.1% DMSO, 0.001 mg/mL CIP, and 0.001 mg/mL CIP + 2 μmol/L STY17. (B) The wound area of mice during Days 1−9. (C) The representative images of wounds in mice during Days 1−9. (D) Quantitative analysis of bacterial growth in the wound of mice after 3 consecutive days of treatment. Data are presented as means ± SD of three biologically independent experiments. $^{*}P < 0.05$, $^{**}P < 0.01$, $^{***}P < 0.001$, and $^{****}P < 0.0001$.

Agilent 6210 series LC/MSD TOF mass spectrometer. These results were shown in Supporting Information Figs. S10−S173.

4.2.1. Preparation of key intermediates

*General procedure for preparation of intermediates **3a−3k**.* A solution of 2-amino-benzothiazole (150.00 mg, 1.00 mmol) and 3,4-dimethoxyphenylacetic acid (235.10 mg, 1.20 mmol) in 5 mL of DCM was treated with HATU (456.30 mg, 1.20 mmol) and DIPEA (0.50 mL, 3.00 mmol). The reaction mixture was stirred at room temperature for 12 h. Upon reaction completion, the solution was sequentially extracted with DCM, washed with water, dried with anhydrous Na_2SO_4, and purified by column chromatography (PE/EA = 2/1), the compound **3a** was collected as a white solid. Compounds **3b−3k** were synthesized in the same way as compound **3a**.

*General procedure for preparation of 3,4-dihydroxyphenylacetic acid (**4**).* A solution of 3,4-dimethoxyphenylacetic acid (200.00 mg, 1.02 mmol) in DCM (6 mL) was treated dropwise with BBr_3 (0.55 mL, 6.12 mmol) under an argon atmosphere. The reaction mixture was stirred at 0 °C for 1 h. Upon reaction completion, it was quenched by adding 3 mL of iced water, and the reaction solution was sequentially extracted with DCM, washed with water and dried with anhydrous Na_2SO_4. The compound **4** was collected as a white solid.

*General procedure for preparation of tert-butyl (2-((3,4-dimethoxybenzyl)amino)-2-oxoethyl)carbamate (**7**).* A solution of 3,4-dimethoxybenzylamine (1.00 g, 5.98 mmol) and *N*-Boc-glycine (1.26 g, 7.18 mmol) in DCM (15 mL) was treated with HATU (2.73 g, 7.18 mmol) and DIPEA (3.1 mL, 17.94 mmol). The reaction mixture was stirred at room temperature for 12 h. Upon reaction completion, the reaction liquid was sequentially extracted with DCM, washed with water, dried with anhydrous Na_2SO_4, and purified by column chromatography (PE/EA = 1/1), the intermediate **7** was collected as a white viscous solid.

*General procedure for preparation of 2-amino-N-(3,4-dimethoxybenzyl)acetamide (**8**).* Intermediate **7** in 36 mL DCM was treated dropwise with 4 mL trifluoroacetic acid, and the reaction was stirred at room temperature for 3 h. Upon completion, the reaction mixture was neutralized to pH 7−8 with aqueous NaOH, and the solution was extracted with DCM. The organic phase was dried over anhydrous Na_2SO_4 and concentrated under reduced pressure to collect compound **8** as a white solid.

*General procedure for preparation of intermediates **10a−10p**.* The commercially available compound 2-chlorobenzothiazole (150.00 mg, 0.88 mmol) and compound **8** (297.50 mg, 1.33 mmol) in 5 mL ethanol were treated with DIPEA (0.23 mL, 1.33 mmol) at 80 °C for 12 h. Upon completion, a white solid was precipitated, and compound **10a** was obtained as a white solid by

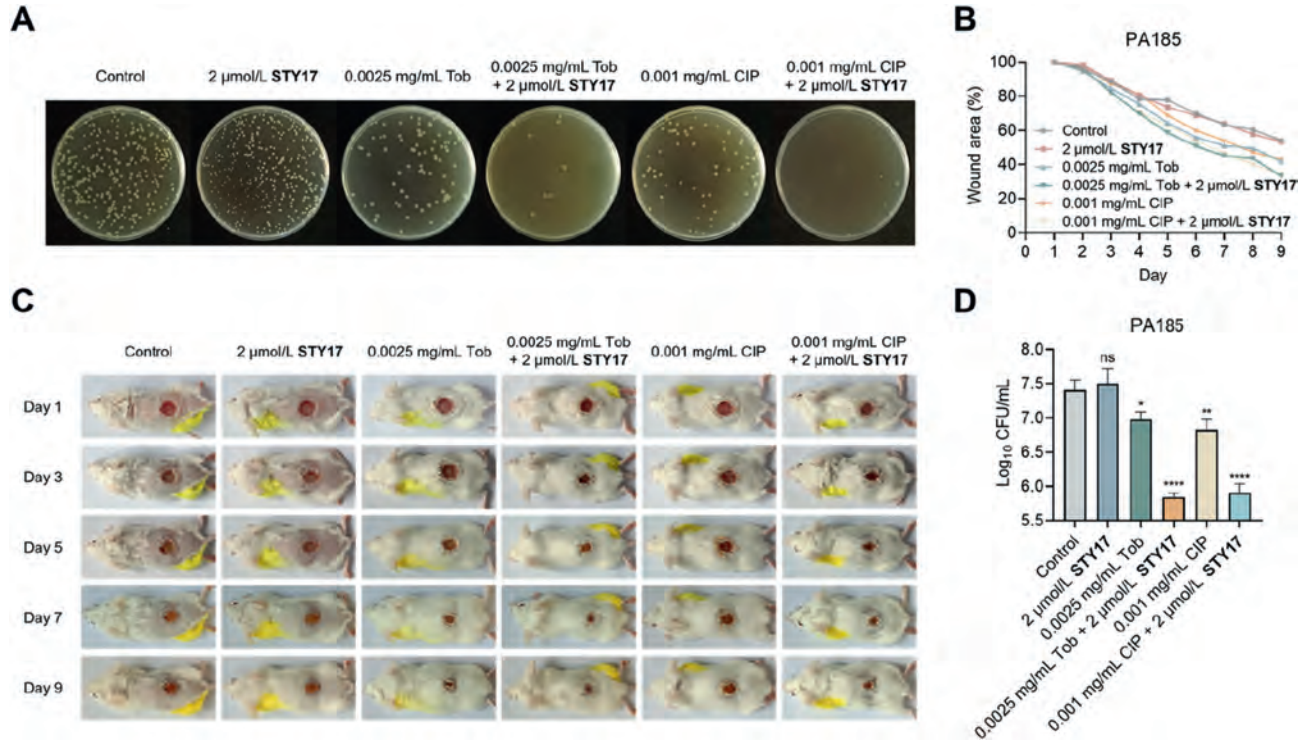

Figure 12 Compound STY17 in combination with Tob and CIP effectively resists the multidrug-resistant *P. aeruginosa* PA185 infection in mice. (A) The bacterial growth in the wound of mice under different treatments, including saline containing 0.1% DMSO, 2 μmol/L STY17, 0.0025 mg/mL Tob, 0.0025 mg/mL Tob + 2 μmol/L STY17, 0.001 mg/mL CIP, and 0.001 mg/mL CIP + 2 μmol/L STY17. (B) The wound area of mice during Days 1−9. (C) The representative images of wounds in mice during Days 1−9. (D) Quantitative analysis of bacterial growth in the wound of mice after 3 consecutive days of treatment. Data are presented as means ± SD of three biologically independent experiments. $^{*}P < 0.05$, $^{**}P < 0.01$, $^{***}P < 0.001$, and $^{****}P < 0.0001$.

diafiltration. Compounds **10b−10p** were synthesized in the same way as **10a**.

*General procedure for preparation of intermediates **12a−12f***. A solution of (3,4-dimethoxyphenyl)methanamine (1.00 g, 5.98 mmol) and *N*-Boc-glycine (1.26 g, 7.18 mmol) in 15 mL DCM was treated with HATU (2.73 g, 7.18 mmol) and DIPEA (3.1 mL, 17.94 mmol). The reaction was carried out at room temperature for 12 h. Upon completion, the reaction liquid was sequentially extracted with DCM, washed with water, and dried with anhydrous Na_2SO_4. Subsequently, purification by column chromatography (PE/EA = 1/1) afforded intermediate **12a** as a white viscous solid. Compounds **12b−12f** were synthesized in the same way as **12a**.

*General procedure for preparation of intermediates **13a−13f***. Intermediate **12a** in 36 mL DCM was treated dropwise with 4 mL trifluoroacetic acid, and the reaction was stirred at room temperature for 3 h. Upon completion, the reaction mixture was neutralized to pH 7−8 with aqueous NaOH. Subsequently, the solution was extracted with 30 mL DCM, the organic phase was dried with anhydrous Na_2SO_4, and the compound **13a** was collected as a white solid. Compounds **13b−13f** were synthesized in the same way as **13a**.

*General procedure for preparation of 4-((3,4-dimethoxybenzyl)amino)-4-oxobutanoic acid (**16**).* 3,4-dimethoxybenzylamine (0.50 mL, 3.00 mmol) (**6**) was dissolved with succinic anhydride (0.33 g, 3.30 mmol) in DCM, triethylamine was added as a base and stirred at room temperature for 1 h. Upon completion of the reaction, the solvent was removed by concentration under reduced pressure to give a white intermediate **16**.

*General procedure for preparation of intermediates **18a−18h.*** Intermediate **16** (0.15 mg, 0.56 mmol) was dissolved in DCM with aniline (62.35 mg, 0.67 mmol) (**17a**). HATU (319.40 mg, 0.84 mmol) and Et_3N (0.08 mL, 0.84 mmol) were added as coupling reagents and stirred at room temperature for 6 h. Upon completion of the reaction, extraction was carried out with DCM (30 mL × 3) and washed with saturated NaCl solution (30 mL × 3), and the organic phase was dried with anhydrous sodium sulfate and purified by column chromatography isolation to obtain the intermediates **18a**. Compounds **18b−18h** were synthesized in the same way as **18a**.

4.2.2. Synthesis of target compounds STY1−STY11

Intermediate **3a** (109.44 mg, 0.32 mmol) was dissolved in DCM and 1 mol/L BBr_3 (1.92 mL, 1.92 mmol) was slowly added dropwise under an ice bath. After the reaction for 30 min, the reaction was quenched by the addition of ice water. The product STY1 was collected by filtration. The compounds STY2−STY11 were obtained in the same synthetic method as compound STY1 using intermediates **3b−3k** as the reactants.

2-(3,4-Dihydroxyphenyl)-N-(4-methylbenzo[d]thiazol-2-yl)acetamide (STY1). White solid 40.90 mg, yield: 56%. HPLC purity: 96.26%. ^{1}H NMR (400 MHz, DMSO-d_6) δ 12.57 (s, 1H), 8.90 (s, 1H), 8.80 (s, 1H), 7.76 (d, J = 9.3 Hz, 1H), 7.25 (d, J = 7.3 Hz, 1H), 7.19 (m, 1H), 6.77 (d, J = 2.1 Hz, 1H), 6.68 (d, J = 7.9 Hz, 1H), 6.60 (dd, J = 8.1, 2.2 Hz, 1H), 3.60 (s, 2 H), 2.57 (s,

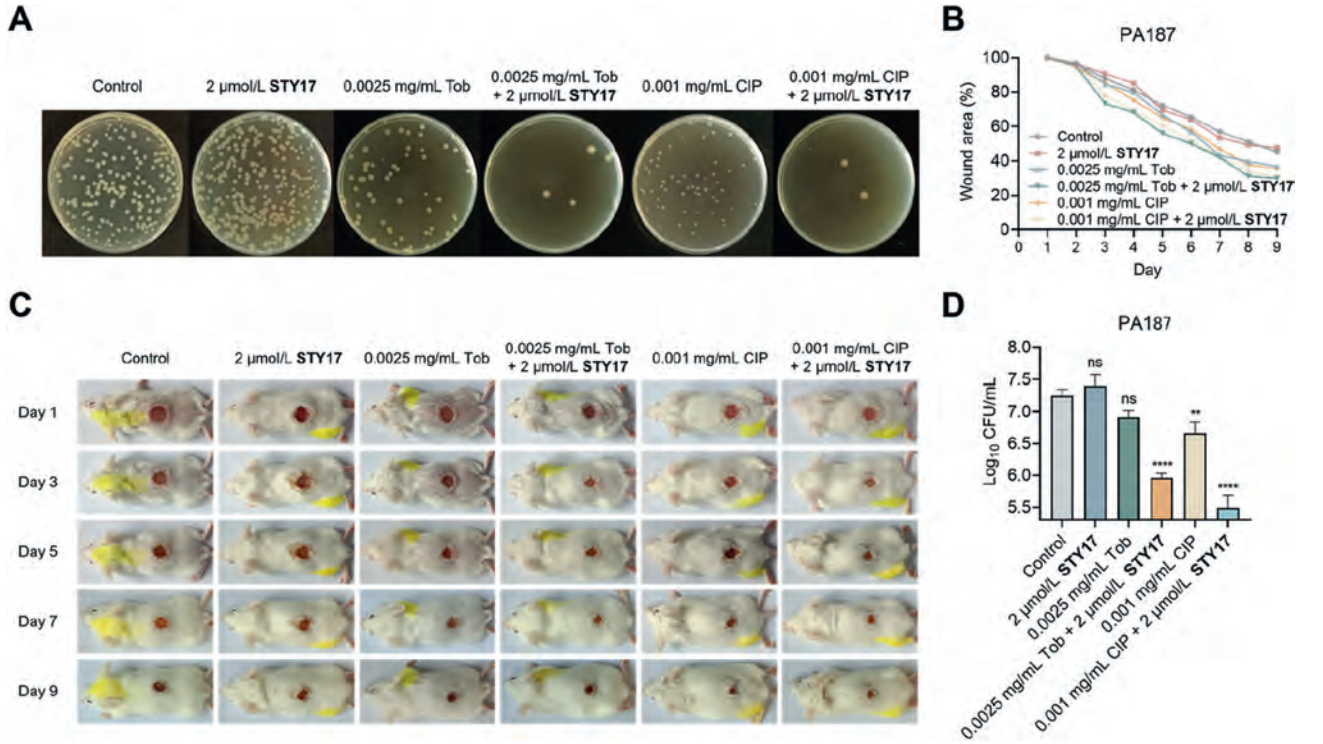

Figure 13 Compound STY17 in combination with Tob and CIP effectively resists the multidrug-resistant *P. aeruginosa* PA187 infection in mice. (A) The bacterial growth in the wound of mice under different treatments, including saline containing 0.1% DMSO, 2 μmol/L STY17, 0.0025 mg/mL Tob, 0.0025 mg/mL Tob + 2 μmol/L STY17, 0.001 mg/mL CIP, and 0.001 mg/mL CIP + 2 μmol/L STY17. (B) The wound area of mice during Days 1−9. (C) The representative images of wounds in mice during Days 1−9. (D) Quantitative analysis of bacterial growth in the wound of mice after 3 consecutive days of treatment. Data are presented as means ± SD of three biologically independent experiments. $^{*}P < 0.05$, $^{**}P < 0.01$, $^{***}P < 0.001$, and $^{****}P < 0.0001$.

3H). ^{13}C NMR (101 MHz, DMSO-d_6) δ 171.07, 157.57, 148.03, 145.57, 144.77, 131.51, 130.22, 127.05, 125.86, 123.92, 120.50, 119.52, 117.00, 115.95, 41.78, 18.43. HRMS (ESI) of compound STY1: calcd for $C_{16}H_{15}N_2O_3S$ $[M + H]^+ = 315.0798$, found $[M + H]^+ = 315.0792$.

2-(3,4-Dihydroxyphenyl)-N-(4-methoxybenzo[d]thiazol-2-yl)acetamide (STY2). White solid 25.70 mg, yield: 46%. HPLC purity: 96.49%. ^{1}H NMR (400 MHz, DMSO-d_6) δ 12.62 (s, 1H), 8.89 (s, 2H), 7.50 (d, J = 7.9 Hz, 1H), 7.24 (t, J = 8.0 Hz, 1H), 6.98 (d, J = 8.1 Hz, 1H), 6.76 (s, 1H), 6.68 (d, J = 8.1 Hz, 1H), 6.60 (d, J = 8.2 Hz, 1H), 3.91 (s, 3H), 3.59 (s, 2H). ^{13}C NMR (101 MHz, DMSO-d_6) δ 170.89, 156.87, 152.26, 145.58, 144.79, 138.81, 133.22, 125.78, 124.93, 120.49, 117.03, 115.98, 113.96, 108.12, 56.27, 41.84. HRMS (ESI) of compound STY2: calcd for $C_{16}H_{15}N_2O_4S$ $[M + H]^+ = 331.0748$, found $[M + H]^+ = 331.0745$.

N-(5-Chlorobenzo[d]thiazol-2-yl)-2-(3,4-dihydroxyphenyl)acetamide (STY3). White solid 20.00 mg, yield: 61%. HPLC purity: 95.04%. ^{1}H NMR (400 MHz, DMSO-d_6) δ 12.45 (s, 1H), 8.87 (s, 2H), 8.00 (d, J = 8.4 Hz, 1H), 7.80 (s, 1H), 7.34 (d, J = 8.4 Hz, 1H), 6.75 (s, 1H), 6.67 (d, J = 8.1 Hz, 1H), 6.58 (d, J = 8.2 Hz, 1H), 3.62 (s, 2H). ^{13}C NMR (101 MHz,

Table 4 The pharmacokinetic properties of STY17.

PK parameters	Unit	i.p. (10 mg/kg)	i.v. (10 mg/kg)
$t_{1/2}$	h	1.05	1.29
T_{max}	h	0.194	–
C_0	ng/mL	–	10,833
C_{max}	ng/mL	338	–
AUC_{last}	h·ng/mL	525	880
AUC_{Inf}	h·ng/mL	531	884
$AUC_{\_\%Extrap\_obs}$	%	1.17	0.528
MRT_{Inf_obs}	h	1.34	0.127
AUC_{last}/D	h·kg·ng/mL/mg	52.5	88.0
CL_obs	mL/min/kg	–	195
V_d	L/kg	–	22.0
F	%	60.1	–

DMSO-d_6) δ 171.36, 160.39, 150.20, 145.59, 144.81, 131.26, 130.69, 125.61, 123.94, 123.73, 120.51, 120.39, 117.04, 115.98, 41.77. HRMS (ESI) of compound STY3: calcd for $C_{15}H_{12}ClN_2O_3S$ $[M + H]^+$ = 335.0252, found $[M + H]^+$ = 335.0253.

N-(5-Bromobenzo[d]thiazol-2-yl)-2-(3,4-dihydroxyphenyl) acetamide (STY4). White solid 82.40 mg, yield: 42%. HPLC purity: 95.73%. ^{1}H NMR (400 MHz, DMSO-d_6) δ 12.65 (s, 1H), 8.90 (s, 1H), 8.80 (s, 1H), 7.98−7.92 (m, 2H), 7.45 (dd, J = 8.5, 1.9 Hz, 1H), 6.75 (d, J = 2.2 Hz, 1H), 6.68 (d, J = 8.1 Hz, 1H), 6.59 (dd, J = 8.1, 2.2 Hz, 1H), 3.62 (s, 2H). ^{13}C NMR (101 MHz, DMSO-d_6) δ 176.15, 164.93, 155.30, 150.36, 149.58, 135.91, 131.37, 130.38, 128.82, 128.03, 125.30, 124.09, 121.79, 120.73, 46.54. HRMS (ESI) of compound STY4: calcd for $C_{15}H_{12}BrN_2O_3S$ $[M + H]^+$ = 378.9747, found $[M + H]^+$ = 378.9745.

2-(3,4-Dihydroxyphenyl)-N-(6-fluorobenzo[d]thiazol-2-yl)acetamide (STY5). White solid 76.40 mg, yield: 80%. HPLC purity: 95.41%. ^{1}H NMR (400 MHz, DMSO-d_6) δ 8.87 (s, 2H), 7.88 (dd, J = 8.7, 2.7 Hz, 1H), 7.78−7.70 (m, 1H), 7.34−7.22 (m, 1H), 6.75 (d, J = 2.0 Hz, 1H), 6.70−6.65 (m, 1H), 6.59 (dd, J = 8.1, 2.0 Hz, 1H), 3.61 (s, 2H). ^{13}C NMR (101 MHz, DMSO-d_6) δ 171.24, 159.07 (d, $^1J_{C-F}$ = 239.7 Hz), 158.46 (d, $^4J_{C-F}$ = 2.6 Hz), 145.68, 145.58, 144.79, 133.11 (d, $^3J_{C-F}$ = 11.0 Hz), 125.71, 122.04 (d, $^3J_{C-F}$ = 9.1 Hz), 120.51, 117.03, 115.97, 114.65 (d, $^2J_{C-F}$ = 24.5 Hz), 108.61 (d, $^2J_{C-F}$ = 27.1 Hz), 41.74. HRMS (ESI) of compound STY5: calcd for $C_{15}H_{12}FN_2O_3S$ $[M + H]^+$ = 319.0547, found $[M + H]^+$ = 319.0542.

N-(6-Chlorobenzo[d]thiazol-2-yl)-2-(3,4-dihydroxyphenyl)acetamide (STY6). White solid 32.00 mg, yield: 59%. HPLC purity: 95.06%. ^{1}H NMR (400 MHz, DMSO-d_6) δ 12.58 (s, 1H), 8.90 (s, 1H), 8.80 (s, 1H), 8.11 (d, J = 2.2 Hz, 1H), 7.73 (d, J = 8.7 Hz, 1H), 7.45 (dd, J = 8.6, 2.3 Hz, 1H), 6.75 (d, J = 2.2 Hz, 1H), 6.68 (d, J = 8.1 Hz, 1H), 6.59 (dd, J = 8.1, 2.2 Hz, 1H), 3.62 (s, 2H). ^{13}C NMR (101 MHz, DMSO-d_6) δ 171.34, 159.30, 147.86, 145.59, 144.80, 133.59, 128.01, 126.90, 125.64, 122.15, 121.89, 120.51, 117.01, 115.96, 41.76. HRMS (ESI) of compound STY6: calcd for $C_{15}H_{12}ClN_2O_3S$ $[M + H]^+$ = 335.0252, found $[M + H]^+$ = 335.0252.

N-(6-Bromobenzo[d]thiazol-2-yl)-2-(3,4-dihydroxyphenyl)acetamide (STY7). White solid 60.50 mg, yield: 69%. HPLC purity: 95.20%. 1H NMR (400 MHz, DMSO-d_6) δ 12.59 (s, 1H), 8.88 (s, 1H), 8.80 (s, 1H), 8.23 (s, 1H), 7.72−7.63 (m, 1H), 7.56 (d, J = 9.5 Hz, 1H), 6.74 (s, 1H), 6.70−6.65 (m, 1H), 6.58 (d, J = 8.5 Hz, 1H), 3.61 (s, 2H). ^{13}C NMR (101 MHz, DMSO-d_6) δ 171.36, 159.26, 148.14, 145.58, 144.79, 134.08, 129.59, 125.64, 124.70, 122.55, 120.53, 117.01, 115.97, 115.90, 41.77. HRMS (ESI) of compound STY7: calcd for $C_{15}H_{12}BrN_2O_3S$ $[M + H]^+$ = 378.9747, found $[M + H]^+$ = 378.9744.

2-(3,4-Dihydroxyphenyl)-N-(6-methoxybenzo[d]thiazol-2-yl)acetamide (STY8). White solid 41.30 mg, yield: 42%. HPLC purity: 95.20%. ^{1}H NMR (400 MHz, DMSO-d_6) δ 12.36 (s, 1H), 8.90 (s, 1H), 8.80 (s, 1H), 7.63 (d, J = 8.8 Hz, 1H), 7.55 (d, J = 2.4 Hz, 1H), 7.02 (dd, J = 8.8, 2.5 Hz, 1H), 6.76 (d, J = 1.6 Hz, 1H), 6.68 (d, J = 8.0 Hz, 1H), 6.60 (dd, J = 8.0, 1.6 Hz, 1H), 3.79 (s, 3H), 3.59 (s, 2H). ^{13}C NMR (101 MHz, DMSO-d_6) δ 170.84, 156.56, 156.41, 145.57, 144.75, 143.05, 133.18, 125.88, 121.55, 120.50, 117.00, 115.95, 115.35, 105.15, 56.06, 41.76. HRMS (ESI) of compound STY8: calcd for $C_{16}H_{15}N_2O_4S$ $[M + H]^+$ = 331.0747, found $[M + H]^+$ = 331.0749.

2-(3,4-Dihydroxyphenyl)-N-(6-ethoxybenzo[d]thiazol-2-yl)acetamide (STY9). White solid 30.20 mg, yield: 47%. HPLC purity: 95.45%. ^{1}H NMR (400 MHz, DMSO-d_6) δ 12.35 (s, 1H), 8.90 (s, 1H), 8.80 (s, 1H), 7.62 (d, J = 8.8 Hz, 1H), 7.53 (d, J = 2.6 Hz, 1H), 7.01 (dd, J = 8.9, 2.6 Hz, 1H), 6.75 (d, J = 2.2 Hz, 1H), 6.68 (d, J = 8.0 Hz, 1H), 6.59 (dd, J = 8.0, 2.1 Hz, 1H), 4.05 (q, J = 7.0 Hz, 2H), 3.59 (s, 2H), 1.34 (t, J = 7.0 Hz, 3H). ^{13}C NMR (101 MHz, DMSO-d_6) δ 170.84, 156.38, 155.80, 145.58, 144.76, 142.99, 133.17, 125.89, 121.55, 120.50, 117.01, 115.95, 115.71, 105.80, 64.05, 41.76, 15.16. HRMS (ESI) of compound STY9: calcd for $C_{17}H_{17}N_2O_4S$ $[M + H]^+$ = 345.0904, found $[M + H]^+$ = 345.0901.

2-(3,4-Dihydroxyphenyl)-N-(6-nitrobenzo[d]thiazol-2-yl) acetamide (STY10). Yellow solid 33.20 mg, yield: 91%. HPLC purity: 95.31%. ^{1}H NMR (400 MHz, DMSO-d_6) δ 12.85 (s, 1H), 9.03 (s, 1H), 8.88 (m, 2H), 8.26 (d, J = 9.0 Hz, 1H), 7.88 (d, J = 9.0 Hz, 1H), 6.76 (s, 1H), 6.69 (d, J = 8.0 Hz, 1H), 6.60 (d, J = 8.1 Hz, 1H), 3.67 (s, 2H). ^{13}C NMR (101 MHz, DMSO-d_6) δ 171.87, 164.01, 153.90, 145.62, 144.86, 143.40, 132.62, 125.40, 122.20, 120.99, 120.56, 119.48, 117.06, 115.99, 41.80. HRMS (ESI) of compound STY10: calcd for $C_{15}H_{12}N_3O_5S$ $[M + H]^+$ = 346.0492, found $[M + H]^+$ = 346.0493.

2-(3,4-Dihydroxyphenyl)-N-(6-(trifluoromethyl)benzo[d]thiazol-2-yl)acetamide (STY11). White solid 49.00 mg, yield: 53%. HPLC purity: 95.74%. ^{1}H NMR (400 MHz, DMSO-d_6) δ 12.75 (s, 1H), 8.48 (s, 1H), 7.90 (d, J = 8.5 Hz, 1H), 7.73 (dd, J = 8.6, 1.6 Hz, 1H), 6.77 (d, J = 1.9 Hz, 1H), 6.69 (d, J = 8.0 Hz, 1H), 6.60 (dd, J = 8.1, 1.9 Hz, 1H), 3.65 (s, 2H). ^{13}C NMR (101 MHz, DMSO-d_6) δ 171.61, 161.67, 151.74, 145.60, 144.83, 132.44, 126.38, 125.53, 124.16 (d, $^2J_{C-F}$ = 31.7 Hz), 123.68, 123.35 (d, $^3J_{C-F}$ = 3.6 Hz), 121.35, 120.33 (d, $^3J_{C-F}$ = 4.3 Hz), 117.05, 115.98, 41.79. HRMS (ESI) of compound STY11: calcd for $C_{16}H_{12}F_3N_2O_3S$ $[M + H]^+$ = 369.0515, found $[M + H]^+$ = 369.0516.

4.2.3. *Synthesis of target compounds STY12−STY27*

Intermediate **10a** (97.10 mg, 0.27 mmol) was dissolved in DCM and 1 mol/L BBr_3 (1.63 mL, 1.63 mmol) was slowly added dropwise under an ice bath. After the reaction for 30 min, the reaction was quenched by the addition of ice water. The product STY12 was collected by filtration. The compounds STY13−STY27 were obtained in the same synthetic method as compound STY12 using intermediates **10b−10p** as the reactants.

2-(Benzo[d]thiazol-2-ylamino)-N-(3,4-dihydroxybenzyl)acetamide (STY12). White solid 33.20 mg, yield: 37%. HPLC purity: 95.65%. ^{1}H NMR (400 MHz, DMSO-d_6) δ 8.81 (s, 1H), 8.75 (s, 1H), 8.39 (t, J = 5.7 Hz, 1H), 8.29 (t, J = 5.3 Hz, 1H), 7.68 (d, J = 7.6 Hz, 1H), 7.41 (d, J = 7.9 Hz, 1H), 7.27−7.20 (m, 1H), 7.04 (t, J = 7.5 Hz, 1H), 6.71−6.63 (m, 2H), 6.55 (dd, J = 8.0, 1.7 Hz, 1H), 4.14 (s, 2H), 4.04 (s, 2H). ^{13}C NMR (101 MHz, DMSO-d_6) δ 168.91, 166.69, 152.58, 145.52, 144.60, 131.10, 130.52, 125.96, 121.56, 121.42, 118.71, 118.59, 115.71, 115.46, 47.08, 42.28. HRMS (ESI) of compound STY12: calcd for $C_{16}H_{16}N_3O_3S$ $[M + H]^+$ = 330.0907, found $[M + H]^+$ = 330.0908.

N-(3,4-Dihydroxybenzyl)-2-((6-fluorobenzo[d]thiazol-2-yl)amino)acetamide (STY13). White solid 30.20 mg, yield: 46%. HPLC purity: 95.06%. ^{1}H NMR (400 MHz, DMSO-d_6) δ 8.78 (s, 2H), 8.39 (t, J = 5.9 Hz, 1H), 8.27 (t, J = 5.8 Hz, 1H), 7.61 (dd, J = 8.8, 2.7 Hz, 1H), 7.38 (dd, J = 8.8, 4.8 Hz, 1H), 7.06 (td, J = 9.1, 2.8 Hz, 1H), 6.70−6.62 (m, 2H), 6.54 (dd, J = 8.0, 2.0 Hz, 1H), 4.14 (d, J = 5.8 Hz, 2H), 4.03 (d, J = 5.1 Hz, 2H). ^{13}C NMR (101 MHz, DMSO-d_6) δ 168.84, 166.58, 157.71 (d, $^1J_{C-F}$ = 236.6 Hz), 149.35 (d, $^4J_{C-F}$ = 1.3 Hz), 145.52, 144.60, 132.20

(d, $^{3}J_{C-F}$ = 11.2 Hz), 130.51, 119.03 (d, $^{3}J_{C-F}$ = 9.0 Hz), 118.70, 115.70, 115.45, 113.25 (d, $^{2}J_{C-F}$ = 23.7 Hz), 108.33 (d, $^{2}J_{C-F}$ = 27.1 Hz), 47.07, 42.27. HRMS (ESI) of compound STY13: calcd for $C_{16}H_{15}FN_3O_3S$ $[M + H]^+$ = 348.0813, found $[M + H]^+$ = 348.0814.

N-(3,4-Dihydroxybenzyl)-2-((6-(trifluoromethoxy) benzo[d]thiazol-2-yl)amino)acetamide (STY14). White solid 67.70 mg, yield: 71%. HPLC purity: 95.07%. ^{1}H NMR (400 MHz, DMSO-d_6) δ 8.80 (s, 1H), 8.75 (s, 1H), 8.45 (t, J = 5.7 Hz, 1H), 8.40 (t, J = 5.8 Hz, 1H), 7.84−7.79 (m, 1H), 7.44 (d, J = 8.7 Hz, 1H), 7.23−7.18 (m, 1H), 6.70−6.61 (m, 2H), 6.54 (dd, J = 8.0, 1.6 Hz, 1H), 4.14 (d, J = 5.8 Hz, 2H), 4.06 (d, J = 5.6 Hz, 2H). ^{13}C NMR (101 MHz, DMSO-d_6) δ 168.66, 167.85, 151.82, 145.51, 144.61, 142.72, 132.27, 130.48, 119.44, 118.87, 118.69, 115.70, 115.46, 114.95, 47.05, 42.28. HRMS (ESI) of compound STY14: calcd for $C_{17}H_{15}F_3N_3O_4S$ $[M + H]^+$ = 414.0730, found $[M + H]^+$ = 414.0727.

2-((6-Bromobenzo[d]thiazol-2-yl)amino)-N-(3,4-dihydroxybenzyl)acetamide (STY15). White solid 40.90 mg, yield: 44%. HPLC purity: 96.90%. ^{1}H NMR (400 MHz, DMSO-d_6) δ 8.78 (s, 2H), 8.47−8.35 (m, 2H), 7.93 (s, 1H), 7.40−7.29 (m, 2H), 6.72−6.62 (m, 2H), 6.54 (d, J = 7.9 Hz, 1H), 4.14 (d, J = 5.5 Hz, 2H), 4.05 (d, J = 3.0 Hz, 2H). ^{13}C NMR (101 MHz, DMSO-d_6) δ 168.69, 167.29, 151.92, 145.52, 144.61, 133.38, 130.48, 128.80, 123.83, 119.98, 118.70, 115.71, 115.46, 112.86, 47.05, 42.29. HRMS (ESI) of compound STY15: calcd for $C_{16}H_{15}BrN_3O_3S$ $[M + H]^+$ = 408.0012, found $[M + H]^+$ = 408.0009.

N-(3,4-Dihydroxybenzyl)-2-((6-(trifluoromethyl)benzo [d]thiazol-2-yl)amino)acetamide (STY16). White solid 82.40 mg, yield: 83%. HPLC purity: 95.42%. ^{1}H NMR (400 MHz, DMSO-d_6) δ 8.86 (s, 1H), 8.48 (t, J = 5.7 Hz, 1H), 8.17 (s, 1H), 7.55 (s, 2H), 6.72−6.64 (m, 2H), 6.55 (dd, J = 8.0, 1.7 Hz, 1H), 4.15 (d, J = 5.8 Hz, 2H), 4.12 (s, 2H). ^{13}C NMR (101 MHz, DMSO-d_6) δ 169.35, 168.33, 145.54, 144.65, 131.37 (d, $^{4}J_{C-F}$ = 2.6 Hz), 130.41, 123.22 (q, $^{3}J_{C-F}$ = 5.3, 3.9 Hz), 119.27 (q, $^{4}J_{C-F}$ = 5.8, 2.0 Hz), 118.74, 118.15, 115.74, 115.52, 47.16, 42.34. HRMS (ESI) of compound STY16: calcd for $C_{17}H_{15}F_3N_3O_3S$ $[M + H]^+$ = 398.0781, found $[M + H]^+$ = 398.0784.

N-(3,4-Dihydroxybenzyl)-2-((6-nitrobenzo[d]thiazol-2-yl)amino)acetamide (STY17). Yellow solid 25.70 mg, yield: 92%. HPLC purity: 95.22%. ^{1}H NMR (400 MHz, DMSO-d_6) δ 9.00 (s, 1H), 8.79 (s, 2H), 8.73 (d, J = 2.5 Hz, 1H), 8.47 (t, J = 5.9 Hz, 1H), 8.12 (dd, J = 8.9, 2.5 Hz, 1H), 7.49 (d, J = 8.9 Hz, 1H), 6.70−6.62 (m, 2H), 6.54 (dd, J = 8.0, 2.2 Hz, 1H), 4.15 (s, 2H), 4.14 (s, 2H). ^{13}C NMR (101 MHz, DMSO-d_6) δ 171.48, 168.19, 158.12, 145.54, 144.65, 141.37, 131.89, 130.39, 122.46, 118.73, 118.29, 117.76, 115.72, 115.49, 47.16, 42.34. HRMS (ESI) of compound STY17: calcd for $C_{16}H_{15}N_4O_5S$ $[M + H]^+$ = 375.0758, found $[M + H]^+$ = 375.0762.

N-(3,4-Dihydroxybenzyl)-2-((5-fluorobenzo[d]thiazol-2-yl)amino)acetamide (STY18). White solid 87.00 mg, yield: 93%. HPLC purity: 95.15%. ^{1}H NMR (400 MHz, DMSO-d_6) δ 8.86 (s, 1H), 8.83 (s, 1H), 8.49 (t, J = 5.6 Hz, 1H), 8.45 (t, J = 6.1 Hz, 1H), 7.68 (dd, J = 8.6, 5.5 Hz, 1H), 7.20 (dd, J = 10.5, 2.5 Hz, 1H), 6.87 (td, J = 9.0, 2.6 Hz, 1H), 6.72−6.63 (m, 2H), 6.53 (d, J = 8.0 Hz, 1H), 4.13 (d, J = 5.8 Hz, 2H), 4.04 (d, J = 5.6 Hz, 2H). ^{13}C NMR (101 MHz, DMSO-d_6) δ 168.89, 168.73, 161.69 (d, $^{1}J_{C-F}$ = 237.3 Hz), 153.91 (d, $^{3}J_{C-F}$ = 12.1 Hz), 145.49, 144.58, 130.46, 126.67 (d, $^{4}J_{C-F}$ = 1.2 Hz), 122.23 (d, $^{3}J_{C-F}$ = 9.6 Hz), 118.67, 115.78, 115.53, 108.71 (d, $^{2}J_{C-F}$ = 24.3 Hz), 105.17 (d, $^{2}J_{C-F}$ = 24.3 Hz), 47.04, 42.25. HRMS (ESI) of compound STY18: calcd for $C_{16}H_{15}FN_3O_3S$ $[M + H]^+$ = 348.0813, found $[M + H]^+$ = 348.0814.

2-((5-Chlorobenzo[d]thiazol-2-yl)amino)-N-(3,4-dihydroxybenzyl)acetamide (STY19). White solid 32.00 mg, yield: 40%. HPLC purity: 95.77%. ^{1}H NMR (400 MHz, DMSO-d_6) δ 8.78 (s, 2H), 8.49 (s, 1H), 8.41 (t, J = 5.4 Hz, 1H), 7.70 (d, J = 8.3 Hz, 1H), 7.44−7.39 (m, 1H), 7.06 (dd, J = 8.3, 1.4 Hz, 1H), 6.70−6.63 (m, 2H), 6.54 (d, J = 7.5 Hz, 1H), 4.14 (d, J = 5.6 Hz, 2H), 4.06 (d, J = 4.1 Hz, 2H). ^{13}C NMR (101 MHz, DMSO-d_6) δ 168.62, 168.35, 153.95, 145.53, 144.62, 130.65, 130.47, 129.96, 122.66, 121.21, 118.71, 118.01, 115.71, 115.47, 47.05, 42.30. HRMS (ESI) of compound STY19: calcd for $C_{16}H_{15}ClN_3O_3S$ $[M + H]^+$ = 364.0517, found $[M + H]^+$ = 364.0517.

2-((5-Bromobenzo[d]thiazol-2-yl)amino)-N-(3,4-dihydroxybenzyl)acetamide (STY20). White solid 20.00 mg, yield: 21%. HPLC purity: 95.72%. ^{1}H NMR (400 MHz, DMSO-d_6) δ 8.83 (s, 1H), 8.79 (s, 1H), 8.46 (d, J = 5.7 Hz, 1H), 8.43 (d, J = 6.1 Hz, 1H), 7.92 (s, 1H), 7.38−7.27 (m, 2H), 6.70−6.63 (m, 2H), 6.52 (d, J = 8.0 Hz, 1H), 4.12 (d, J = 5.8 Hz, 2H), 4.03 (d, J = 5.5 Hz, 2H). ^{13}C NMR (101 MHz, DMSO-d_6) δ 168.73, 167.29, 151.90, 145.48, 144.57, 133.38, 130.46, 128.79, 123.83, 119.98, 118.67, 115.75, 115.49, 112.82, 47.04, 42.25. HRMS (ESI) of compound STY20: calcd for $C_{16}H_{15}BrN_3O_3S$ $[M + H]^+$ = 408.0012, found $[M + H]^+$ = 408.0011.

N-(3,4-Dihydroxybenzyl)-2-((5-nitrobenzo[d]thiazol-2-yl)amino)acetamide (STY21). Yellow solid 76.40 mg, yield: 82%. HPLC purity: 95.20%. ^{1}H NMR (400 MHz, DMSO-d_6) δ 8.85 (s, 1H), 8.48 (t, J = 5.8 Hz, 1H), 8.10 (d, J = 2.2 Hz, 1H), 7.98 (d, J = 8.6 Hz, 1H), 7.91 (dd, J = 8.6, 2.2 Hz, 1H), 6.69−6.62 (m, 2H), 6.54 (dd, J = 8.0, 1.9 Hz, 1H), 4.14 (d, J = 5.8 Hz, 2H), 4.11 (s, 2H). ^{13}C NMR (101 MHz, DMSO-d_6) δ 169.06, 168.26, 152.37, 146.56, 145.53, 144.64, 139.08, 130.40, 122.26, 118.70, 116.31, 115.72, 115.49, 112.17, 47.12, 42.33. HRMS (ESI) of compound STY21: calcd for $C_{16}H_{15}N_4O_5S$ $[M + H]^+$ = 375.0758, found $[M + H]^+$ = 375.0757.

N-(3,4-Dihydroxybenzyl)-2-((5-nitrobenzo[d]oxazol-2-yl)amino)acetamide (STY22). Yellow solid 40.00 mg, yield: 86%. HPLC purity: 95.27%. ^{1}H NMR (400 MHz, DMSO-d_6) δ 8.75 (t, J = 5.9 Hz, 1H), 8.47 (t, J = 5.4 Hz, 1H), 8.09−8.04 (m, 1H), 7.98 (dd, J = 8.7, 2.0 Hz, 1H), 7.61 (d, J = 8.7 Hz, 1H), 6.73−6.63 (m, 2H), 6.54 (d, J = 7.9 Hz, 1H), 4.14 (d, J = 5.5 Hz, 2H), 3.99 (d, J = 6.0 Hz, 2H). ^{13}C NMR (101 MHz, DMSO-d_6) δ 168.33, 164.93, 152.99, 145.53, 144.90, 144.64, 144.50, 130.44, 118.77, 117.44, 115.68, 115.55, 110.88, 109.34, 45.60, 42.35. HRMS (ESI) of compound STY22: calcd for $C_{16}H_{15}N_4O_6$ $[M + H]^+$ = 359.0986, found $[M + H]^+$ = 359.0983.

2-((5-Chlorobenzo[d]oxazol-2-yl)amino)-N-(3,4-dihydroxybenzyl)acetamide (STY23). White solid 63.80 mg, yield: 38%. HPLC purity: 95.08%. ^{1}H NMR (400 MHz, DMSO-d_6) δ 8.55 (s, 1H), 8.44 (t, J = 5.8 Hz, 1H), 7.58 (d, J = 1.9 Hz, 1H), 7.27 (d, J = 8.3 Hz, 1H), 7.19 (dd, J = 8.3, 1.9 Hz, 1H), 6.67 (d, J = 1.8 Hz, 1H), 6.65 (d, J = 8.0 Hz, 1H), 6.53 (dd, J = 8.0, 1.7 Hz, 1H), 4.12 (d, J = 5.8 Hz, 2H), 3.95 (s, 2H). ^{13}C NMR (101 MHz, DMSO-d_6) δ 168.35, 163.04, 148.60, 145.50, 144.63, 141.06, 130.41, 125.02, 124.49, 118.79, 116.36, 115.69, 115.55, 110.08, 45.61, 42.34. HRMS (ESI) of compound STY23: calcd for $C_{16}H_{15}ClN_3O_4$ $[M + H]^+$ = 348.0746, found $[M + H]^+$ = 348.0747.

2-(Benzo[d]oxazol-2-ylamino)-N-(3,4-dihydroxybenzyl)acetamide (STY24). White solid 49.50 mg, yield: 75%. HPLC purity: 95.11%. ^{1}H NMR (400 MHz, DMSO-d_6) δ 8.77 (s, 2H), 8.40 (t, J = 5.8 Hz, 1H), 8.21 (t, J = 6.0 Hz, 1H),

7.37 (d, J = 7.9 Hz, 1H), 7.26 (d, J = 7.7 Hz, 1H), 7.16−7.09 (m, 1H), 7.00 (td, J = 7.8, 1.1 Hz, 1H), 6.68−6.62 (m, 2H), 6.53 (dd, J = 8.0, 1.9 Hz, 1H), 4.12 (d, J = 5.8 Hz, 2H), 3.94 (d, J = 6.1 Hz, 2H). ^{13}C NMR (101 MHz, DMSO-d_6) δ 168.81, 162.85, 148.59, 145.52, 144.62, 143.12, 130.53, 124.16, 120.87, 118.77, 115.99, 115.68, 115.54, 109.16, 45.67, 42.32. HRMS (ESI) of compound STY24: calcd for $C_{16}H_{16}N_3O_4$ $[M + H]^+$ = 314.1135, found $[M + H]^+$ = 314.1131.

2-((5-Bromobenzo[d]oxazol-2-yl)amino)-N-(3,4-dihydroxybenzyl)acetamide (STY25). White solid 82.80 mg, yield: 88%. HPLC purity: 96.01%. ^{1}H NMR (400 MHz, DMSO-d_6) δ 8.50 (t, J = 5.5 Hz, 1H), 8.43 (t, J = 5.8 Hz, 1H), 7.44 (d, J = 1.9 Hz, 1H), 7.36 (d, J = 8.4 Hz, 1H), 7.16 (dd, J = 8.4, 1.9 Hz, 1H), 6.67 (d, J = 1.8 Hz, 1H), 6.64 (d, J = 8.0 Hz, 1H), 6.52 (dd, J = 8.0, 1.8 Hz, 1H), 4.12 (d, J = 5.8 Hz, 2H), 3.94 (d, J = 5.1 Hz, 2H). ^{13}C NMR (101 MHz, DMSO-d_6) δ 168.29, 163.33, 147.49, 145.50, 144.64, 143.90, 130.40, 123.67, 118.78, 118.21, 116.35, 115.69, 115.55, 111.06, 45.55, 42.35. HRMS of STY25: calcd for $C_{16}H_{15}BrN_3O_4$ $[M + H]^+$ = 392.0240, found $[M + H]^+$ = 392.0240.

N-(3,4-Dihydroxybenzyl)-2-((6-fluorobenzo[d]oxazol-2-yl)amino)acetamide (STY26). White solid 52.20 mg, yield: 58%. HPLC purity: 95.21%. ^{1}H NMR (400 MHz, DMSO-d_6) δ 8.79 (s, 1H), 8.76 (s, 1H), 8.40 (t, J = 5.8 Hz, 1H), 8.22 (t, J = 6.2 Hz, 1H), 7.38 (dd, J = 8.5, 2.5 Hz, 1H), 7.23 (dd, J = 8.6, 5.0 Hz, 1H), 6.98 (ddd, J = 10.9, 8.6, 2.5 Hz, 1H), 6.70−6.61 (m, 2H), 6.53 (dd, J = 8.0, 1.9 Hz, 1H), 4.12 (d, J = 5.8 Hz, 2H), 3.92 (d, J = 6.1 Hz, 2H). ^{13}C NMR (101 MHz, DMSO-d_6) δ 168.79, 163.46, 157.47 (d, $^1J_{C-F}$ = 235.1 Hz), 148.43 (d, $^3J_{C-F}$ = 15.0 Hz), 145.50, 144.61, 139.87, 130.53, 118.76, 115.80 (d, $^3J_{C-F}$ = 10.0 Hz), 115.67, 115.53, 110.65 (d, $^2J_{C-F}$ = 23.5 Hz), 98.12 (d, $^2J_{C-F}$ = 29.3 Hz), 45.69, 42.31. HRMS of STY26: calcd for $C_{16}H_{15}FN_3O_4$ $[M + H]^+$ = 332.1041, found $[M + H]^+$ = 332.1043.

2-((6-Chlorobenzo[d]oxazol-2-yl)amino)-N-(3,4-dihydroxybenzyl)acetamide (STY27). White solid 83.10 mg, yield: 89%. HPLC purity: 95.61%. ^{1}H NMR (400 MHz, DMSO-d_6) δ 8.79 (s, 1H), 8.74 (s, 1H), 8.41 (t, J = 5.9 Hz, 1H), 8.35 (t, J = 6.3 Hz, 1H), 7.54 (d, J = 2.0 Hz, 1H), 7.24 (d, J = 8.3 Hz, 1H), 7.16 (dd, J = 8.3, 2.0 Hz, 1H), 6.67 (d, J = 2.1 Hz, 1H), 6.64 (d, J = 8.0 Hz, 1H), 6.52 (dd, J = 8.0, 2.1 Hz, 1H), 4.12 (d, J = 5.9 Hz, 2H), 3.93 (d, J = 6.3 Hz, 2H). ^{13}C NMR (101 MHz, DMSO-d_6) δ 168.65, 163.50, 148.99, 145.51, 144.62, 142.67, 130.49, 124.53, 124.17, 118.77, 116.68, 115.67, 115.53, 109.79, 45.65, 42.32. HRMS (ESI) of compound STY27: calcd for $C_{16}H_{15}ClN_3O_4$ $[M + H]^+$ = 348.0746, found $[M + H]^+$ = 348.0739.

4.2.4. Synthesis of target compounds STY28−STY33

The commercially available compound 2-chloro-6-nitrobenzo[*d*]thiazole (50.00 mg, 0.23 mmol) was dissolved with compound **13a** (78.40 mg, 0.35 mmol) in 5 mL ethanol, and the reaction was carried out by adding DIPEA (0.23 mL, 1.33 mmol) at 80 °C for 12 h. At the end of the reaction, a yellow solid was precipitated and compound STY28 was by filtration. The compounds STY29−STY33 were obtained in the same synthetic method as compounds STY28 using intermediates **13b−13f** as the reactants.

N-(3,4-Dimethoxybenzyl)-2-((6-nitrobenzo[d]thiazol-2-yl)amino)acetamide (STY28). Yellow solid 89.50 mg, yield: 97%. HPLC purity: 96.85%. ^{1}H NMR (400 MHz, DMSO-d_6) δ 9.02 (s, 1H), 8.73 (d, J = 2.3 Hz, 1H), 8.56 (t, J = 5.7 Hz, 1H), 8.13 (dd, J = 8.9, 2.4 Hz, 1H), 7.48 (d, J = 8.9 Hz, 1H), 6.92−6.86 (m, 2H), 6.82 (d, J = 8.2 Hz, 1H), 4.27 (d, J = 5.8 Hz, 2H), 4.17 (s, 2H), 3.73 (s, 3H), 3.71 (s, 3H). ^{13}C NMR (101 MHz, DMSO-d_6) δ 171.56, 168.44, 158.29, 149.08, 148.25, 141.36, 132.06, 131.96, 122.46, 119.82, 118.27, 117.76, 112.17, 111.80, 56.04, 55.86, 47.18, 42.39. HRMS (ESI) of compound STY28: calcd for $C_{18}H_{19}N_4O_5S$ $[M + H]^+$ = 403.1071, found $[M + H]^+$ = 403.1064.

N-(Cyclohexylmethyl)-2-((6-nitrobenzo[d]thiazol-2-yl)amino)acetamide (STY29). Yellow solid 120.20 mg, yield: 69%. HPLC purity: 97.41%. ^{1}H NMR (400 MHz, DMSO-d_6) δ 9.09 (t, J = 5.6 Hz, 1H), 8.72 (d, J = 2.5 Hz, 1H), 8.18−8.06 (m, 2H), 7.45 (d, J = 8.9 Hz, 1H), 4.09 (d, J = 5.2 Hz, 2H), 2.94 (t, J = 6.3 Hz, 2H), 1.71−1.62 (m, 4H), 1.62−1.55 (m, 1H), 1.39 (m, 1H), 1.19−1.06 (m, 3H), 0.91−0.79 (m, 2H). ^{13}C NMR (101 MHz, DMSO-d_6) δ 171.44, 168.29, 158.31, 141.29, 131.94, 122.43, 118.25, 117.66, 47.15, 45.29, 37.93, 30.77 (2C), 26.48, 25.87 (2C). HRMS (ESI) of compound STY29: calcd for $C_{16}H_{21}N_4O_3S$ $[M + H]^+$ = 349.1329, found $[M + H]^+$ = 349.1320.

N-Benzyl-2-((6-nitrobenzo[d]thiazol-2-yl)amino)acetamide (STY30). Yellow solid 228.60 mg, yield: 95%. HPLC purity: 97.36%. ^{1}H NMR (400 MHz, DMSO-d_6) δ 9.06 (t, J = 5.7 Hz, 1H), 8.73 (d, J = 2.4 Hz, 1H), 8.65 (t, J = 5.9 Hz, 1H), 8.14 (dd, J = 8.9, 2.5 Hz, 1H), 7.50 (d, J = 8.9 Hz, 1H), 7.30 (m, J = 3.2 Hz, 4H), 7.26−7.20 (m, 1H), 4.34 (d, J = 6.0 Hz, 2H), 4.18 (d, J = 5.6 Hz, 2H). ^{13}C NMR (101 MHz, DMSO-d_6) δ 171.51, 168.65, 158.29, 141.38, 139.69, 132.00, 128.69 (2C), 127.57 (2C), 127.20, 122.48, 118.29, 117.78, 47.21, 42.54. HRMS (ESI) of compound STY30: calcd for $C_{16}H_{15}N_4O_3S$ $[M + H]^+$ = 343.0859, found $[M + H]^+$ = 343.0852.

N-(2-Chlorophenethyl)-2-((6-nitrobenzo[d]thiazol-2-yl)amino)acetamide (STY31). Yellow solid 49.70 mg, yield: 55%. HPLC purity: 95.65%. ^{1}H NMR (400 MHz, DMSO-d_6) δ 8.98 (t, J = 5.7 Hz, 1H), 8.72 (s, 1H), 8.25 (t, J = 5.7 Hz, 1H), 8.11 (dd, J = 9.0, 2.5 Hz, 1H), 7.47 (d, J = 8.9 Hz, 1H), 7.44−7.36 (m, 1H), 7.35−7.28 (m, 1H), 7.26−7.20 (m, 2H), 4.08 (d, J = 5.7 Hz, 2H), 3.39−3.32 (m, 2H), 2.87 (t, J = 7.2 Hz, 2H). ^{13}C NMR (101 MHz, DMSO-d_6) δ 171.43, 168.42, 158.27, 141.33, 137.11, 133.55, 131.96, 131.55, 129.65, 128.62, 127.65, 122.44, 118.26, 117.77, 47.11, 38.91, 33.25. HRMS (ESI) of compound STY31: calcd for $C_{17}H_{16}ClN_4O_3S$ $[M + H]^+$ = 391.0626, found $[M + H]^+$ = 391.0620.

N-(2-Methoxyphenethyl)-2-((6-nitrobenzo[d]thiazol-2-yl)amino)acetamide (STY32). Yellow solid 56.70 mg, yield: 64%. HPLC purity: 97.62%. ^{1}H NMR (400 MHz, DMSO-d_6) δ 8.97 (t, J = 5.6 Hz, 1H), 8.72 (d, J = 2.5 Hz, 1H), 8.16 (t, J = 5.6 Hz, 1H), 8.12 (dd, J = 8.9, 2.5 Hz, 1H), 7.47 (d, J = 8.9 Hz, 1H), 7.18 (td, J = 7.8, 1.8 Hz, 1H), 7.11 (dd, J = 7.4, 1.8 Hz, 1H), 6.94 (d, J = 8.2 Hz, 1H), 6.83 (t, J = 7.3 Hz, 1H), 4.08 (d, J = 5.6 Hz, 2H), 3.78 (s, 3H), 3.33−3.25 (m, 2H), 2.72 (t, J = 7.3 Hz, 2H). ^{13}C NMR (101 MHz, DMSO-d_6) δ 171.40, 168.25, 158.30, 157.64, 141.33, 131.96, 130.46, 128.05, 127.46, 122.45, 120.69, 118.26, 117.76, 111.09, 55.71, 47.13, 39.29, 30.23. HRMS (ESI) of compound STY32: calcd for $C_{18}H_{19}N_4O_4S$ $[M + H]^+$ = 387.1122, found $[M + H]^+$ = 387.1114.

N-(2-Bromophenethyl)-2-((6-nitrobenzo[d]thiazol-2-yl)amino)acetamide (STY33). Yellow solid 74.20 mg, yield: 74%. HPLC purity: 97.27%. ^{1}H NMR (400 MHz, DMSO-d_6) δ 8.98 (t, J

= 5.6 Hz, 1H), 8.72 (d, *J* = 2.4 Hz, 1H), 8.25 (t, *J* = 5.4 Hz, 1H), 8.12 (dd, *J* = 8.9, 2.4 Hz, 1H), 7.57 (d, *J* = 7.9 Hz, 1H), 7.47 (d, *J* = 8.9 Hz, 1H), 7.35−7.24 (m, 2H), 7.15 (td, *J* = 7.9, 1.8 Hz, 1H), 4.08 (d, *J* = 5.5 Hz, 2H), 3.37 (d, *J* = 6.9 Hz, 1H), 3.33 (s, 1H), 2.87 (t, *J* = 7.1 Hz, 2H). ^{13}C NMR (101 MHz, DMSO-d_6) δ 171.47, 168.44, 158.28, 141.34, 138.80, 132.94, 131.96, 131.54, 128.89, 128.24, 124.34, 122.45, 118.26, 117.77, 47.12, 39.02, 35.71. HRMS (ESI) of compound STY33: calcd for $C_{17}H_{16}BrN_4O_3S$ $[M + H]^+$ = 435.0121, found $[M + H]^+$ = 435.0114.

4.2.5. Synthesis of target compounds STY34−STY41

Intermediate **18a** (236.09 mg, 0.69 mmol) was dissolved in DCM and 1 mol/L BBr_3 (4.14 mL, 4.14 mmol) was slowly added dropwise under an ice bath. After the reaction for 30 min, the reaction was quenched by the addition of ice water. The product **S**TY34 was collected by filtration. The compounds STY35−STY41 were obtained in the same synthetic method as compound STY34 using intermediates **18b−18h** as the reactants.

N^1-(3,4-Dihydroxybenzyl)-N^4-phenylsuccinamide (STY34). White solid of 180.00 mg, yield: 58%. HPLC purity: 95.68%. ^{1}H NMR (400 MHz, DMSO-d_6) δ 9.95 (s, 1H), 8.25 (s, 1H), 7.59 (dd, *J* = 8.2, 2.9 Hz, 2H), 7.28 (td, *J* = 7.8, 2.9 Hz, 3H), 7.01 (td, *J* = 7.4, 2.8 Hz, 2H), 6.64 (m, 2H), 6.50 (m, 1H), 4.08 (m, 2H), 2.57 (m, 2H), 2.45 (m, 2H). ^{13}C NMR (101 MHz, DMSO-d_6) δ 171.41, 170.93, 145.51, 144.53, 139.80, 130.79, 129.09 (2C), 123.33, 119.38 (2C), 118.65, 115.72, 115.41, 42.26, 32.23, 30.80. HRMS (ESI) of compound STY34: calcd for $C_{17}H_{19}N_2O_4$ $[M + H]^+$ = 315.1339, found $[M + H]^+$ = 315.1332.

N^1-benzyl-N^4-(3,4-Dihydroxybenzyl)succinimide (STY35). White solid 220.00 mg, yield 66%. HPLC purity: 96.00%. ^{1}H NMR (400 MHz, DMSO-d_6) δ 8.81 (s, 1H), 8.72 (s, 1H), 8.34 (t, *J* = 5.9 Hz, 1H), 8.19 (t, *J* = 5.8 Hz, 1H), 7.31 (m, 2H), 7.24 (m, 3H), 6.70−6.57 (m, 2H), 6.49 (d, *J* = 8.0 Hz, 1H), 4.26 (d, *J* = 5.9 Hz, 2H), 4.07 (d, *J* = 5.8 Hz, 2H), 2.39 (s, 4H). ^{13}C NMR (101 MHz, DMSO-d_6) δ 171.87, 171.52, 145.51, 144.54, 140.06, 130.82, 128.69 (2C), 127.61 (2C), 127.13, 118.66, 115.73, 115.40, 42.50, 42.25, 31.30, 31.29. HRMS (ESI) of compound STY35: calcd for $C_{18}H_{21}N_2O_4$ $[M + H]^+$ = 329.1496, found $[M + H]^+$ = 329.1491.

N^1-(3,4-Dihydroxybenzyl)-N^4-phenethylsuccinamide (STY36). White solid 210.00 mg, yield 60%. HPLC purity: 95.25%. ^{1}H NMR (400 MHz, DMSO-d_6) δ 8.82 (s, 1H), 8.72 (s, 1H), 8.18 (t, *J* = 5.9 Hz, 1H), 7.93 (t, *J* = 5.6 Hz, 1H), 7.33−7.24 (m, 2H), 7.25−7.15 (m, 3H), 6.65 (m, 2H), 6.49 (dd, *J* = 8.0, 2.1 Hz, 1H), 4.07 (d, *J* = 5.8 Hz, 2H), 3.25 (m, 2H), 2.71 (m, 2H), 2.40−2.27 (m, 4H). ^{13}C NMR (101 MHz, DMSO-d_6 δ 171.70, 171.51, 145.51, 144.53, 139.98, 130.83, 129.08 (2C), 128.75 (2C), 126.50, 118.63, 115.70, 115.38, 42.22, 40.71, 35.66, 31.37, 31.31. HRMS (ESI) of compound STY36: calcd for $C_{19}H_{23}N_2O_4$ $[M + H]^+$ = 343.1652, found $[M + H]^+$ = 343.1642.

N^1-([1,1′-Biphenyl]-4-ylmethyl)-N^4-(3,4-dihydroxybenzyl)succinimide (STY37). White solid 290.00 mg, yield 70%. HPLC purity: 95.28%. ^{1}H NMR (400 MHz, DMSO-d_6) δ 8.81 (s, 1H), 8.72 (s, 1H), 8.39 (t, *J* = 6.0 Hz, 1H), 8.20 (t, *J* = 5.8 Hz, 1H), 7.67−7.57 (m, 4H), 7.46 (t, *J* = 7.5 Hz, 2H), 7.35 (m, 3H), 6.65 (m, 2H), 6.50 (dd, *J* = 8.1, 2.0 Hz, 1H), 4.30 (d, *J* = 5.8 Hz, 2H), 4.08 (d, *J* = 5.8 Hz, 2H), 2.43−2.39 (m, 4H). ^{13}C NMR (101 MHz, DMSO-d_6) δ 171.88, 171.50, 145.52, 144.55, 140.45, 139.36, 139.10, 130.83, 129.38 (2C), 128.26 (2C), 127.76, 127.03 (4C), 118.66, 115.72, 115.41, 42.25 (2C), 31.33, 31.28. HRMS (ESI) of compound STY37: calcd for $C_{24}H_{25}N_2O_4$ $[M + H]^+$ = 405.1809, found $[M + H]^+$ = 405.1806.

N^1-(((1r,3r,5r,7r)-Adamantan-2-yl)methyl)-N^4-(3,4-dihydroxybenzyl)succinimide (STY38). White solid 190.00 mg, yield 48%. HPLC purity: 96.26%. ^{1}H NMR (400 MHz, DMSO-d_6) δ 8.80 (s, 1H), 8.73 (s, 1H), 8.17 (t, *J* = 5.8 Hz, 1H), 7.65 (t, *J* = 6.2 Hz, 1H), 6.67−6.60 (m, 2H), 6.48 (dd, *J* = 8.0, 2.1 Hz, 1H), 4.07 (d, *J* = 5.8 Hz, 2H), 2.75 (d, *J* = 6.2 Hz, 2H), 2.36 (m, 4H), 1.96−1.86 (m, 3H), 1.70−1.62 (m, 3H), 1.62−1.52 (m, 3H), 1.48−1.37 (m, 6H). ^{13}C NMR (101 MHz, DMSO-d_6) δ 171.98, 171.59, 145.50, 144.53, 130.79, 118.61, 115.70, 115.38, 50.57, 42.23, 40.24, 37.02 (4C), 34.05, 31.65, 31.49, 28.18 (4C). HRMS (ESI) of compound STY38: calcd for $C_{22}H_{31}N_2O_4$ $[M + H]^+$ = 387.2278, found $[M + H]^+$ = 387.2272.

N^1-(3,4-Dihydroxybenzyl)-N^4-pentylsuccinamide (STY39). White solid 190.00 mg, yield 62%. HPLC purity: 95.19%. ^{1}H NMR (400 MHz, DMSO-d_6) δ 8.79 (s, 1H), 8.71 (s, 1H), 8.16 (t, *J* = 5.8 Hz, 1H), 7.77 (t, *J* = 5.6 Hz, 1H), 6.69−6.55 (m, 2H), 6.47 (dd, *J* = 8.0, 2.1 Hz, 1H), 4.05 (d, *J* = 5.8 Hz, 2H), 3.00 (q, *J* = 6.5 Hz, 2H), 2.38−2.24 (m, 4H), 1.37 (m, 2H), 1.30−1.19 (m, 4H), 0.86 (m, 3H). ^{13}C NMR (101 MHz, DMSO-d_6) δ 171.54 (2C), 145.50, 144.52, 130.81, 118.61, 115.70, 115.37, 42.20, 38.91, 31.39 (2C), 29.28, 29.07, 22.31, 14.39. HRMS (ESI) of compound STY39: calcd for $C_{16}H_{25}N_2O_4$ $[M + H]^+$ = 309.1809, found $[M + H]^+$ = 309.1806.

N^1-(3,4-Dihydroxybenzyl)-N^4-hexylsuccinamide (STY40). White solid 160.00 mg, yield 54%. HPLC purity: 95.02%. ^{1}H NMR (400 MHz, DMSO-d_6) δ 8.80 (s, 1H), 8.71 (s, 1H), 8.16 (t, *J* = 5.9 Hz, 1H), 7.77 (t, *J* = 5.6 Hz, 1H), 6.68−6.58 (m, 2H), 6.48 (dd, *J* = 8.0, 2.1 Hz, 1H), 4.06 (d, *J* = 5.8 Hz, 2H), 3.01 (q, *J* = 6.5 Hz, 2H), 2.37−2.26 (m, 4H), 1.36 (m, 2H), 1.31−1.20 (m, 6H), 0.86 (m, 3H). ^{13}C NMR (101 MHz, DMSO-d_6) δ 171.54 (2C), 145.50, 144.53, 130.81, 118.61, 115.70, 115.37, 42.20, 38.95, 31.47, 31.39 (2C), 29.56, 26.54, 22.53, 14.39. HRMS (ESI) of compound STY40: calcd for $C_{17}H_{27}N_2O_4$ $[M + H]^+$ = 323.1965, found $[M + H]^+$ = 323.1958.

N^1-(3,4-Dihydroxybenzyl)-N^4-heptylsuccinamide (STY41). White solid 240.00 mg, yield 71%. HPLC purity: 95.32%. ^{1}H NMR (400 MHz, DMSO-d_6) δ 8.80 (s, 1H), 8.71 (s, 1H), 8.16 (t, *J* = 5.9 Hz, 1H), 7.77 (t, *J* = 5.6 Hz, 1H), 6.69−6.60 (m, 2H), 6.48 (dd, *J* = 8.0, 2.1 Hz, 1H), 4.06 (d, *J* = 5.8 Hz, 2H), 3.01 (q, *J* = 6.5 Hz, 2H), 2.39−2.24 (m, 4H), 1.37 (m, 2H), 1.32−1.16 (m, 8H), 0.86 (m, 3H). ^{13}C NMR (101 MHz, DMSO-d_6) δ 171.54 (2C), 145.50, 144.52, 130.81, 118.60, 115.69, 115.36, 42.21, 38.95, 31.72, 31.39 (2C), 29.60, 28.90, 26.84, 22.53, 14.42. HRMS (ESI) of compound STY41: calcd for $C_{18}H_{29}N_2O_4$ $[M + H]^+$ = 337.2122, found $[M + H]^+$ = 337.2117.

4.3. Biology

4.3.1. Bacterial strains and growth conditions

The bacteria used in this study mainly included *Pseudomonas aeruginosa* PAO1 (ATCC15692), PA14 wild-type strains, and sdhB-deficient mutant strain. Four clinical strains: PA1129 was from the clinical laboratory of the First Affiliated Hospital of Jinan University. PA182, PA185, PA187, PA1065, and PA1167 were from Guangzhou Red Cross Hospital. Bacteria were stored in LB broth supplemented with 25% glycerol at −80 °C. Before each experiment, frozen primary seeds were inoculated onto LB agar plates and incubated overnight at 37 °C to obtain single colonies. Single colonies were selected and inoculated into LB broth.

Incubate at 37 °C, 200 rpm overnight, and dilute to the desired concentration according to the optical density value at 600 nm.

4.3.2. Biofilm inhibitory activity assay

The biofilm inhibitory activity of the compounds was evaluated by crystal violet staining. Overnight incubated *P. aeruginosa* PAO1, PA182, PA1129, PA185, PA187, PA1065, PA1167 and different concentrations of compounds were added into 96-well flat-bottomed polystyrene microtitre plates and incubated at 37 °C for 24 h. The floating cells were removed and the biofilm was rinsed with PBS, the biofilm was stained with 150 μL of 0.1% crystalline violet for 15 min, then rinsed with distilled water, and finally the crystalline violet was dissolved with 150 μL of 30% glacial acetic acid in each well, and then the optical density (OD) of each well was measured at 570 nm using a microplate reader (Bio Tek, USA) and the experiment was repeated three times.

4.3.3. Growth curve testing

Overnight cultured *P. aeruginosa* PAO1, PA182, PA1129, PA185, PA187, PA1065, and PA1167 were diluted in 100 mL LB broth to give an OD of 0.05 at 600 nm, and then compounds were added for co-culture. Growth curves were recorded every 10 min for 16 h using a Tecan Infinite 200 Pro plate reader (Tecan Group Ltd., Mannedorf, Switzerland).

4.3.4. MIC testing

P. aeruginosa PAO1 was cultured overnight in MH broth and diluted to OD_{600} of 0.05 in 96-well plates. Then, 100 μL of medium containing different concentrations of STY17 was added to the culture plates. After incubation at 37 °C for 20 h, the absorbance value of each well was measured at 600 nm using a microplate reader (Bio Tek, USA). The values of OD_{600} lower than 0.1 were judged as non-growing bacteria. The experiments were analyzed in triplicate.

4.3.5. Elastase activity assay

Single colonies of PAO1 and PAO1-*ΔlasIΔrhlI* were picked in advance in an appropriate amount of LB broth and incubated overnight in a shaker. The bacterial solution was diluted to an OD_{600} of 0.01, and compound STY17 at concentrations of 0, 0.125, 0.25, 0.5, 1, and 2 μmol/L was added, and incubated at 37 °C, 200 rpm for 24 h. The supernatant was collected by centrifugation of the cultures (10,000 rpm, 10 min, 4 °C) and filtered through a sterile 0.2 μmol/L filter tip for spare parts. Elastase activity was next determined using the EnzChekTM Protease assay kit (Invitrogen, USA). The reagents and samples were added to 96-well black plates according to the manufacturer's instructions, and the fluorescence values were measured using a microplate reader (excitation wavelength 490 nm, emission wavelength 520 nm) at 10-min intervals for at least 7 h. The experiments were analyzed in triplicate.

4.3.6. Pyocyanin production inhibition assay

The overnight culture was diluted to an OD_{600} of 0.01, supplemented with compound STY17 to the final concentration, and incubated with shaking (200 rpm, 37 °C) for 24 h. Following incubation, the culture was centrifuged at 4 °C, 10,000 rpm for 10 min. Subsequently, 8 mL of the supernatant was extracted with 2 mL of chloroform. The lower (chloroform) layer (1 mL) was transferred to a new centrifuge tube, mixed with 300 μL of 0.2 mol/L HCl, vortex-mixed, and centrifuged. Finally, 200 μL of pink supernatant was taken to determine OD_{520}. The experiments were analyzed in triplicate.

4.3.7. Rhamnolipid production inhibition assay

The overnight culture was diluted to an OD_{600} of 0.01, supplemented with compound STY17 at the target concentration, and incubated with shaking (200 rpm, 37 °C) for 24 h. Following incubation, the culture was centrifuged at 4 °C, 10,000 rpm for 10 min. Subsequently, 2 mL of the supernatant was extracted with 4 mL of diethyl ether by thorough mixing. The ether layer (1 mL) was transferred to a 1.5 mL centrifuge tube and evaporated to dryness. The residue was reconstituted in 100 μL of ultrapure water, mixed with 900 μL of freshly prepared 0.2% orcinol reagent, vortex-mixed thoroughly, and incubated at 80 °C for 30 min in a thermostatic water bath. After cooling to room temperature, 200 μL of the solution was aliquoted for OD_{421} measurement. The experiments were analyzed in triplicate.

4.3.8. Imaging of biofilm structure by CLSM

Different concentrations of compound STY17 were inoculated with *P. aeruginosa* PAO1 in 96-well glass-bottom plates and incubated at 37 °C for 24 h. The supernatant was discarded and the surface of the well plates was washed with PBS three times. 100 μL of PBS containing 1 μmol/L SYTO9 and 10 μmol/L PI dye was added to each well. After incubation for 15 min away from light, the effect of STY17 on the formation of bacterial biofilm was observed by a fluorescence confocal microscope (Zeiss LSM800).

4.3.9. Motility assay

For swarming motility, 20 mL medium (LB agar medium containing 0.5% agar) was added to a Petri dish containing different concentrations of STY17. The mixture was used to prepare solid plates, and then 1 μL of *P. aeruginosa* PAO1 was inoculated onto the surface of the Petri dish. For swimming motility, 20 mL medium (LB agar medium with 0.3% agar) was added to the Petri dish containing different concentrations of STY17. The mixture was used to prepare solid plates, and then 1 μL of *P. aeruginosa* PAO1 was inoculated into the middle of the medium. For twitching motility, 20 mL medium (LB agar medium with 1% agar) was added to the Petri dish containing different concentrations of STY17. The mixture was used to prepare solid plates, and then 1 μL of *P. aeruginosa* PAO1 was inoculated into the bottom of the Petri dish. The Petri dishes were incubated at 37 °C for 16 h. The experiments were analyzed in triplicate.

4.3.10. Scanning electron microscope assay

Overnight cultured *P. aeruginosa* PAO1 was diluted with LB medium to an OD_{600} of 0.05 and then incubated with different concentrations of STY17 for 16 h. The precipitates were then eluted with gradients of 30%, 50%, 70%, 90% and 100% ethanol. Finally, these samples were placed on silicon wafers for SEM (Ultra-55, Zeiss) analysis.

4.3.11. Extracellular polysaccharide production inhibition assay

The overnight cultured *P. aeruginosa* PAO1 was diluted with LB to $OD_{600} = 0.05$, and incubated with different concentrations of compound STY17 at 37 °C for 24 h. Next, the biofilm was washed with 200 μL of physiological saline and sonicated for 40 min. After heating at 80 °C for 30 min, the mixture was cooled and centrifuged for 10 min (4 °C, 10,000 rpm). Take 100 μL of

supernatant with the addition of 100 μL 5% phenol solution, 500 μL concentrated H_2SO_4. It was mixed well and the OD_{490} was measured by a microplate reader. The experiments were analyzed in triplicate.

4.3.12. Determination of iron concentration

The overnight cultured *P. aeruginosa* PAO1 was diluted to an OD_{600} value of 0.05. The diluted bacterial solution was added to ABTGC medium containing different concentrations of the compound and incubated in a shaker at 37 °C, 200 rpm for 16 h. The culture was centrifuged (4000 rpm, 10 min, 4 °C) and the supernatant was discarded. Next, it was washed by adding 5 mL of PBS buffer and finally mixed with 2 mL of PBS buffer. The total intracellular iron ion content was determined using the Elabscience Total Cellular Iron Colorimetric Test Kit. The appropriate reagents and samples were added to the slats according to the manufacturer's instructions, and OD_{593} was determined using a microplate reader after the incubation was completed. The experiments were analyzed in triplicate.

4.3.13. Activity of succinate dehydrogenase

The overnight cultured *P. aeruginosa* PAO1 was diluted to an OD_{600} value of 0.01. The diluted bacterial solution was added to LB broth containing different concentrations of the compound and incubated in a shaker at 37 °C, 200 rpm for 8 h. Then, the samples were centrifuged (4000 rpm, 10 min, 4 °C) to remove the supernatant and washed with PBS buffer. Succinate dehydrogenase activity was next measured using the Solarbio Succinate Dehydrogenase (SDH) Activity Assay Kit. The samples were sonicated with the appropriate reagents according to the manufacturer's instructions, centrifuged, and the supernatant assayed. The experiments were analyzed in triplicate.

4.3.14. Determination of pH in bacteria

The overnight cultured *P. aeruginosa* PAO1 was diluted to an OD_{600} value of 0.01, and the diluted bacterial solution was added to LB broth containing different concentrations of the compounds in a 96-well black plate, and incubated overnight in an incubator at 37 °C. The samples were centrifuged (3000 rpm, 5 min, 4 °C) and the supernatant was discarded. The 2′,7′-bis(2-carboxyethyl)-5-(and 6)-carboxyfluorescein acetoxymethyl ester (BCECF-AM) probe was formulated to a working concentration of 5 μmol/L, and 200 μL of it was added to each well and incubated for 30 min under the protection of light. Finally, the fluorescence value of excitation 500, emission 522 nm was detected by using a microplate reader. The experiments were analyzed in triplicate.

4.3.15. Determination of INT reduction

The overnight cultured *P. aeruginosa* PAO1 was diluted to an OD_{600} value of 0.01, and the diluted bacterial solution was added into ABTGC medium containing different concentrations of the compounds, added into a 96-well black plate, and incubated in an incubator at 37 °C overnight. The samples were centrifuged (3000 rpm, 5 min, 4 °C) and the supernatant was discarded. The iodine nitrotetrazolium (INT) probe was prepared to a working concentration of 10 μmol/L, and 200 μL of it was added to each well and incubated for 30 min under the protection of light, and OD_{490} absorbance was detected by using a microplate reader. The experiments were analyzed in triplicate.

4.3.16. Determination of ATP

The overnight cultured *P. aeruginosa* PAO1 was diluted to an OD_{600} value of 0.01. The diluted bacterial solution was added to LB broth containing different concentrations of compounds and incubated in a shaker at 37 °C, 200 rpm for 16 h. The samples were centrifuged (4000 rpm, 10 min, 4 °C) and the ATP content was determined using the CheKine™ ATP Content Assay Kit. The experiments were analyzed in triplicate.

4.3.17. Determination of membrane potential

The overnight cultured *P. aeruginosa* PAO1 was diluted to an OD_{600} value of 0.01, and the diluted bacterial solution was added to ABTGC medium containing different concentrations of compounds. They were added to 96-well black plates and incubated overnight in a 37 °C incubator. Next, wash them three times with PBS buffer, 200 μL of 10 μmol/L thioflavin (ThT) dye was added to each well for incubation of 30 min away from light, and the effect of STY17 on the membrane potential was observed using a fluorescence confocal microscope (Zeiss LSM800).

4.3.18. Determination of iron chelating ability

The fluorescent probe CP645 was diluted with MOPS (Solarbio, China) buffer to a final concentration of 6 μmol/L. $FeCl_3$ and nitrilotriacetic acid (NTA) were added so that the concentration of Fe^{3+} in the mixture was 30 μmol/L, and the concentration of NTA was 5 μmol/L and incubated away from light for 1 h. Then, the compound STY17 (30 μmol/L) was added to the samples with 30 μmol/L EGCG used as a positive control. After the mixture was incubated for 24 h away from light, the fluorescence intensity was determined using a microplate reader at an excitation wavelength of 435 nm and an emission wavelength of 475 nm. The fluorescence intensity of CP654 and CP654 bound to Fe^{3+} was recorded as 100% and 0%, respectively. pFe^{3+} was calculated by Eq. (1):

$$\text{Fluorescence (\%)} = 11.743\ \text{pFe(III)} - 169 \quad (1)$$

The experiments were analyzed in triplicate.

4.3.19. RT-PCR assay

Total RNA from PAO1 cells was extracted using the Hipure Universal RNA kit (Magen, Shanghai, China), and RNA concentration was measured using a NanoDrop2000 Ultra-Micro Spectrophotometer. RNA was then reverse transcribed using Hieff® qPCR SYBR Green Master Mix (without Rox). Real-time fluorescent quantitative PCR was performed using a LightCycler® 480 Instrument II (Roche, Switzerland). Specific primers are listed in the Supporting Information Table S3. The experiments were analyzed in triplicate.

4.3.20. Development of bacterial resistance assay

Bacteria were cultured using MH medium by picking single colonies in a shaker for 16 h. Antibiotics in combination with or without compounds to be tested were added and cultured for 20 h. The OD_{600} of each group was then determined using a microplate reader, and the MIC values were recorded. Next, take 10 μL 1/2 MIC concentration of the culture to 3 mL of fresh MH medium. The resulting bacterial solution was cultured overnight as the next generation of bacteria, and 12 consecutive generations were cultured until the MIC reached the plateau stage.

4.3.21. Checkerboard assay

First, STY17 and antibiotics (Tobramycin, Ciprofloxacin) were diluted in MH medium. 50 μL of each was added to a 96-well plate in columns and rows to form an 8 × 8 arrangement. Next, a bacterial suspension (OD_{600} = 0.01) was added to the same 96-well plate at 100 μL per well. After incubation at 37 °C for 16−24 h, the absorbance was read at 600 nm. FICI was calculated using the following formula: FICI = (MIC_A combination/MIC_A combination) + (MIC_B combination/MIC_B alone). The calculated FICI was defined as a synergistic effect (FICI ≤0.5), indifferent effect (0.5 < FICI <4), and antagonistic effect (FICI ≥4).

4.3.22. Expression and purification of the SdhB protein

First, the plasmid pET-28a-sdhB was transformed into *E. coli* BL21 (DE3) in which the SdhB protein was expressed contains a 6-His tag. The pET-28a-sdhB strain was induced at a 1:100 ratio. Upon reaching an OD_{600} of approximately 0.4−0.8, 0.2 mmol/L IPTG was added, followed by overnight incubation at 20 °C for 24 h. The next day, the pellet was resuspended in lysis buffer containing the protease inhibitor PMSF (20 mmol/L Tris-HCl, 150 mmol/L NaCl, pH 7.5). After high-pressure homogenization, remove cellular debris by density gradient centrifugation and collect the membrane fraction (10,000 rpm, 40 min, 4 °C/100,000 rpm, 60 min, 4 °C). The membrane fraction was then precipitated in solubilization buffer containing detergent (LMNG) and incubated at 4 °C with gentle shaking for 1−2 h. Insoluble material was removed by ultracentrifugation (13,000 rpm, 40 min, 4 °C) to remove insolubles. The supernatant was incubated with affinity chromatography resin bearing a specific tag (His-tag) at 4 °C. After washing with buffer containing detergent and 30 mmol/L imidazole to remove non-specifically bound proteins, the target protein was collected using elution buffer containing 60 mmol/L imidazole or tag-specific competitive inhibitors. Finally, sample purity and concentration were verified *via* SDS-PAGE and protein concentration measurement. Purified membrane proteins were stored on ice or at 4 °C for MST experiments. All steps were performed on ice or at 4 °C to maintain protein stability.

4.3.23. Microscale thermophoresis (MST) assay

The MST assay employed the Monolith His-Tag Labeling Kit RED-tris-NTA 2nd Generation (Nano Temper, MO-L008). At a concentration of 100 nmol/L, fluorescent labeling of the SdhB-His protein was performed using the His-Tag Labeling Kit (Nano Temper, MO-L008), strictly adhering to the operational guidelines in the user manual. Following labeling, 10 μL of the fluorescently labeled SdhB-His protein was mixed with 10 μL of PBST buffer, followed by the addition of 1 mmol/L STY17. This mixture was subsequently subjected to serial dilutions. Micro-scale thermoelectrophoresis analysis was performed on the NanoTemper Monolith NT.115 instrument, set at 100% LED power and medium MST power level. Experimental data were analyzed using MO Affinity Analysis software (X86 version).

4.3.24. Cytotoxicity assay

RAW264.7, Vero, and BT549 cells cultured to logarithmic growth phase were seeded in plates at a density of 6000 cells/well and 0.1 mL/well and incubated in an incubator at 37 °C and 5% CO_2 for 24 h to make the cells adhere to the wall, respectively. On the following day, the plates were removed, and the original medium was aspirated. 100 μL of the desired concentration of compound was added and the incubation was continued for 24 h. After that, 20 μL of MTT solution (5 mg/mL) was added to each well, and the incubation was continued for 4 h. The cells were then incubated for 4 h with a syringe. Then the supernatant in the 96-well plate was carefully aspirated with a syringe, and 150 μL of DMSO solution was added to each well to dissolve the mezzanine. Finally, the plate was shaken for 15 min, the treated 96-well plate was immediately used to measure its absorbance at 570 nm with a microplate reader to calculate the cell survival rate. The experiments were analyzed in triplicate.

4.3.25. Hemolysis assay

An appropriate amount of fresh mouse or rabbit erythrocytes was centrifuged (2500 rpm, 5 min) and the supernatant was discarded. After being washed three times with PBS, the washed erythrocytes were prepared into 2% erythrocyte suspension with PBS. Next, 150 μL of 2% erythrocyte suspension was added to 1.5 mL centrifuge tubes in each group, and 50 μL of the compound was diluted to the desired concentration. PBS was added to the blank group and 0.4% Triton X-100 solution was used as the positive control group (100% hemolysis). Incubate them at 37 °C for 2 h, during which time gently shake several times. After incubation, 100 μL of supernatant was centrifuged (2500 rpm, 5 min) into a 96-well plate. The absorbance value was measured at 575 nm. The experiments were analyzed in triplicate.

4.3.26. Zebrafish toxicity assay

In the evening of the day before the experiment, 7−18-month-old zebrafish were placed into the mating tank in the ratio of female: male = 1:1 or 2:1, and the following morning, the partition was removed to allow them to mate naturally. The fertilized eggs spawned within 30 min were collected and added with the appropriate amount of embryonic medium to be incubated in a constant-temperature incubator. Zebrafish embryos incubated up to 4 hpf were cultured in PTU embryo medium containing different concentrations of compound in the quantity of 10 embryos/well. Survival rates were recorded at different times, and normally developing juveniles were recorded as survivors, while those that died, developed abnormally, or showed signs of toxicity such as behavioral abnormalities or locomotor disorders were recorded as dead fish.

4.3.27. Biological activity and toxicity of STY17 in G. mellonella

Overnight cultured *P. aeruginosa* PAO1 was diluted with PBS to an OD_{600} value of 0.01. For the *G. mellonella* infection experiment, 10 *G. mellonella* larvae in each group were injected with 5 μL of a PBS mixture containing the bacteria with different concentrations of the drug, and the survival rate at different times was recorded. For the toxicity experiment in *G. mellonella*, 10 *G. mellonella* larvae per group were injected with 5 μL of PBS containing different concentrations of compound and the survival rate was recorded at different times.

4.3.28. Mice wound infection model

The wound infection model was conducted in BALB/c mice purchased from SPF (Beijing) Biotechnology Co., Ltd. This animal experiment was performed following the National Regulations on Animal Experimentation (IACUC approval number: Szwwbio-IACUC-20241014-01). Healthy 4-week-old female mice (n = 5) of were selected for acclimatization for 1 week. *P. aeruginosa* PAO1, PA185, and PA187 cultured overnight were adjusted to a bacterial concentration of 5 × 10^8 CFU/mL with saline. The compound was dissolved in saline containing 0.1%

DMSO, and the antibiotics were dissolved in saline. First, a wound of approximately 5 mm in diameter was created on the back of the mice, and then 30 μL of bacterial solution was dripped on the surface of the wound to establish infection for 24 h. After the wound was infected, it was treated with saline, antibiotics, or antibiotics in combination with compound, respectively, for three consecutive days. After that, the mice were euthanized, and the skin at the wound of some mice in each group was homogenized and plated on agar plates for CFU counting. Meanwhile, the mice were monitored daily for wound recovery and body weight changes. After 9 days, the remaining mice in each group were euthanized, and their hearts, livers, spleens, lungs, and kidneys were taken for H&E staining analysis.

4.3.29. Acute toxicity study

Four-week-old female and male BALB/c mice were randomly divided into eight groups ($n = 3$). After a 12-h fast, all mice received single oral doses of either vehicle, 50, 100, or 200 mg/kg STY17. The vehicle consisted of physiological saline containing 5% DMSO and 10% Tween 80. Subsequently, mouse survival, body weight, and physiological activity were continuously monitored for 2 weeks. All mice were euthanized on Day 14, and major organs were collected for H&E staining analysis.

4.3.30. In vivo pharmacokinetic studies

Six female BALB/c mice were randomly divided into two groups ($n = 3$), receiving intraperitoneal injection and intravenous injection of 10 mg/kg STY17, respectively. Blood samples were collected at 5, 15, 30 min, 1, 2, 4, 7 and 24 h. Samples were then transferred to microcentrifuge tubes containing EDTA-K2 anticoagulant. After centrifugation at 4 °C and 4000×*g* for 5 min, the supernatant was collected and stored at −80 °C for subsequent LC−MS/MS analysis of compound concentrations in plasma samples. Finally, pharmacokinetic parameters were calculated using WinNonlin software based on the obtained analytical data.

Acknowledgments

We sincerely thank the First Affiliated Hospital and Guangzhou Red Cross Hospital of Jinan University Clinical Laboratory for gifting clinical multidrug-resistant *P. aeruginosa* strains. Part of the images were created in BioRender.com with permission (https://BioRender.com/1vhotto). This work was supported by the National Natural Science Foundation of China (82304274, 82473788), Natural Science Foundation of Guangdong Province, China (2025A1515012144), the Fundamental Research Funds for the Central Universities, and Tianchi Academic Elite Leader Project.

Author contributions

Siyu Zhao, Jie Tang and Ziyang Du contributed equally to this work. Siyu Zhao and Ziyang Du wrote the manuscript and performed most of experiments. Jie Tang performed the biological activity experiments and revised the manuscript. Pinghua Sun designed the project, supervised the chemical experiments and revised the manuscript. Jun Liu designed the project, supervised the biological experiments and revised the manuscript. Junxia Zheng designed and supervised the computer experiments. Yiqun Chang performed the computer experiments and revised the manuscript. Yujie Li, Yingbo Zhou, Wenqian Liu, Xiao Wu, Xibing Hu, Xin Long, Dengchao Lian, Jinglin Xie, Tiantian Xie, Shuo Dai, Daxi He, Jiahui Su, Youfeng Zhu performed some chemical experiments or biological experiments.

Conflicts of interest

The authors declare that there are no conflicts of interest.

Appendix A. Supporting information

Supporting information to this article can be found online at https://doi.org/10.1016/j.apsb.2026.02.002.

References

1. Melchiorri D, Rocke T, Alm RA, Cameron AM, Gigante V. Addressing urgent priorities in antibiotic development: insights from who 2023 antibacterial clinical pipeline analyses. *Lancet Microbe* 2025;**6**:100992.
2. Antimicrobial Resistance Collaborators. Global burden of bacterial antimicrobial resistance in 2019: a systematic analysis. *Antimicrobial Resistance Collaborators, The Lancet* 2022;**399**:629−55.
3. Ho CS, Wong CTH, Aung TT, Lakshminarayanan R, Mehta JS, Rauz S, et al. Antimicrobial resistance: a concise update. *Lancet Microbe* 2025;**6**:100947.
4. GBD 2021 Antimicrobial Resistance Collaborators. Global burden of bacterial antimicrobial resistance 1990−2021: a systematic analysis with forecasts to 2050. *Lancet* 2024;**404**:1199−226.
5. Tacconelli E, Carrara E, Savoldi A, Harbarth S, Mendelson M, Monnet DL, et al. Discovery, research, and development of new antibiotics: the WHO priority list of antibiotic-resistant bacteria and tuberculosis. *Lancet Infect Dis* 2018;**18**: 318−27.
6. Burki T. High-level meeting on antimicrobial resistance 2024. *Lancet Infect Dis* 2024;**24**:e684−5.
7. Payne DJ, Gwynn MN, Holmes DJ, Pompliano DL. Drugs for bad bugs: confronting the challenges of antibacterial discovery. *Nat Rev Drug Discov* 2007;**6**:29−40.
8. Azam MW, Khan AU. Updates on the pathogenicity status of *pseudomonas aeruginosa. Drug Discov today* 2019;**24**:350−9.
9. Horcajada JP, Montero M, Oliver A, Sorlí L, Luque S, Gómez-Zorrilla S, et al. Epidemiology and treatment of multidrug-resistant and extensively drug-resistant *Pseudomonas aeruginosa* infections. *Clin Microbiol Rev* 2019;**32**:e00031. 19.
10. Davis R, Markham A, Balfour JA. Ciprofloxacin. *Drugs* 1996;**51**: 1019−74.
11. Brogden RN, Pinder RM, Sawyer PR, Speight TM, Avery GS. Tobramycin: a review of its antibacterial and pharmacokinetic properties and therapeutic use. *Drugs* 1976;**12**:166−200.
12. Valencia IC, Kirsner RS, Kerdel FA. Microbiologic evaluation of skin wounds: alarming trend toward antibiotic resistance in an inpatient dermatology service during a 10-year period. *J Am Acad Dermatol* 2004;**50**:845−9.
13. Costerton JW, Stewart PS, Greenberg EP. Bacterial biofilms: a common cause of persistent infections. *Science* 1999;**284**:1318−22.
14. Maurice NM, Bedi B, Sadikot RT. *Pseudomonas aeruginosa* biofilms: host response and clinical implications in lung infections. *Am J Respir Cell Mol Biol* 2018;**58**:428−39.
15. Flemming HC, Wingender J. The biofilm matrix. *Nat Rev Microbiol* 2010;**8**:623−33.
16. Fux CA, Costerton JW, Stewart PS, Stoodley P. Survival strategies of infectious biofilms. *Trends Microbiol* 2005;**13**:34−40.
17. Mah T-FC, O'Toole GA. Mechanisms of biofilm resistance to antimicrobial agents. *Trends Microbiol* 2001;**9**:34−9.
18. Davies D. Understanding biofilm resistance to antibacterial agents. *Nat Rev Drug Discov* 2003;**2**:114−22.

19. Powell LC, Pritchard MF, Ferguson EL, Powell KA, Patel SU, Rye PD, et al. Targeted disruption of the extracellular polymeric network of *Pseudomonas aeruginosa* biofilms by alginate oligosaccharides. *npj Biofilms Microbiomes* 2018;**4**:13.
20. Pritchard Manon F, Powell Lydia C, Jack Alison A, Powell K, Beck K, Florance H, et al. A low-molecular-weight alginate oligosaccharide disrupts *pseudomonal* microcolony formation and enhances antibiotic effectiveness. *Antimicrob Agents Chemother* 2017;**61**:e00762. 17.
21. Harris ES, Novak L, Fernandez-Petty CM, Lindgren NR, Baker SM, Birket SE, et al. SNSP113 (PAAG) improves mucociliary transport and lung pathology in the Scnn1b-Tg murine model of CF lung disease. *J Cyst Fibros* 2023;**22**:1104−12.
22. Narayanaswamy VP, Giatpaiboon S, Baker SM, Wiesmann WP, LiPuma JJ, Townsend SM. Novel glycopolymer sensitizes burkholderia cepacia complex isolates from cystic fibrosis patients to tobramycin and meropenem. *PLoS One* 2017;**12**:e0179776.
23. Reig S, Le Gouellec A, Bleves S. What is new in the anti−*Pseudomonas aeruginosa* clinical development pipeline since the 2017 WHO alert?. *Front Cell Infect Microbiol* 2022;**12**:909731.
24. Pritchard MF, Powell LC, Menzies GE, Lewis PD, Hawkins K, Wright C, et al. A new class of safe oligosaccharide polymer therapy to modify the mucus barrier of chronic respiratory disease. *Mol Pharm* 2016;**13**:863−72.
25. Popova M, Isayev O, Tropsha A. Deep reinforcement learning for *de novo* drug design. *Sci Adv* 2018;**4**:eaap7885.
26. Blaschke T, Arús-Pous J, Chen H, Margreitter C, Tyrchan C, Engkvist O, et al. REINVENT 2.0: an AI tool for *de novo* drug design. *J Chem Inf Model* 2020;**60**:5918−22.
27. Loeffler HH, Wan S, Klähn M, Bhati AP, Coveney PV. Optimal molecular design: generative active learning combining REINVENT with precise binding free energy ranking simulations. *J Chem Theor Comput* 2024;**20**:8308−28.
28. Filella-Merce I, Molina A, Orzechowski M, Díaz L, Zhu YM, Mor JV, et al. Optimizing drug design by merging generative AI with active learning frameworks. arxiv:230506334 [Preprint]. 2023 [cited 2026 Feb 6]. Available from: https://arxiv.org/abs/2305.06334.
29. Eckmann P, Wu D, Heinzelmann G, Gilson MK, Yu R. MFBind: a multi-fidelity approach for evaluating drug compounds in practical generative modeling. arxiv:240210387 [Preprint]. 2024 [cited 2026 Feb 6]. Available from: https://arxiv.org/abs/2402.10387.
30. Liu J, Hou JS, Chang YQ, Peng LJ, Zhang XY, Miao ZY, et al. New *pqs* quorum sensing system inhibitor as an antibacterial synergist against multidrug-resistant *Pseudomonas aeruginosa*. *J Med Chem* 2022;**65**:688−709.
31. Liu J, Zhao S, Hu J, Chen Q, Jiao S, Xiao H, et al. Novel coumarin derivatives inhibit the quorum sensing system and iron homeostasis as antibacterial synergists against *Pseudomonas aeruginosa*. *J Med Chem* 2023;**66**:14735−54.
32. Zhang Z, Zhao S, Liu W, Wu X, Tang J, Li Y, et al. Hybrid molecules of benzothiazole and hydroxamic acid as dual-acting biofilm inhibitors with antibacterial synergistic effect against *Pseudomonas aeruginosa* infections. *J Med Chem* 2025;**68**:6210−32.
33. Li Y, Liu J, Huang Z, Yu J, Xu X, Sun P, et al. Design, synthesis and biological evaluation of 2-substituted 3-hydroxy-6-methyl-4*H*-pyran-4-one derivatives as *Pseudomonas aeruginosa* biofilm inhibitors. *Eur J Med Chem* 2018;**158**:753−66.
34. Liu J, Hou J, Li Y, Miao Z, Sun P, Lin J, et al. Novel 2-substituted 3-hydroxy-1,6-dimethylpyridin-4(1*H*)-ones as dual-acting biofilm inhibitors of *Pseudomonas aeruginosa*. *J Med Chem* 2020;**63**: 10921−45.
35. Liu J, Meng Y, Yang M, Zhang X, Zhao J, Sun P, et al. Design, synthesis and biological evaluation of novel 3-hydroxypyridin-4(1*H*)-ones based hybrids as *Pseudomonas aeruginosa* biofilm inhibitors. *Eur J Med Chem* 2023;**259**:115665.
36. Liu J, Wu W, Hu J, Zhao S, Chang Y, Chen Q, et al. Novel benzothiazole derivatives target the Gac/Rsm two-component system as antibacterial synergists against *Pseudomonas aeruginosa* infections. *Acta Pharm Sin B* 2024;**14**:4934−61.
37. Loeffler HH, He J, Tibo A, Janet JP, Voronov A, Mervin LH, et al. Reinvent 4: modern AI-driven generative molecule design. *J Cheminf* 2024;**16**:20.
38. Heid E, Greenman KP, Chung Y, Li SC, Graff DE, Vermeire FH, et al. Chemprop: a machine learning package for chemical property prediction. *J Chem Inf Model* 2024;**64**:9−17.
39. Liu J, Chen Q, Wu W, Wang D, Zhao S, Li J, et al. Novel ligustilide derivatives target quorum sensing system LasR/LasB and relieve inflammatory response against *Pseudomonas aeruginosa* infection. *Eur J Med Chem* 2024;**263**:115972.
40. Liu J, Li J, Zhao S, Chang Y, Chen Q, Wu W, et al. Discovery of *N*-(phenylsulfonyl)thiazole-2-carboxamides as potent α-glucosidase inhibitors. *Drug Dev Res* 2024;**85**:e22128.
41. *RDKit: Open-source cheminformatics*. Available from: https://www.rdkit.org.
42. Gaupp R, Schlag S, Liebeke M, Lalk M, Götz F. Advantage of upregulation of succinate dehydrogenase in *Staphylococcus aureus* biofilms. *J Bacteriol* 2010;**192**:2385−94.
43. Keohane CE, Steele AD, Fetzer C, Khowsathit J, Van Tyne D, Moynié L, et al. Promysalin elicits species-selective inhibition of *Pseudomonas aeruginosa* by targeting succinate dehydrogenase. *J Am Chem Soc* 2018;**140**:1774−82.
44. Yankovskaya V, Horsefield R, Törnroth S, Luna-Chavez C, Miyoshi H, Léger C, et al. Architecture of succinate dehydrogenase and reactive oxygen species generation. *Science* 2003;**299**:700−4.
45. UniProt: a worldwide hub of protein knowledge. *Nucleic Acids Res* 2019;**47**:D506−15.
46. Mirdita M, Schütze K, Moriwaki Y, Heo L, Ovchinnikov S, Steinegger M. ColabFold: making protein folding accessible to all. *Nat Methods* 2022;**19**:679−82.
47. De Backer S, Sabirova J, De Pauw I, De Greve H, Hernalsteens JP, Goossens H, et al. Enzymes catalyzing the TCA- and urea cycle influence the matrix composition of biofilms formed by methicillin-resistant *Staphylococcus aureus USA300. Microorganisms* 2018;**6**:113.
48. Moura-Alves P, Puyskens A, Stinn A, Klemm M, Guhlich-Bornhof U, Dorhoi A, et al. Host monitoring of quorum sensing during *Pseudomonas aeruginosa* infection. *Science* 2019;**366**:eaaw1629.
49. Pecsi I, Hards K, Ekanayaka N, Berney M, Hartman T, Jacobs WR, et al. Essentiality of succinate dehydrogenase in mycobacterium smegmatis and its role in the generation of the membrane potential under hypoxia. *mBio* 2014;**5**:e01093-14.
50. Ma Y, Xie Y, Hider RC. A novel fluorescence method for determination of pFe^{3+}. *Analyst* 2013;**138**:96−9.
51. Zhou X, Gao Y, Wang W, Yang X, Yang X, Liu F, et al. Architecture of the mycobacterial succinate dehydrogenase with a membrane-embedded Rieske FeS cluster. *Proc Natl Acad Sci USA* 2021;**118**: e2022308118.
52. Zhang N, Dhumal D, Kuo SH, Lew SQ, Patil PD, Taher R, et al. Targeting the phosphatidylglycerol lipid: an amphiphilic dendrimer as a promising antibacterial candidate. *Sci Adv* 2024;**10**:eadn8117.
53. Yang B, Tong Z, Shi J, Wang Z, Liu Y. Bacterial proton motive force as an unprecedented target to control antimicrobial resistance. *Med Res Rev* 2023;**43**:1068−90.
54. Farha Maya A, Verschoor Chris P, Bowdish D, Brown Eric D. Collapsing the proton motive force to identify synergistic combinations against. *Staphylococcus aureus. Chem Biol* 2013;**20**:1168−78.
55. Prindle A, Liu J, Asally M, Ly S, Garcia-Ojalvo J, Süel GM. Ion channels enable electrical communication in bacterial communities. *Nature* 2015;**527**:59−63.
56. Köhler T, Curty LK, Barja F, Delden Cv, Pechère -C. Swarming of *Pseudomonas aeruginosa* is dependent on cell-to-cell signaling and requires flagella and pili. *J Bacteriol* 2000;**182**:5990−6.
57. Anyan ME, Amiri A, Harvey CW, Tierra G, Morales-Soto N, Driscoll CM, et al. Type IV pili interactions promote intercellular

association and moderate swarming of *Pseudomonas aeruginosa*. *Proc Natl Acad Sci USA* 2014;**111**:18013−8.
58. Condren AR, Kahl LJ, Boelter G, Kritikos G, Banzhaf M, Dietrich LEP, et al. Biofilm inhibitor taurolithocholic acid alters colony morphology, specialized metabolism, and virulence of *Pseudomonas aeruginosa*. *ACS Infect Dis* 2020;**6**: 603−12.
59. CLSI. CLSI M100 35th. Clinical and Laboratory Standards Institute; 2025. Available from: https://clsi.org/shop/standards/m100-ed35/.
60. Chen S, Liu D, Wang L, Fan A, Wu M, Xu N, et al. Marine-derived new peptaibols with antibacterial activities by targeting bacterial membrane phospholipids. *Acta Pharm Sin B* 2025;**15**:2764−77.
61. *Schrödinger release 2023-1: desmond molecular dynamics System, D. E. Shaw research*. 2023. New York, NY.
62. *Schrödinger release 2023-1: glide*. New York, NY: Schrödinger, LLC; 2023.
63. *Schrödinger release 2023-1: prime*. New York, NY: Schrödinger, LLC; 2023.